To the Graduate Council:

I am submitting herewith a dissertation written by Dujiu Yang entitled "Enhanced Particle Agglomeration in Coal-fired MHD Systems Through Injection". I have examined the final copy of this dissertation for form and content and recommend that it be accepted in partial fulfillment of the requirements for the degree of Doctor of Philosophy, with a major in Engineering Science.

L.W. Crawford, Major Professor

We have read this dissertation
and recommend its acceptance:

Accepted for the Council:

Associate Vice Chancellor
and Dean of the Graduate School

Enhanced Particle Agglomeration In Coal-Fired MHD Systems Through Injection

A Dissertation

Presented for the

Doctor of Philosophy

Degree

The University of Tennessee, Knoxville

Dujiu Yang

December, 1993

DEDICATION

This work is dedicated to my great father

Changqi Yang

Acknowledgments

The author is grateful for the advice and support of this research effort rendered by his doctoral committee chairman, Dr. Lloyd W. Crawford. The author thanks committee member, Dr. A.C. Sheth, for his great ideas and his invaluable advice. The author is also grateful to Dr. Tom Giel, Jr. for his support. Thanks are extended to Drs. B. Antar, and M. H. MaCay for serving as members of the author's doctoral committee and for their recommendations concerning this dissertation.

A very special thanks to all members of Energy Conversion Division for assistance in the course of the development of this dissertation, especially Bob Douglas, Bill Millard, Jeff Holt, Mike Hodges, Dr. Brad Winkleman, John Lineberry, and Jack Parker for their assistance with the experiments. A very special thanks to Michael Bonin and Adrian Wu of Insitec, Inc. for providing remarkable test data.

The author would like to thank Mrs. Mary Lo for her help. Finally, the author would like to thank his wife, Kewei, for her encouragement and faithful support as well as scientific support during the course of this endeavor.

ABSTRACT

In the open cycle coal-fired MHD system, ash is generated from burning coal in the combustor and downstream condensation of potassium seed species, and is a potential pollutant. A range of ash particle sizes is produced by the MHD system, including a high concentration of submicron particles. Research at the US.DOE coal fired flow facility (CFFF) has addressed ash removal with baghouse (BH) filters and an electrostatic precipitator (ESP). After filtration in the BH, most of the ash particles are removed from the flow. However, some of the smaller particles pass through the filter into the exhaust air. At the ESP, submicron particles also pass into the exhaust air due to low collection efficiencies for this size particle. A particle agglomeration method presented in the dissertation can decrease the submicron portion of the ash and thus improve particle collection. When appropriate particles are injected into the flow, small particles will agglomerate around these particles so that more of the particle ash will be larger in size, and therefore be easily removed from the flow by the BH or ESP. The larger particles will also give higher overall energy conversion efficiency by raising superheater heat transfer efficiency and reducing energy consumption in the BH or the ESP.

In this dissertation, a theoretical model is presented in two parts. The first part represents particle growth at the section where particles are injected. Because temperature at this section is very high, the flow is in the three phases and in the supersaturated state, and particles have thermophoretic coagulation, condensation growth and heterogeneous nucleation growth. A kinetic rate, modified coagulation equation, is given to describe these three processes associated with particle injection. This equation can be solved numerically

for either each single phenomenon or as combination of these phenomena. The second part is the section after particle injection. This part considered what occurs in the 14 sections of the CFFF from cooling section 1 to the inlet of the BH and ESP. The primary process at this part is particle thermophoretic coagulation only. Discussions of thermophoretic coagulation, condensation, nucleation and particle injection are presented for the injection point and after injection point. The theoretical results show that particle size distribution is shifted to lower submicron particle densities with particle injection and the total number of particle is also even lower when additional particles are introduced into the flow after cooling section 1. Finally, measured particle size distributions at the inlet of the CFFF BH and ESP with and without particle injection are compared to the calculated distribution based on the theory developed in the dissertation. The experimental data support the theoretical prediction.

TABLE OF CONTENTS

Page

CHAPTER 1 INTRODUCTION 1

1.1 Background 1

1.2 General Descriptions of Current MHD System at UTSI 5

1.3 Objectives 8

CHAPTER 2 THEORY 11

2.1 Dynamic Behavior of a Single Particle 11

2.1.1 Equation of Motion 11

2.1.2 Behavior of the Particle 13

2.2 Particle Collection Efficiency and Collision Frequency 19

2.2.1 Particle Collection Efficiency 19

2.2.2 Particle Collision Frequency 24

2.3 Studies of Particle Size Distribution (PSD)--Modified Coagulation Equation 24

2.3.1 Coagulation Equation 26

2.3.1.1 Numerical Solution of the Coagulation Equation 27

2.3.1.2 Characteristic Time for Agglomeration 28

2.3.2 Coagulation Equation with Particle Injection 30

2.3.3 Coagulation Equation with Condensation 44

2.3.3.1 Rate of Solid Particle Growth 45

2.3.4 Coagulation Equation with Heterogeneous Nucleation 47

2.3.5 Modified Coagulation Equation with Heterogeneous Nucleation, Condensation, and Particle Injection 50
2.4 Particle Agglomeration After Injection 54

CHAPTER 3 EXPERIMENTS 56
3.1 Particle Size Measurement at the Secondary Combustor and Comparison with Im's Theoretical Prediction 57
3.2 Particle Size Measurements at TS1 and the BH and ESP Inlet 57
3.3 Theoretical Calculation without Particle Injection 61
3.3.1 Evolution of Particle Size Distribution from the Secondary Combustor to CS1 65
3.3.2 Evolution of Particle Size Distribution from TS1 to the Inlet of the BH 66
3.4 Theoretical Calculation with Particle Injection 67
3.4.1 Evolution of Particle Size Distribution from the Secondary Combustor to TS1 with particle injection 68
3.4.2 Evolution of Particle Size Distribution from CS1 to the Inlet of the BH with Particle Injection 70
3.5 Comparison of Theoretical and Experimental Results with Injection and without Injection 70

CHAPTER 4 CONCLUSIONS 77

CHAPTER 5 RECOMMENDATIONS 80
5.1 Laboratory Study and Apparatus 80
5.2 Study of Collision Efficiency of Large Particle 82

5.3 Heterogeneous Nucleation 84

LIST OF REFERENCES 86

APPENDICES 94

APPENDIX A THEORETICAL PREDICATION OF INITIAL PARTICLE SIZE DISTRIBUTION AND EXPERIMENTAL MEASUREMENTS AT CFFF 95

APPENDIX B THERMOPHORESIS 105

APPENDIX C THERMAL FORCE BETWEEN TWO PARTICLES 110

APPENDIX D TWO PARTICLE INTERACTION IN THERMOPHORESIS 112

APPENDIX E DERIVATION OF RATE OF PARTICLE GROWTH 122

APPENDIX F NUCLEATION 128

APPENDIX G TURBULENT AND GRAVITATIONAL COAGULATION 138

APPENDIX H MIGRATION OF PARTICLES TO THE WALL 142

APPENDIX I PARTICLE INJECTOR AND ITS MASS LOADING 149

VITA 151

LIST OF FIGURES

Figure Page

1.1 Particle Size Distribution Measured Before and After the CFFF BH&DESP 3

1.2 CFFF Schematic Diagram 6

2.1.1 Single Particle in a Flow 12

2.1.2 Particle Displacement vs. Time 15

2.1.3 Particle Displacement vs. Radius 16

2.1.4 Particle Displacement vs. Particle Temperature 16

2.1.5 Particle Displacement vs. Injection Angle 17

2.1.6 Particle Displacement vs. Injection Velocity 18

2.2.1 Definition of Collection Efficiency of Particle 19

2.2.2 Temperature of Particle vs. Particle Size 23

2.2.3 Collection Efficiency vs. Particle Size with $r_j >> r_i$ 23

2.3.1 Numerical Solution of Coagulation Equation 28

2.3.2.1 Injection at r = 2 μm with V = 1.0 m/s 33

2.3.2.2 Injection at r = 4 μm and V = 1.0 m/s 33

2.3.2.3 Injection at r = 6 μm with V = 1.0 m/s 34

2.3.2.4 Injection at r = 2 μm and V = 0.1 m/s 35

2.3.2.5 Injection at r = 2 μm and V = 10.0 m/s 35

2.3.2.6 Injection at r = 2 μm and V = 1.0 m/s 36

2.3.2.7 Injection of n_0 =1.0x10^{+13}/m^3, σ=0.15, a =12.39, V=1.0 m/s 38

2.3.2.8 Injection of n_0=2.0x10^{+13}/m^3, σ=0.15, a=12.39, V=1.0 m/s 38

2.3.2.9 Injection of n_0 =0.5x10^{+13}/m^3, σ=0.15, a=12.39, V=1.0 m/s 39

2.3.2.10 Injection of n_0=1.0x10^{+13}/m^3, σ=0.15, a=12.39, V=0.1m/s..... 40

2.3.2.11 Injection of n_0=1.0x10^{+13}//m^3, σ=0.29, a=13.04, V=1.0 m/s..... 40

2.3.2.12 Injection of n_0=0.5x10^{+13}/m^3, σ=0.29, a=13.04, V=1.0 m/s..... 41

2.3.2.13 Injection of n_0=1.0x10^{+13}/m^3, σ=0.29, a=13.04, V=1.0 m/s..... 42

2.3.2.14 Injection of n_0=1.0x10^{+13}/m^3, σ=0.55, a=13.61, V=1.0 m/s..... 43

2.3.2.15 Injection of n_0 =1.0x10^{+13}/m^3, σ=0.38, a=13.29, V=1.0 m/s..... 43

2.3.3.1 Condensation Growth at the CFFF..... 46

2.3.3.2 PSD with Condensation Growth and Thermophoretic Coagulation..... 47

2.3.4.1 PSD with Heterogeneous Nucleation 49

2.3.4.2 PSD with Nucleation and Thermophoretic Coagulation 50

2.3.5.1 PSD with Condensation and Heterogeneous Nucleation 52

2.3.5.2 PSD with Condensation, Nucleation &Thermophoresis..... 53

2.3.5.3 PSD with Condensation, Nucleation, Thermophoresis & Injection..... 53

3.1.1 Locations of Injection Port and Measurement Port..... 58

3.2.1 Particle Size Measurements at TS1 by Insitec, Inc..... 59

3.2.2 PSD at the Inlet of the BH and ESP During LMF5I Test 60

3.3.1 PSD with Thermophoretic Coagulation 62

3.3.2 PSD with Condensation..... 62

3.3.3 PSD with Heterogeneous Nucleation..... 63

3.3.4 PSD with Nucleation and Condensation 64

3.3.5 PSD with Thermophoresis and Condensation..... 64

3.3.6 PSD with Thermophoresis and Nucleation 65

3.3.7 Predicted PSD at CS1 without Particle Injection 66

3.3.8 Predicted PSD and Particle Loading From CS1 to the BH and ESP Inlet..... 67

3.4.1 Measured PSD of Injected Particles at Different Mass Loading 68

3.4.2 Predicted PSD at Injection Section and Particle Loading with Injection..... 69

3.4.3 Predicted PSD and Particle Loading at Injection Section with Injection..... 69
3.4.4 Predicted PSD and Particle Loading at the BH and ESP Inlet..... 70
3.5.1 Predicted PSD at CS1 with and without Injection..... 71
3.5.2 Particle Loading vs. Gas Temperatures From the SC to CS1 72
3.5.3 PSD at the inlet of the BH and ESP with and without Injection..... 73
3.5.4 Particle Loading at Different Section..... 73
3.5.5 Experimental Measurements with and without Injection 75
3.5.6 Comparison of Theoretical and Experimental Results..... 76
5.1 Proposed Laboratory Test Configuration..... 81
5.2 Illustration of Collection Efficiency 83
A.1 Particle Growth Evaporation Model 97
A.2 Measured PSD at the ESP and BH Inlet by Insitec 102
A.3 Im's Prediction and 5-stage Cyclone Measurement at the Outlet of the
Secondary Combustor..... 104
B.1 $f(\lambda/r)$ vs. Radius of Particle..... 108
B.2 Thermophoretic Velocity..... 109
C.1 Interaction of Two Spherical Particles..... 110
D.1 Bispherical Coordinates..... 114
F.1 ΔG Required to Form a Droplet of Radius r in a Vapor with Partial Pressure p..... 131
F.2 Supersaturated Ratio and Nucleation Rate After the SC at CFFF 133
F.3 Critical Radius and Nucleation Rate After the SC at CFFF 133
F.4 An Embryo in the Form of a Spherical Cap..... 135
F.5 Heterogeneous Nucleation Rate 137
H.1 Sketch of Flow Regions 142
H.2 Collection Efficiency of the Wall..... 148
I.1 Sketch of Particle Injector..... 149

I.2 Injection Experiment at CFFF 150
I.3 Injector Flow Rate vs. Air Pressure 150

NOMENCLATURE

a, a_1, a_2	particle radius, m
a', b', c'	constants
A	area, m^2
C_m, C_s, C_t	constants
C_p	specific heat at constant pressure, J/kg-K
b_{ij}	collision frequency
d	separation distance of two adjacent large particles
D	diameter, m
D_e	particulate eddy diffusivity, m^2/s
D_v	molecular diffusivity of vapor, m^2/s
$f(x,z)$	correction function to heterogeneous nucleation rate
f_j	distribution function
$\vec{F}$	force, N
$\vec{F}_d, F_v$	drag force, N
$g(r_i,r_j)$	relative speed between particle i and j, m/s
$\Delta G^*, \Delta G$	free energy, J
h	convection heat transfer coefficient, W/m^2-K
I^0	nucleation rate of a single particle, 1/s
J	nucleation rate, No./s-m^3
J_A	mass flux of species A to wall, kg/m
k	Boltzmann constant, 1.38×10^{-23} J/K
k_g, K	thermal conductivity of gas, J/m-s-K

K_n	Knudsen number
k_p	thermal conductivity of particle, J/m-s-K
L_c	latent heat, J/kg
L_{ij}	turbulent collision rate density, No./m^2-s
m	mass of particle, kg
M_g	molecular weight of gas
$\dot{m}$	mass flux of CFFF flow; mass flux of condensable species, kg/s
$\dot{M}$	mass flux of nuclei injection, kg/s
m_c	mass of condensable vapor molecule, kg
$n(r,t)$, n_i,n_j	number distribution, No./m^3
N	particle loading, No./m^3
N_A	Avogadro's number
p	pressure, N/m^2
p_{sat}	saturated pressure, N/m^2
Δp	pressure drop, N/m^2
$Q(r_i,r_j)$	collision cross section, m^2
Q	rate of injection, No./s
$\dot{q}$	heat flow, W
$\dot{q}$"	heat flux, W/m^2
r, r_0, r_i, r_j	radius of particle, m
$\bar{r}$	particle displacement, m
$\dot{r}$	rate of particle growth, m/s
r^*	critical radius, m
R_g	gas constant, J/kg-K
R_e	Reynolds number
R_v	gas constant of vapor, J/kg-K

S	supersaturation ratio
Sc	Schmidt number
S_t	Stanton number
T_0, T_g	gas temperature, K
T_p	particle temperature, K
T_f	flow temperature, K
T_w	wall temperature, K
$U,\ U_1,\ U_2$	velocity, m/s
U_t	thermophoretic velocity, m/s
$\vec{V}, \vec{V}_f, \vec{V}_0$	velocity, m/s
$\overline{V}$	average flow velocity, m/s
V^*	friction velocity, m/s
x, y	coordinates
$\dot{x}, \dot{y}$	velocity along x and y axis, m/s

Greek Letters:

α	thermal diffusivity, m^2/s
α_c	evaporation coefficient
δ	Dirac delta function
δt	time interval, t
ε	emissivity
ε'	eddy diffusivity of gas, m^2/s
ε_t	energy dissipated per unit mass, J/kg
γ	ratio of specific heat
Γ	thermophoretic coagulation terms

η_{ij}	collection efficiency
λ	mean free path, m
μ_g	gas viscosity, kg/s-m
ν	kinematic viscosity, m^2/s
ρ_g	density of gas, kg/m^3
ρ_l	density of liquid (condensed), kg/m^3
ρ_v	density of vapor, kg/m^3
ρ_p	density of particle, kg/m^3
σ	Stefan-Boltzmann constant; surface tension, N/m; constant
τ	dimensionless variable
τ_0	characteristic time of agglomeration, s
τ_w	shear stress, N/m^2

CHAPTER 1 INTRODUCTION

1.1 Background

Coal is widely used as one of the major energy sources in many countries. It is predicted that coal will serve human beings for at least the next fifty years before new energy sources, such as nuclear fusion, are developed and when other energy sources, such as oil, are used up. Coal is most commonly used today in electrical power plants, which consume millions and millions of tons of coal every year.

In an open cycle coal-fired system, like power plants, coal serves as a relatively cheap source of fuel, but it creates certain problems, too. Any type of coal contains percentage of ash and other materials useless for energy conversion, for instance, sulfur and nitrogen. Table 1 (next page) gives some analyses of different coals. Typically, ash companies 5 to 10 percent and sulfur companies 1.0 to 5.0 percent of coal. These materials become pollutants when discharged as past of the stack gases. When these materials are discharged to the air, they contribute to pollution problems, such as acid rain. Major pollutants like this, therefore, must be significantly removed from the flue gases prior to discharge out the stack.

The most important equipment used to remove ash pollutants are the dry electroprecipitator (DESP), the wet electroprecipitator (WESP), and the baghouse (BH). Cyclones have also been used for ash removal, but not generally in large plants. These devices are able to

Table 1 Analytical Data from some Coals of Different Ranks;[1]

Coal	Seam	County & State	*As received* Moisture(%)	Ash(%)	*Ultimate Composition, maf(%)* C	H	N	O	S
Lignite	Coteau	Ward, ND	32.5	5.0	72.38	5.30	1.12	20.53	0.67
Subbituminous B	Unnamed	Weld, CO	20.7	3.9	77.69	5.24	1.60	14.98	0.49
High-volatile B	6	Franklin, IL	5.4	10.3	81.41	5.64	1.56	7.89	3.50
High-volatile A Bituminous	Pittsburgh	Allegheny, PA	1.7	7.8	82.92	5.91	1.80	6.34	3.03
Medium-volatile A Bituminous	Sewell	Fayette, WV	1.4	1.8	89.47	4.93	1.66	3.49	0.45
Anthracite	Lykens	Luzerne, PA	4.2	2.4	94.88	1.83	0.67	1.78	0.84

remove most typical coal produced particulates very effectively. For example, mass efficiencies of particulate removal exceeding 99% for an ESP can be achieved even under severe industrial conditions. But each of these devices has shown a low collection efficiency for the submicron size range of particles. The capability of the DESP is weakened for particle sizes in the submicron size range of 0.2-0.8μm because these particles are difficult to charge. If a large concentration of 0.2-0.8μm particles is in a flue, a large amount of particles within this size range will escape into the air from a DESP. These small particles will also escape into the air from a BH. Figure (1.1) gives measurements before and after the CFFF BH and DESP. It is known that this submicron size range of particles is particularly significant in affecting human health, the visibility though the air and water-droplet nucleation. Although these small particles may constitute a small fraction by mass, it is obviously important that they be collected effectively. In coal fired systems which use higher temperature combustion to attain increased efficiency, like magnetohydrodynamic (MHD), the number of these small particles increases, and so does the hazard they pose.

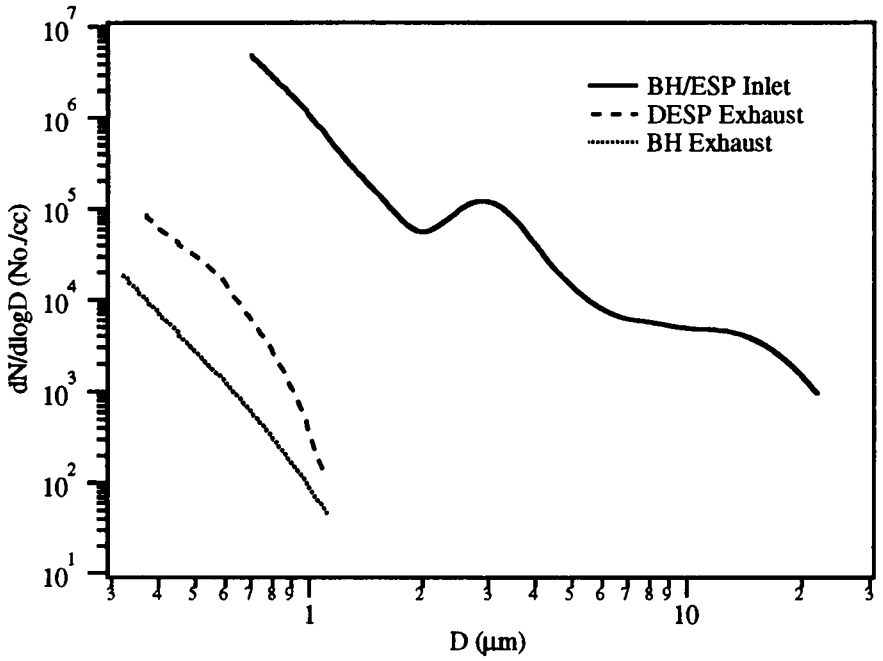


Figure 1.1 Particle Size Distribution Measured Before and After the CFFF BH&DESP

One alternative way to raise the collection efficiency of particle collection equipment, instead of improving their small particle performance, is to induce small particles agglomeration so that the total amount of particles, and small particles in particular, escaping into the air is reduced. Two techniques that can be used practically in certain fields for enhancing particle agglomeration have been pointed out by N. Fuchs.[2] One is the use of acoustic energy. In 1931, Patterson and Cawood first studied the effects of sound on aerosol dispersions.[3] Since then many sonic studies, such as the physical causes of sonic agglomeration, the generation of high frequency sound fields and the technology for large-scale industrial applications,[4,5,6] have been carried out in the United States. These papers were summarized in the well-known book on sonic agglomeration by Mednikov published in 1963.[7] Since acoustic agglomeration has its principal advantage in the ability to control particles of any size without a minimum in the collection efficiency, it is attractive for use as a preconditioner to conventional emission control devices for the effective removal of fine

particles. The other agglomeration technique is the electrical induction technique of applying alternating electrical current on the electrostatic precipitator electrodes. This technique was reported first by Melcher and Sachar.[8] They proposed that agglomeration would result from the combination of Coulomb attraction due to bipolar charging and the fluid-mechanical-turbulent-mixing caused by the charging wires. Both methods provide agglomeration but also have disadvantages, including intense noise production and excessive power consumption.

Another particle agglomeration technique is cold nuclei particle injection into a hot particle stream which flows in a duct. Various injections have been reported, for example sorbent.[9,10] Thermophoresis is the primary mechanism of fine particle agglomeration with this nuclei injection technique. Thermophoresis is an agglomeration process which occurs naturally in many flue gas flows. Because the balance of convection heat transfer on the surfaces of the particles and radiation heat transfer between the particles and the cooler wall of the flow duct, larger particles tend to have lower temperatures than smaller particles. Therefore, a temperature gradient that causes thermophoresis is established between the large and small particles, and smaller particles are attracted to larger particles to which they often adhere (i.e., they agglomerate).

Thermophoresis is not an new concept. It was first formulated by Epstein.[11] Particle deposition on the wall by thermophoresis is well known.[12,13,14,15,16] Use of thermophoresis for separation of aerosol was also reported.[17] Because the wall of a cooled duct or tube has a lower temperature than the gas inside, there is a temperature gradient between the flow and the wall. The thermophoretic force drives fine particles in the flow to the wall where they deposit. Now, because large particles also have low temperatures, they are similar to a cooled wall but with a very small surface area. Small particles deposit on the

surface of the large particles. Small particles will grow.[18,19] If there is a supersaturated vapor, condensation and nucleation will assist thermophoresis in producing particle growth. This is the coal fired flow facility (CFFF) superheater module situation at the University of Tennessee Space Institute (UTSI).[20]

1.2 General Descriptions of Current MHD System at UTSI

Figure (2.1) is a schematic of the open cycle coal-fired MHD CFFF facility located at UTSI (next page).

At the CFFF, coal is burned fuel rich in the primary combustor (upstream test train) with the help of preheated O_2/N_2 mixture to provide the high gas temperature (about 5000 ^oF) required to affect dissociation of potassium seed and subsequent formation of an electrically conductive plasma. Fuel rich combustion is used to reduce NO_x formation. The circular aerodynamic duct section substitutes for the MHD generator channel which converts this thermal energy into electrical energy. In this section the flow speed is transonic. After the circular aerodynamic duct the diffuser converts the plasma kinetic energy into thermal energy. Hence the diffuser slows the flow down to enter the radiant furnace which simulates a steam boiler. The furnace controls thermal relaxation of NO_x and the 90^o flow turn entering the furnace allows larger slag particle removal ballistically. Flow from the furnace enters the secondary combustor(SC). At the secondary combustor the combustion is completed utilizing secondary air. The flow at the secondary combustor contains slag, flyash, gaseous combustion products and seed. After the secondary combustor, the flow train has many sections. These sections form the superheater test module which simulates high, intermediate and low temperature heat exchange with saturated steam and is followed by an intermediate temperature airheater. The rest of the sections carry out particle

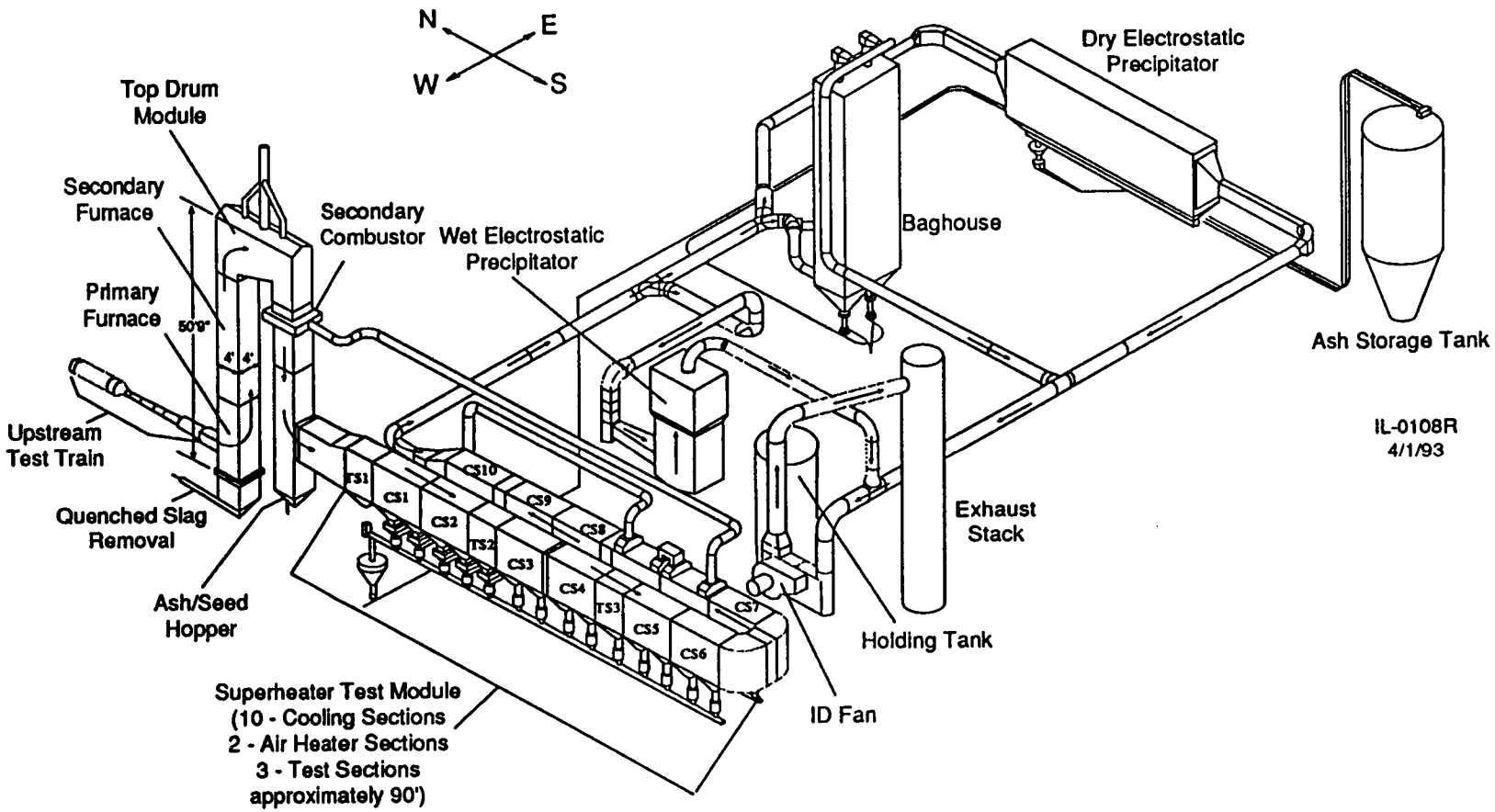


Figure 1.2 CFFF Schematic Diagram

collection with appropriate particle sampling as well as further cooling of the exhaust gases. The baghouse(BH), the dry electrostatic precipitator(DESP) and the wet electrostatic precipitator(WESP) are operated in parallel to allow comparison of particle removal capabilities in order to define the most appropriate particulate pollution control in scaled up plant designs.

At the radiant furnace, 80% of the ash is removed out of the system as slag. But 20% of the ash is carried through the downstream. Experimental data show that at the outlet of the secondary combustor the flow contains approximately 75% potassium and sulfur, 15% flyash and about 5% carbonates.[21] These products will be removed by the BH and ESP's as particles. Because the products have a very wide size distribution, generally from 0.01 micron up, the BH and the ESP can not remove the small particles effectively. Previous experiments indicate that the BH and the DESP demonstrate higher efficiencies in removing larger particles than smaller ones. Many submicron particles pass through these particle removal system along with the stack gases, and so pollute the air. When high submicron particle loadings occur as at the CFFF, the WESP is more efficient at removing the small particles, but the solubility of the flue gas potassium compound creates operational problems which have not been overcome. Since there are many submicron particles left in the flow leaving the DESP, in particular, methods to enhance the DESP performance are sought. One way to accomplish this is to drive submicron particles to agglomerate to larger size, e.g., larger than one micron, simplifying removal by both the BH and the DESP. Acoustic wave and electrical induction techniques are not efficiently effective for typical CFFF conditions.

Another advantage of forming large particles from the smaller ones is that it will raise the overall plant energy conversion efficiency. Large ash particles will reduce fouling by ash,

which is a poor thermal conductor, on the surfaces of the heat exchangers so that the heat transfer efficiency becomes higher with agglomerated particles than before. Im has examined this problem.[13] At the BH, the energy required to pump the flow will be reduced since the cake resistance by the small particles will be reduced and the pressure drop over the filter will be thus reduced not climb as fast, reducing the clearing cycle requirement. At the DESP, larger particles will be easier to collect as a smaller ESP might be used with less electrical power consumption for the same removal efficiency.

1.3 Objectives

The previous discussions indicate that efficient particle agglomeration could provide advantages to MHD particle emission concerns. Because acoustic wave and electrical induction techniques are not very effective for CFFF conditions, thermophoresis particle agglomeration is considered. An entire theory for cold particle injection to induce agglomeration and the growth, is developed in this dissertation. The particle injection technique is shown to overcome the disadvantages of the sonic wave and the electrical induction techniques because it does not generate excessive noise or consume excessive energy. Particle injection technique can achieve the desired agglomeration without flue gas chemical additives since the injected particles can be obtained from the coal-fired MHD system itself. An experiment, injecting cold particles collected by the DESP verified the theoretical results through measurement of particle size distribution before and after injection. This particle injection technique will be economic and convenient to use not only at the CFFF but other industries to improve submicron particulate capture.

The particle injection technique should achieve the following:

1. maximize individual submicron particle growth

2. minimize fractions of the smaller particles, especially for submicron particles,
3. minimize heat loss from the flow with low temperature particles (nuclei) injected.

The present work consists of two parts. The first part is a theoretical investigation. Since MHD flow after the secondary combustor is primarily a three-phase flow, possible heterogeneous nucleation and condensation growth are studied, especially under the condition of foreign solid particles being injected into this flow. For simplicity, this three-phase flow is considered to contain vapor, condensed potassium sulfate and solid fly ash particles. The injected particles are flyash and flyash with solid potassium sulfate.

After the secondary combustor and before the cooling section 1 of the superheater test module, the flow is in the supersaturated state. Condensation growth and nucleation are considered. Since there is a huge number of particles, particle collision is also considered as thermophoretic coagulation. Particle coagulation by thermophoresis is discussed in details. Particle collection efficiency and collision frequency are given with the presentation of the coagulation equation, which describes particle concentration changes with respect to time. Then both condensation growth and also nucleation is added to the coagulation equation. Because particles are injected into the flow at this section, the injection is also taken into the coagulation equation. Associated with this equation, the condensation growth rate and nucleation rate at different temperatures and supersaturated ratios are obtained. After the injection section, the temperature of the flow will decrease and the flow becomes two phase gas with solid particles. From this point only thermophoretic coagulation is considered.

The second part of this dissertation is an experimental study of thermophoresis agglomeration. The experiment was done at the CFFF with an injector at port 2503 in the

secondary combustor mixing regime, which locates just above the secondary combustor platform (see Chapter 3). Particles are collected at the BH and DESP of the CFFF. Particle size distribution is measured at the outlet of the secondary combustion and at the inlet of the BH and ESP by means of five-stage cyclone method, laser optical method by Insitec, Inc.,[22] and sample extraction&dilution system (SEDS) method.[23] The data show that lower submicron particle number densities and lower total number of particles with particle injection. These data are compared with the theoretical prediction developed in this dissertation.

CHAPTER 2 THEORY

The combustion products of the primary and the secondary combustor are chemically complex. The flow out of the secondary combustor has many chemical compounds existing in all three phases, including gaseous and liquid K_2SO_4 and K_2CO_3, and solid ash. A simplified model of this flow is developed to represent this three-phase flow, which is primarily considered to contain vapor with gases like N_2, NO_x, CO, and CO_2, and condensed liquid K_2SO_4, and solid flyash particles existing the secondary combustor. This location was selected for particle injection because by this point the flow has become oxidizing and cooled significantly for most of the vapor K_2SO_4 to be nucleated homogeneously to very small liquid and solid particles of submicron sizes. When cold particles are injected at this location, there are many complex agglomeration processes, (e.g., thermophoretic coagulation, heterogeneous nucleation, and condensation), which takes place simultaneously as well as sequentially in the CFFF flow train. In this dissertation, the heterogeneous nucleation, condensation, thermophoresis, and injection will be discussed. This theoretical work is divided into two major fields. The first field includes the particle injection section from the exit of the secondary combustor to the entrance of the cooling section 2 (CS2). The second field includes the flow from the CS2 to the inlet of the ESP and BH. In the second field, there are 14 different temperature cooling and test sections between the CS1 and the DESP.

2.1 Dynamic Behavior of a Single Particle

2.1.1 Equation of Motion

A motion of a single particle in the flow is considered to respond to the forces of drag and thermophoresis. Since the Reynolds number is less than one, the drag force can be expressed as the Stokes formula $6\pi\mu r_0\vec{V}$, where r_0 is the radius of the particle and μ is the gas viscosity and $\vec{V}$ is the particle velocity. The thermophoretic force was given by J. R. Brock.[24] Accordingly, the equation of motion of the single particle of mass m with temperature, T_0, lower than that of the flow and injection velocity $\vec{V}_0$ with angle θ with respect to the direction of the flow, which is assumed to be parallel to the flow train and to have a constant velocity $\vec{V}_f$, is given as:

$$m\frac{d^2\vec{r}}{dt^2} = \vec{F} - 6\pi\mu r_0\frac{d\vec{r}}{dt} + 6\pi\mu r_0\vec{V}_f \qquad (2.1.1.1)$$

In this case, $\vec{F}$ is the thermophoretic force applied on the particle and is considered as a constant [see Appendix B]. Figure (2.1.1) illustrates the forces on the particle.

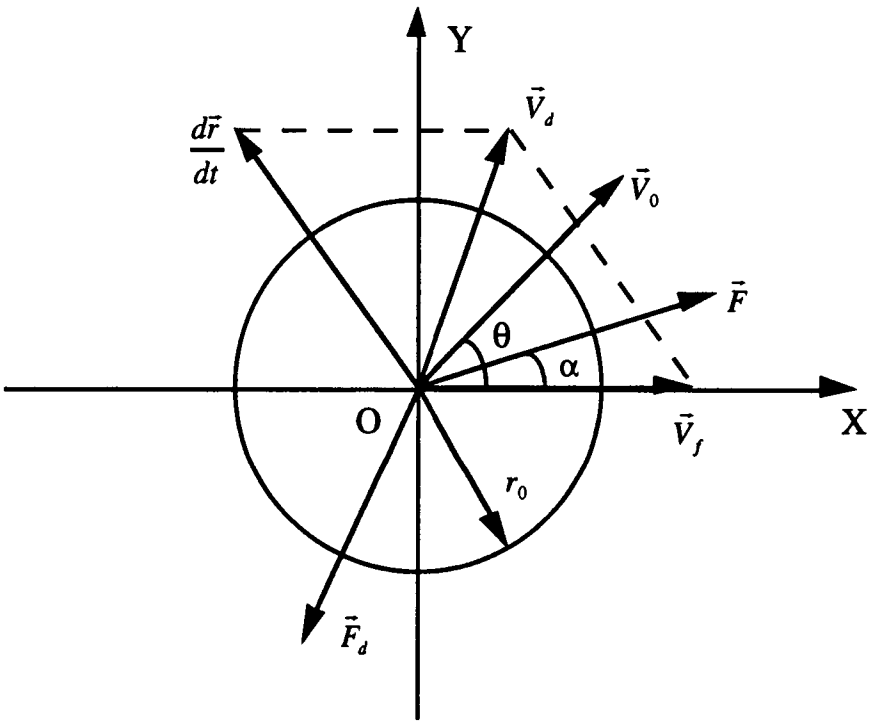


Figure 2.1.1 Single Particle in a Flow

In the x-direction, Eq.(2.1.1.1) becomes:

$$m\frac{d^2x}{dt^2} = F_x - 6\pi\mu r_0(\frac{dx}{dt} - V_f) \tag{2.1.1.2}$$

and in the y-direction:

$$m\frac{d^2y}{dt^2} = F_y - 6\pi\mu r_0\frac{dy}{dt}. \tag{2.1.1.3}$$

2.1.2 Behavior of the Particle

The initial conditions are $t=0$, $x=y=0$, $\dot{x} = V_0\cos\theta$ and $\dot{y} = V_0\sin\theta$. Solutions to Eqs.(2.1.1.2) and Eq.(2.1.1.3) are:

$$x = \frac{m}{6\pi\mu r_0}(V_0\cos\theta - \frac{F_x}{6\pi\mu r_0} - V_f)(1 - e^{-\frac{6\pi\mu r_0 t}{m}}) + (\frac{F_x}{6\pi\mu r_0} + V_f)t \tag{2.1.2.1}$$

$$y = \frac{m}{6\pi\mu r_0}(V_0\sin\theta - \frac{F_y}{6\pi\mu r_0})(1 - e^{-\frac{6\pi\mu r_0 t}{m}}) + \frac{F_y}{6\pi\mu r_0}t \tag{2.1.2.2}$$

When only drag and thermophoretic force apply on the particle, the trajectory of the particle is given by:

$$r = \sqrt{x^2 + y^2}, \quad \varphi = \arctan\frac{y}{x}. \tag{2.1.2.3}$$

The thermophoretic force (F_x, F_y) can be calculated by Eq.(B.3) when all parameters are given. Typical data are

C_m=1.14

C_s=1.17

C_t=2.18

r_0=1.0 μm

λ=0.1 μm

k_g=0.03 W/m-K

k_p=0.198 W/m-K

ρ_g=0.14 kg/m^3

ρ_p=2500 kg/m^3

μ=5.0x10^{-5} kg/m-sec.

T_0=1442 K

T_p=600 K

The numerical solution of the equation of the motion of the injected particle and its trajectory are plotted on page 15 to page 18.

From the Figure (2.1.2), it can be seen that particle's displacement is nearly linearly dependent on time and is dependent on the radius of the particle. In Eqs.(2.1.2.1) and (2.1.2.2), the ratio of the mass m to $6\pi\mu r_0$ is very small, which causes the linear time dependence. For example, for a particle of 1.0μm radius,

$$\frac{m}{6\pi\mu r_0} = \frac{\frac{4}{3}\pi\rho r_0^3}{6\pi\mu r_0} = \frac{2}{9}\frac{\rho}{\mu} r_0^2 = \frac{2\times 2500.\times(1.0\times10^{-6})^2}{9\times 5.0\times10^{-5}} = \frac{1.\times10^{-4}}{9} \approx 10^{-5}.$$

and

$$\frac{6\pi\mu r_0}{m} = 10^5 \text{ and } 1 - e^{-\frac{6\pi\mu r_0}{m}t} \approx 1 \text{ if } t \text{ is not extremely small.}$$

Therefore, the first term in Eqs.(2.1.2.1) and (2.1.2.2) is not very important. The trajectory can be rewritten as

$$r \approx \frac{t}{6\pi\mu r_0}\sqrt{\left(F_x + 6\pi\mu r_0 V_f\right)^2 + F_y^2} \quad \text{if t is not extremely small.} \tag{2.1.2.4}$$

Thus, the displacement is nearly linearly dependent on time.

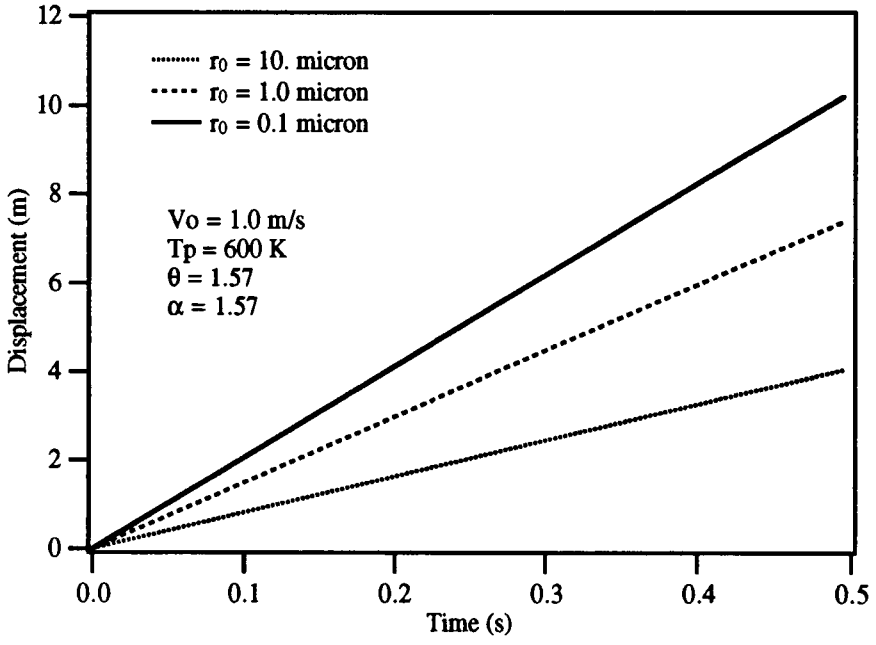


Figure 2.1.2 Particle Displacement vs. Time

Additionally, this relation, Eq.(2.1.2.4), explains Figure (2.1.3) since it shows the trajectory to be inversely proportional to the radius of the particle, r_0. Since the thermophoretic force is proportional to the local temperature gradient [Appendix B], and the temperature gradient at the surface of the particle is expressed as

$$\frac{\nabla T}{T} = \frac{T_f - T_p}{T_f} \cdot \frac{1}{r_0}, \tag{2.1.2.5}$$

the trajectory of the particle is also nearly linearly dependent on the temperature of the particle as can be seen in Figure (2.1.4).

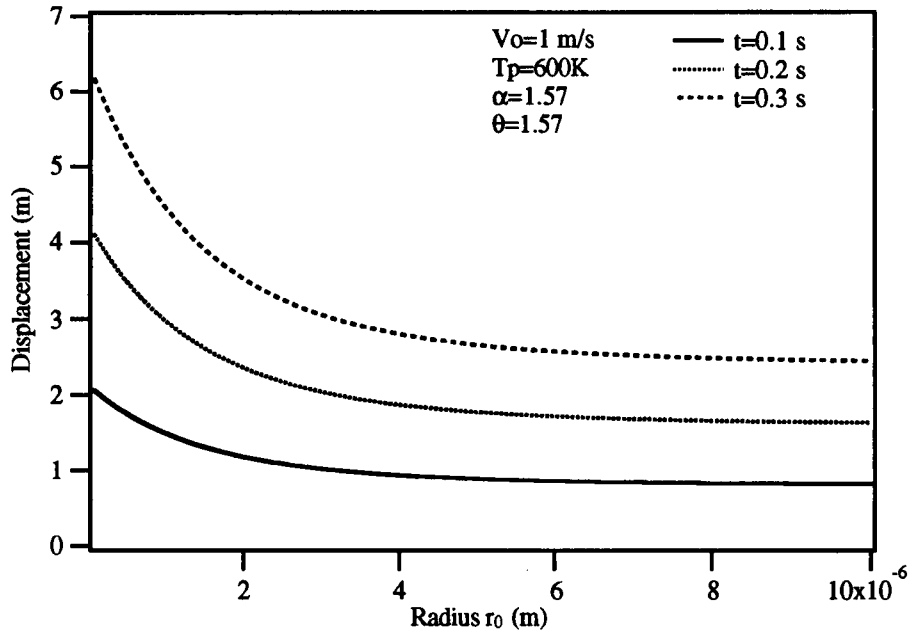


Figure 2.1.3 Particle Displacement vs. Radius

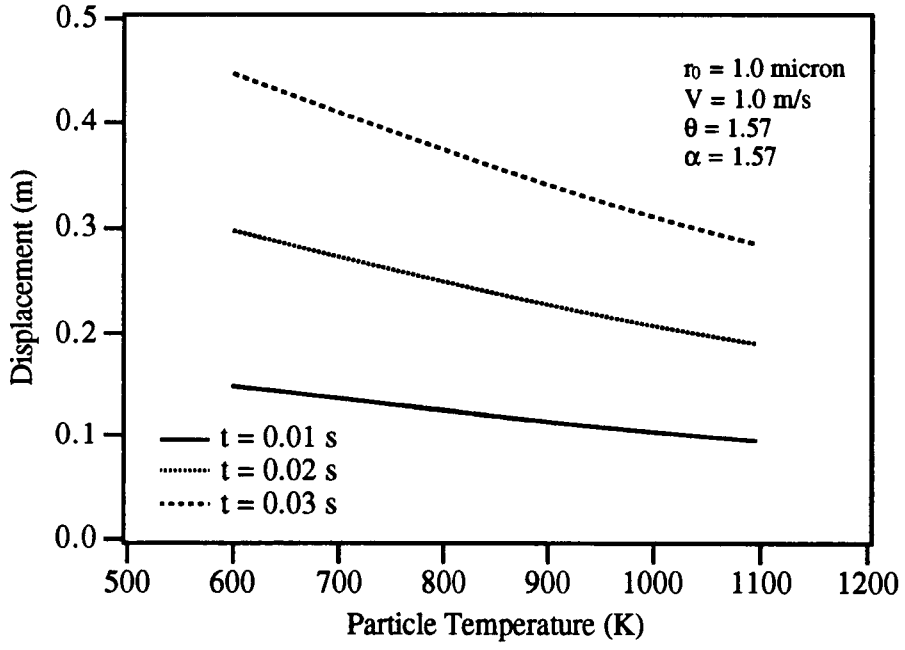


Figure 2.1.4 Particle Displacement vs. Particle Temperature

Figures (2.1.5) indicates that the injection angle is not an important factor for injecting a small particle, such as a particle of 1.0μm. The displacement of the particle changes from 1.4902m to 1.4904m at $t=0.1s$ after the particle is injected.

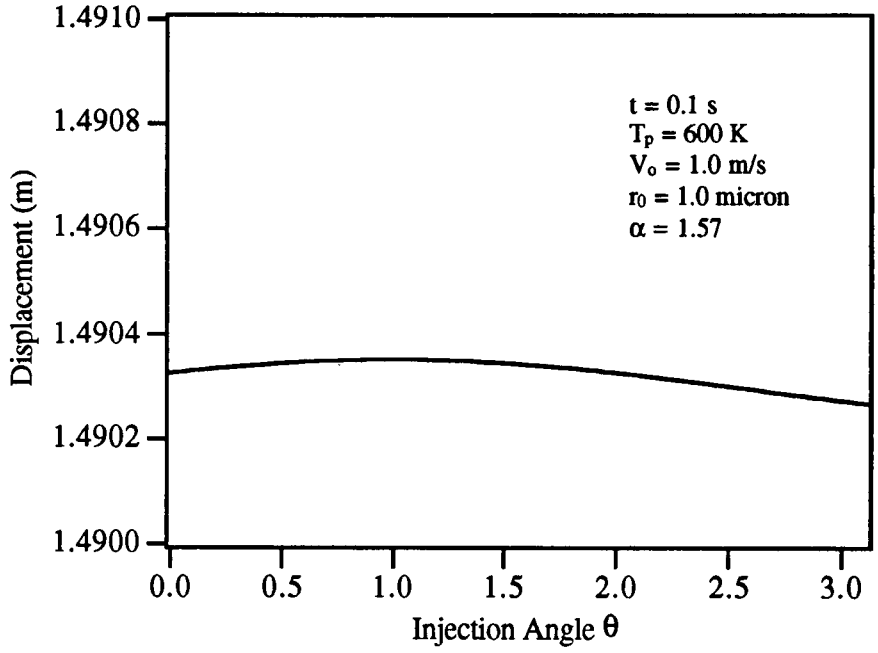


Figure 2.1.5 Particle Displacement vs. Injection Angle

Figure (2.1.6) indicates that injection velocity is not an important factor for injecting small particle near the size of one micron because when the injection velocity changes from very small velocity to 20m/s, the displacement of the injected particle changes only approximate 0.01m.

It can be concluded from Figures (2.1.2-2.1.6) that injected very small particles, such as r_0=1.0μm, will go with the main flow right after they are injected. Different injection velocity and angle may affect only on mixture of two flows.

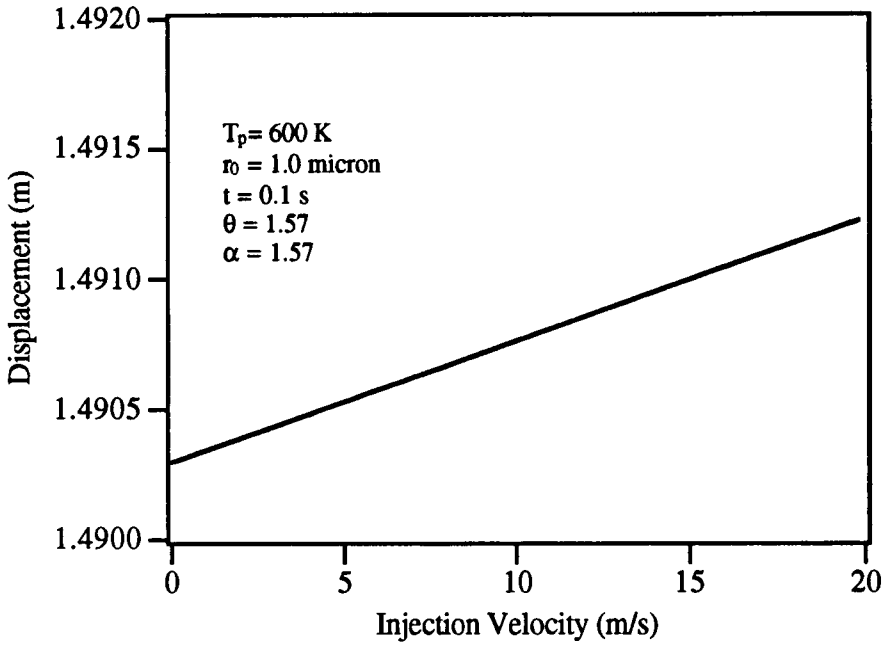


Figure 2.1.6 Particle Displacement vs. Injection Velocity

It is desired that injected particles penetrate deep into the primary flow and maintain their low temperatures as long as possible so that they are able to collect more small particles by thermophoresis. Micron size particles will reach their equilibrium temperatures very quickly (i.e., 10^{-3} sec.) due to convection heat transfer. However, particles of different sizes have different equilibrium temperatures because of the differences in the heat balance between convection heating at the surface of the different particles and radiation cooling with the cooler walls of flow ducting. Larger particles have lower temperatures than smaller particles. These temperature differences cause local temperature gradients at the surfaces of the particles and thus thermophoresis attracts small particles to large particle as they flow down the ducting.

2.2 Particle Collection Efficiency and Collision Frequency

2.2.1 Particle Collection Efficiency

Collection efficiency is defined[25] as the ratio of the relative volume cleared of small particles to the volume occupied by one large particle as shown in Figure (2.2.1).

$$\eta_{ij} = \frac{\frac{4}{3}\pi(R_i^3 - r_j^3)}{d^3}. \qquad (2.2.1.1)$$

The distance between particles i and j, R_i, is related to the thermophoretic velocity of particle i. It is assumed that r_i is less than r_j and the j particle is relatively still. d is the separation distance of two adjacent j particles, which is approximately equal to $1/n_j^{1/3}(t)$. where $n_j(t)$ is the number concentration of the particle of size r_j.

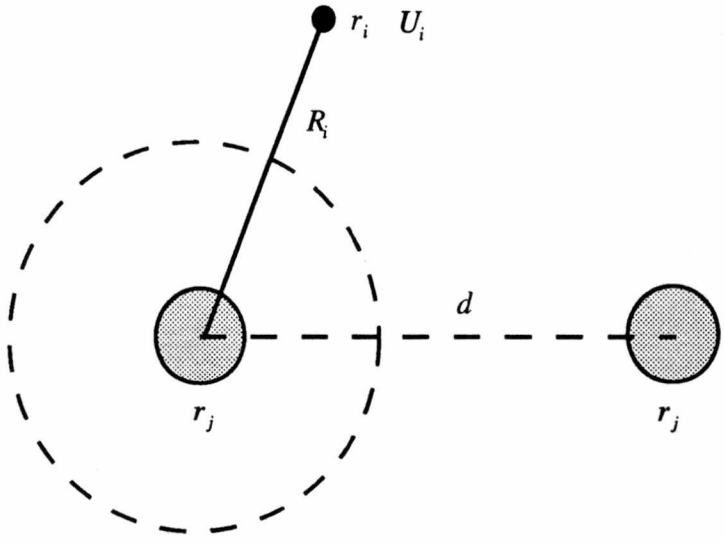


Figure 2.2.1 Definition of Collection Efficiency of Particle

Since thermophoretic force for fine particle agglomeration is caused by the temperature difference between the large and small particles, which the larger particles have lower temperatures and small particles, however, have negligible temperature difference from gas. All particles are assumed to be spherical in shape.

Now temperature gradient is considered in the neighborhood of the large particle by balancing the heat flux at the surface of the large particle. The convection and conduction heat flux are

$$\dot{q}" = h(T_g - T_p) \tag{2.2.1.2}$$

and

$$\dot{q}" = -k_g \left.\frac{dT}{dR}\right|_{r_j}. \tag{2.2.1.3}$$

Then equating Eq.(2.2.1.2) and Eq.(2.2.1.3) and simplifying,

$$\left.\frac{dT}{dR}\right|_{r_j} = -(T_g - T_p)\frac{h}{k_g}. \tag{2.2.1.4}$$

In the system, since the Nusselt number is about 2.0,[25] it gives

$$\frac{hD_j}{k_g} = 2.0. \tag{2.2.1.5}$$

or

$$h = \frac{k_g}{r_j}. \tag{2.2.1.6}$$

Referring to Appendix B, the term T_0 represents the mean temperature in the neighborhood of the large particle and this can be taken to be gas temperature, T_g. Therefore, at the surface of the large particle

$$\frac{\nabla T}{T_o} = \frac{\nabla T}{T_g} = -\frac{T_g - T_p}{r_j}\frac{1}{T_g} \tag{2.2.1.7}$$

The thermophoretic velocity calculated by using this temperature gradient is the value at the surface of the large particle.

When a small particle is away from a large particle a distance R, the velocity of the small particle will be proportional to the inverse square of R. For the large particle, the heat flux out of its surface is given by Eq.(2.2.1.3). At the distance R, the heat flow will be

$$\dot{q} = 4\pi R^2 \dot{q}''. \tag{2.2.1.8}$$

Substituting Eq.(2.2.1.2) into Eq.(2.2.1.8) and rearranging,

$$\frac{dR}{R^2} = -4\pi k_g \frac{dT}{\dot{q}}. \tag{2.2.1.9}$$

Integrating it and applying at $R=r_j$, $T=T_p$ and $R \to \infty$, $T=T_g$, then Eq.(2.2.1.9) reduces to

$$\dot{q} = -4\pi k_g (T_g - T_p) r_j. \tag{2.2.1.10}$$

Substituting Eq.(2.2.1.10) back into Eq.(2.2.1.9) and applying it at $r=r_j$ and $r=r$, it gives

$$\left.\frac{dT}{dR}\right|_R = \frac{r_j^2}{R^2}\left.\frac{dT}{dR}\right|_{r_j}. \tag{2.2.1.11}$$

Finally, the thermophoretic velocity at a distance R from the large particle is

$$U_t|_R = \frac{dT}{dR} = -\frac{r_j^2}{R^2} U_t|_{r_j}. \tag{2.2.1.12}$$

since

$$U_t \propto \frac{dT}{dR}. \tag{2.2.1.13}$$

The temperature of the large particle, T_p, will be obtained by balancing radiation heat flux and convection heat flux for the large particle. In the coal-fired system, most of the large particles are ash, which primarily consists of silica. For the range of temperature of interest here, the emissivity of silica varies from 0.7 to 0.84. And 0.8 was used as a suitable approximation for emissivity. The particle temperature can be calculated from Eq.(2.2.1.14)

$$h(T_g - T_p) = \varepsilon\sigma(T_p^4 - T_w^4). \tag{2.2.1.14}$$

It is assumed that small particles within a distance R_i from a large particle will be collected by the large particle. Integration of Eq.(2.2.1.12) from $r=r_j$ to $r=r_i$ during the residence time δt gives

$$(R_i^3 - r_j^3) = 3r_j^2 U_{ri}\delta t. \tag{2.2.1.15}$$

Finally, the collection efficiency is

$$\eta_{ij} = 4\pi r_j^2 U_{ri}\delta t_i n_j. \tag{2.2.1.16}$$

Figure (2.2.2) gives temperatures of particles of various sizes. It shows that smaller particles have higher temperatures and larger particles have lower temperature as low as 40K than the gas temperature. Figure (2.2.3) gives the collection efficiencies of large particles to small particle of size of 0.1μm at section TS1. It can be seen that smaller large particle has higher collection efficiency to the same small particles.

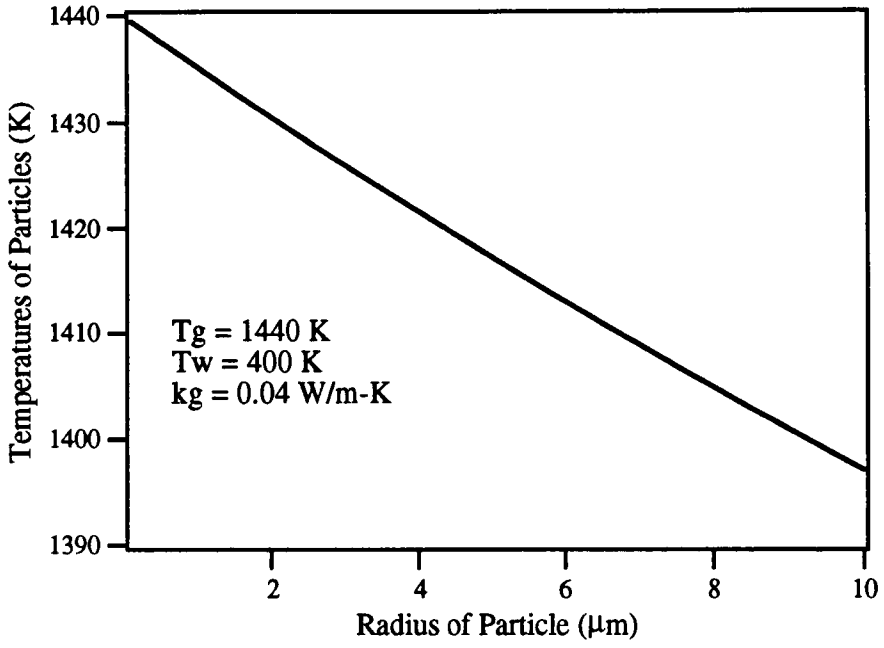


Figure 2.2.2 Temperature of Particle vs. Particle Size

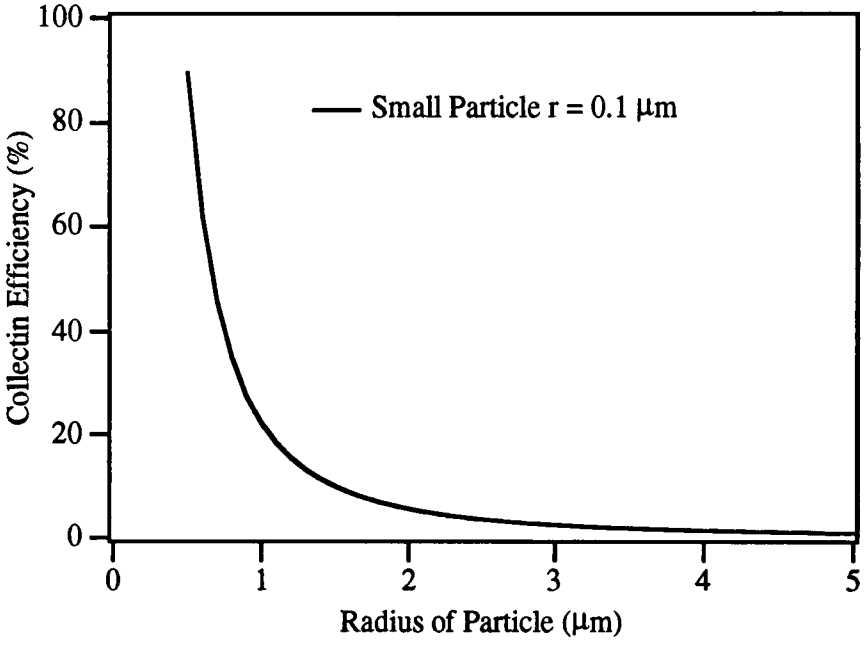


Figure 2.2.3 Collection Efficiency vs. Particle Size with $r_j >> r_i$

2.2.2 Particle Collision Frequency

The present problem of the dynamics of particle agglomeration falls into the category of collisions due to differential settling. Therefore, the collision frequency function can be written in the form

$$b_{ij} = b_{ij}(r_i, r_j) = Q(r_i, r_j) g(r_i, r_j), \tag{2.2.2.1}$$

where $Q(r_i, r_j)$ is the collision cross section and $g(r_i, r_j)$ is the relative speed between particles of volume r_i and r_j. The cross section can be expressed as

$$Q(r_i, r_j) = \eta_{ij} \pi (r_i + r_j)^2, \tag{2.2.2.2}$$

where η_{ij} is the collection efficiency. For a particle responding only to the thermophoretic and drag force, the velocity, U_t, is given by Eq.(B.6) and, therefore, the relative speed between two particles with radii r_i and r_j is

$$g(r_i, r_j) = \left| U_{ti} - U_{tj} \right| \tag{2.2.2.3}$$

The resultant frequency function becomes

$$b_{ij} = \eta_{ij} \pi (r_i + r_j)^2 \left| U_{ti} - U_{tj} \right|. \tag{2.2.2.4}$$

2.3 Studies of Particle Size Distribution (PSD)--Modified Coagulation Equation

An equation governing the time rate of change of the distribution function f_i may be derived phenomenologically by using reasoning analogous to that employed in the kinetic theory of gases. The force per unit mass on a particle of kind j at $(r, \vec{x}, \vec{v}, t)$ is denoted by

$\vec{F}_j = d\vec{v}_j / dt$ and the rate of change of the size r of a particle of kind j at $(r,\vec{x},\vec{v},t)$ is defined as $\dot{r}_j = dr_j / dt$. Both $\dot{r}_j$ and $\vec{F}_j$ are allowed to depend on $(r,\vec{x},\vec{v},t)$ and the local properties of the gas. The rate of increase of fj with time due to particle formation or destruction by processes such as nucleation or liquid break-up will be denoted by Q_j. Finally, Γ_j will represent the rate of change of the distribution for particle of kind j caused by collisions with other particles. These collisions must occur sufficiently seldom that the aerodynamic contributions to Γ_j are separable from those due to $\vec{F}_j$. Adding the changes in f_j resulting from particle growth, the motion of particles into and out of the spatial element $d\vec{x}$ by virtue of their velocity $\vec{v}$, the change of the number of in the velocity element $d\vec{v}$ because of the acceleration $\vec{F}$, sources of droplet Q_j and collisions Γ_j, one can define in one dimension,[26,27,28,29]

$$\frac{\partial f_j}{\partial t} = -\frac{\partial}{\partial r}(\dot{r}_j f_j) - \nabla_x \cdot (v f_j) - \nabla_x \cdot (F_j f_j) + Q_j + \Gamma_j, \quad j = 1,..m. \tag{2.3}$$

In this equation the distribution function can be replaced by the particle number concentration function $n_j(r,\vec{x},\vec{v},t)$.

In this dissertation, evolution of the particle size distribution is governed by Eq.(2.3), which is called the modified coagulation equation. The coagulation equation is modified with particle injection, condensation, and heterogeneous nucleation. Also, it is assumed that the flow velocity and external force $\vec{F}_j$ are constant, and the variation of particle number density within dx is very small. The second and third terms on the right hand side of Eq.(2.3), therefore, can be neglected. Particle injection, condensation, and heterogeneous nucleation will be discussed separately. Finally, the modified coagulation equation with all three phenomena will be discussed.

2.3.1 Coagulation Equation

In order to discuss the dynamic equation describing the time rate of change of the particle size distribution during the agglomeration process, the continuous size distribution is conveniently broken into a discrete spectrum with a size interval Δd_k for the size class k. All the particles belonging to class k are assumed to have the same size d_k, which is a midpoint of the size interval. By defining n_k as the number of particles per unit volume in the size class k, the net rate of change in n_k owing to the agglomeration process can be expressed as

$$\frac{dn_k(t)}{dt} = \frac{1}{2}\sum_{i+j=k} b_{ij} n_i n_j - n_k \sum_{i=1}^{\infty} b_{ik} n_i, \quad k = 1,2..... \tag{2.3.1.1}$$

The first term on the right hand side of Eq.(2.3.1.1) represents the collision of particles of sizes i and j to form particles of size k while the second term represents collision of particles of size i and k to destroy particles of size k. This equation was first discussed by Smoluchowski.[30,31]

The variation with time of the total concentration of particles is of interest. The rate of change in the total number of particles per unit volume $N(t)$ can be obtained easily by summing n_k over all values of k:[32,33]

$$\frac{dN(t)}{dt} = -\frac{1}{2}\sum_{i=j}^{\infty}\sum_{j=1}^{\infty} b_{ij} n_i n_j. \tag{2.3.1.2}$$

For the simplest case, if $b_{ij}=b_0$ (constant), Eq.(2.3.1.2) can be solved:

$$N(t) = \frac{2N_0}{2 + b_0 N_0 t} \quad \text{and} \quad N_0 = \sum_{k=1}^{\infty} n_k(0). \tag{2.3.1.3}$$

This expression can be used to check numerical solutions when b_{ij} = *constant.*

Because of the complexities of the coagulation equation, no general solution have been found for a variable collision parameter b_{ij}. This equation has to be solved numerically.

2.3.1.1 Numerical Solution of the Coagulation Equation

Since the particle number concentration may be very high (i.e., 10^{+16} particles/m^3), the nonlinear terms on the right hand side of the Eq.(2.3.1.1) may cause divergent. To avoid this, time step of computation must be very small (i.e., 10^{-8} sec.) and the computer time will be very long. Thus, the coagulation equation has to be modified to simplify solution.[34,35] Let

$$N_0 = \sum_{j=0}^{\infty} n_j(0), \quad \tau = 4\pi r_0 D_0 N_0 t. \tag{2.3.1.4}$$

D_0 and r_0 are reference dimension and diffusivity, respectively. The coagulation equation (2.3.1.1) can be rewritten as

$$\frac{d\hat{n}_k(t)}{d\tau} = \frac{1}{2} \sum_{i+j=k} \hat{b}_{ij} \hat{n}_i \hat{n}_j - \hat{n}_k \sum_{i=1}^{\infty} \hat{b}_{ik} \hat{n}_i. \tag{2.3.1.5}$$

where dimensionless parameters are defined as $\hat{n}_j = n_j / N_0$ and $\hat{b}_{ij} = b_{ij} / (4\pi r_0 D_0)$. This equation can be solved by Runge-Kutta time integration. Since coal ash particles have a typical log-normal distribution after combustion, it is assumed that the initial particle distribution has a log-normal form:

$$n(0) = \frac{n_0}{\sqrt{2\pi}\sigma r} e^{-\frac{(\ln r + a)^2}{2\sigma^2}} \quad \text{with } n_0 = 2\times 10^{13}/m^3, \sigma = 0.8 \text{ and } a = 14.0 \tag{2.3.1.6}$$

This initial distribution and numerical solutions after 0.5 and 1.0 second are plotted in Figure (2.3.1). From this plot, it is clear that the maximum values of particle size distribution decrease 1.6 times after 0.5 second and 2.5 times after 1.0 second, and number density increases at larger size. 200 particles were used here.

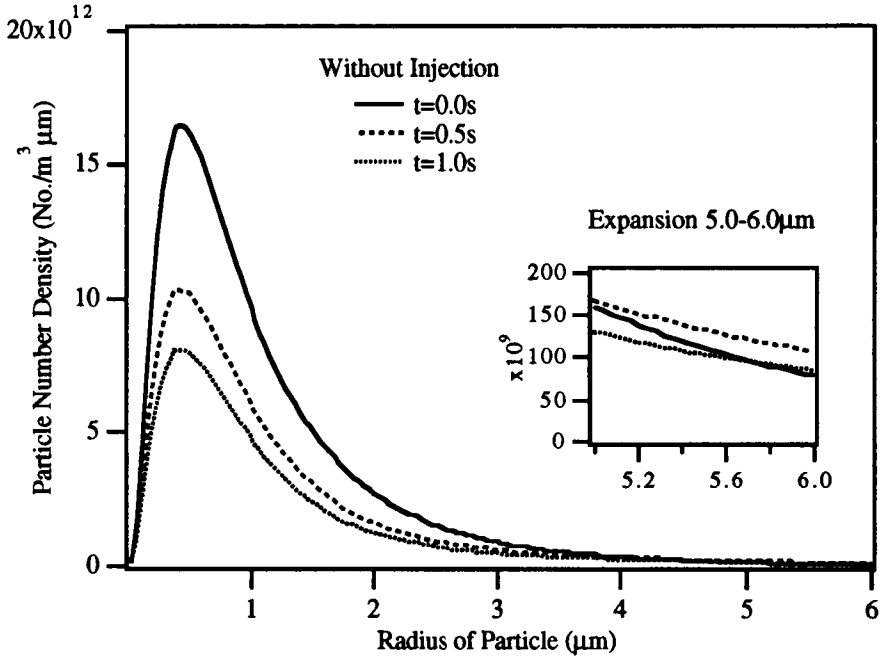


Figure 2.3.1 Numerical Solution of Coagulation Equation

2.3.1.2 Characteristic Time for Agglomeration

To examine the effects of agglomeration on the smaller particles, the following approximations can be made in Eq.(2.3.1.1), assuming that k is sufficiently small.

(1) The first term on the right hand side can be ignored in comparison with the second term.

(2) The second term on the right-hand side is bounded, which is

$$\begin{aligned} b_{ik} &= 4\pi^2 r_i^2 n_i U_k |U_k - U_i| (r_i + r_k)^2 \delta t \\ &\le 4\pi^2 r_i^2 n_i U_k{}^2 (r_i + r_k)^2 t \quad \text{if} \quad r_k \le r_i \\ &\le 4\pi^2 r_i^2 n_i U_k{}^2 4 r_i{}^2 t \\ &= 16\pi^2 r_i^4 n_i U_k{}^2 t \end{aligned} \tag{2.3.1.7}$$

Generally, if k is very small, $r_k \le r_i$ is an appropriate assumption. Appendix B shows that $U_k > U_i$, if $r_k < r_i$, and U_k is independent of n_k. Now, Eq.(2.3.1.1) can be approximated as

$$\begin{aligned} \frac{dn_k}{dt} &= -16\pi^2 U_k{}^2 n_k t \sum_{i=1}^{\infty} r_i^4 n_i^2 \\ &= -U_k{}^2 n_k t \sum_{i=1}^{\infty} (4\pi r_i^2 n_i)^2 \\ &= -U_k{}^2 n_k t \sum_{i=1}^{\infty} S_i^2 \\ &= -U_k{}^2 S_{tot}^2 n_k t \end{aligned} \tag{2.3.1.8}$$

where

$$S_{tot}^2 = \sum_{i=1}^{\infty} S_i^2 \quad \text{and} \quad S_i = 4\pi r_i^2 n_i. \tag{2.3.1.9}$$

S_{tot} is total surface area of particles in an unit volume. Eq.(2.3.1.8) can be solved as

$$n_k = n_k(0) \exp\left(-\frac{t^2}{\tau_0^2} \right) \tag{2.3.1.10}$$

where

$$\tau_0 = \frac{\sqrt{2}}{U_k S_{tot}}. \qquad (2.3.1.11)$$

defines the characteristic time for small particle agglomeration.

2.3.2 Coagulation Equation with Particle Injection

When particles are injected into the original flow, the coagulation equation can be rewritten as[36]

$$\frac{dn_k(t)}{dt} = \frac{1}{2}\sum_{i+j=k} b_{ij} n_i n_j - n_k \sum_{i=1}^{\infty} b_{ik} n_i + Q_k. \qquad (2.3.2.1)$$

where $n_k(r,t)$ is still the particle number concentration of size k particles, b_{ij} is still the collision frequency of the particles of size i and j and Q_k is the rate of k size of particles injected into the system. It is assumed that the particles injected have a size distribution $n_S(r)$ and a injection velocity V. If a injector has cross area A , the total mass loading, therefore, is

$$\dot{M} = \sum_k \frac{4\pi}{3} r_k^3 \rho n_{k,s}(r) VA. \qquad (2.3.2.2)$$

If the interaction length of the flow is L_0, Q_k is given by

$$Q_k = \frac{n_{k,s} V}{L_0}. \qquad (2.3.2.3)$$

When the particles are injected, the particle collection efficiency is rewritten as

$$\eta_{ij} = 4\pi r_j^2 U_{ri} \delta t_i (n_j + n_{j,s}). \qquad (2.3.2.4)$$

Note that when two flows are mixed together, many complicated processes may occur, including both physical and chemical interactions, which can result in temperature change, pressure change, chemical potential changes, etc.. In this dissertation, these effects are neglected and the mixture is assumed to be well mixed. Since the mass loading of the injected particles is relatively small with respect to the original flow, the only concerns are the particle interaction in the mixture of the two flows, and the condensation and nucleation of K_2SO_4 vapor onto the particles and droplets in both the original and the injected particle flows. Thus, the theory used here is to simply add the source term Q_k to the coagulation equation.

As mentioned before, a 1.0 micron particle reaches its equilibrium temperature very quickly. Thus, the small injected particles having lower temperatures than that of the flow will reach their equilibrium temperatures quickly as they obey Eq.(2.2.1.14). This transition to equilibrium temperatures is neglected in the dissertation because it occurs so rapidly.

For the injection process, two parameters, V and $n_S(r)$, can be adjusted. Other parameters, A, L_0, and ρ, depend on the type of the injector and type of the particle material injected. The interaction length also depends on the injection velocity. A can be found in Appendix I. At the CFFF, because of limited experimental conditions, the only parameters that could be changed were $n_S(r)$ and V. Thus, only the effects of $n_S(r)$ and V will be studied theoretically with A being a constant and L_0 being a unit length for a fixed injector. Since the injection material is CFFF flyash, its ρ is a known 2500 kg/m^3.

The modified coagulation equation, Eq.(2.3.2.1), has to be solved numerically. With introduction of Eq. (2.3.2.3) and (2.3.2.4), Eq. (2.3.2.1) can be rewritten as

$$\frac{d\hat{n}_k(t)}{d\tau} = \frac{1}{2}\sum_{i+j=k}\hat{b}_{ij}\hat{n}_i\hat{n}_j - \hat{n}_k\sum_{i=1}^{\infty}\hat{b}_{ik}\hat{n}_i + \hat{Q}_k. \tag{2.3.2.5}$$

where the dimensionless parameters are defined as $\hat{n}_j = n_j / N_0$, $\hat{b}_{ij} = b_{ij} / (4\pi r_0 D_0)$ and $\hat{Q}_k = Q_k / (4\pi r_0 D_0 N_0^2)$, where r_0 and D_0 are the reference radius and diffusivity, respectively.

First, a particle flow containing particles of a single size (radius) r_j is studied. Thus the particle size distribution of the injected particles is given as

$$n_s(r) = n_0\delta(r - r_j). \tag{2.3.2.6}$$

Under this assumption, the total mass flow can be rewritten as

$$\dot{M} = \sum_k \frac{4\pi}{3} r_k^3 \rho n_{k,s}(r) VA = \frac{4\pi}{3}\rho n_0 r_j^3 VA\delta(r - r_j). \tag{2.3.2.7}$$

And

$$Q_k = \frac{n_0 V}{L}\delta(r_k - r_j). \tag{2.3.2.8}$$

This modified coagulation equation can be solved numerically using Runge-Kutta method. Computed changes in the particle size distribution are given for different constant radius particles injection cases on page 33 to page 36. Figures (2.3.2.1), (2.3.2.2), and (2.3.2.3) have the same injection mass flux and injection velocity, but different injection particle sizes (2μm, 4μm, 6μm) and different injected number particle densities ($16\text{x}10^{+12}/\text{m}^3$, $2\text{x}10^{+12}/\text{m}^3$, $0.6\text{x}10^{+12}/\text{m}^3$), respectively. It can be seen from these three figures that if injection mass flux is fixed, and thus smaller size particles have higher number densities, higher agglomeration of smaller particles will result.

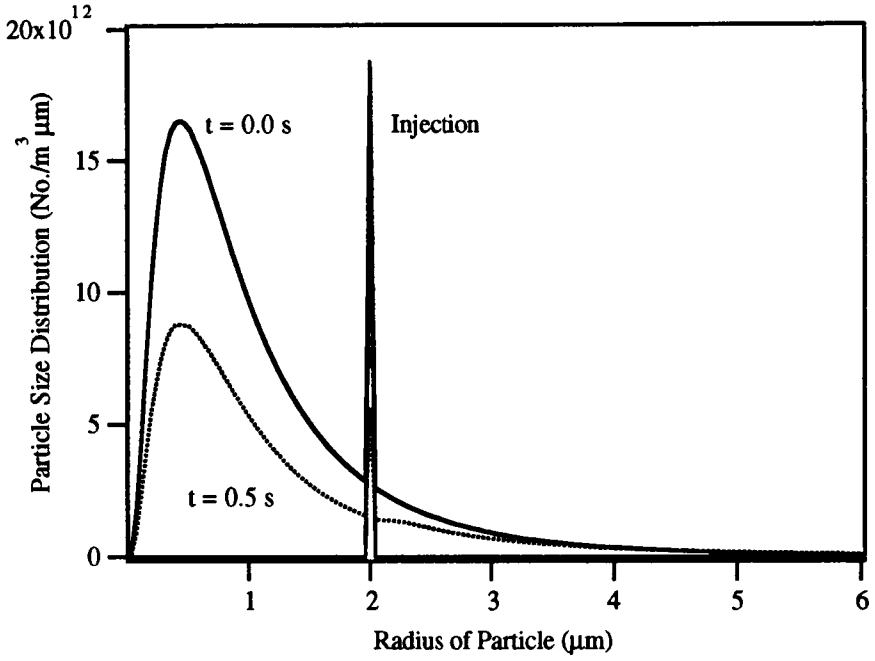


Figure 2.3.2.1 Injection at $r = 2\mu m$ with $V = 1.0$ m/s

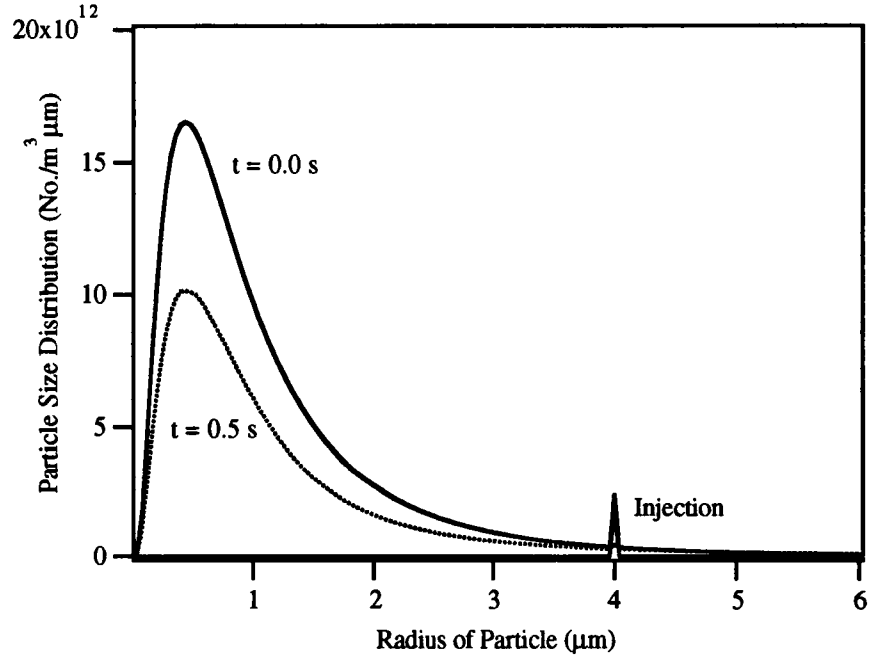


Figure 2.3.2.2 Injection at $r = 4\mu m$ and $V = 1.0$ m/s

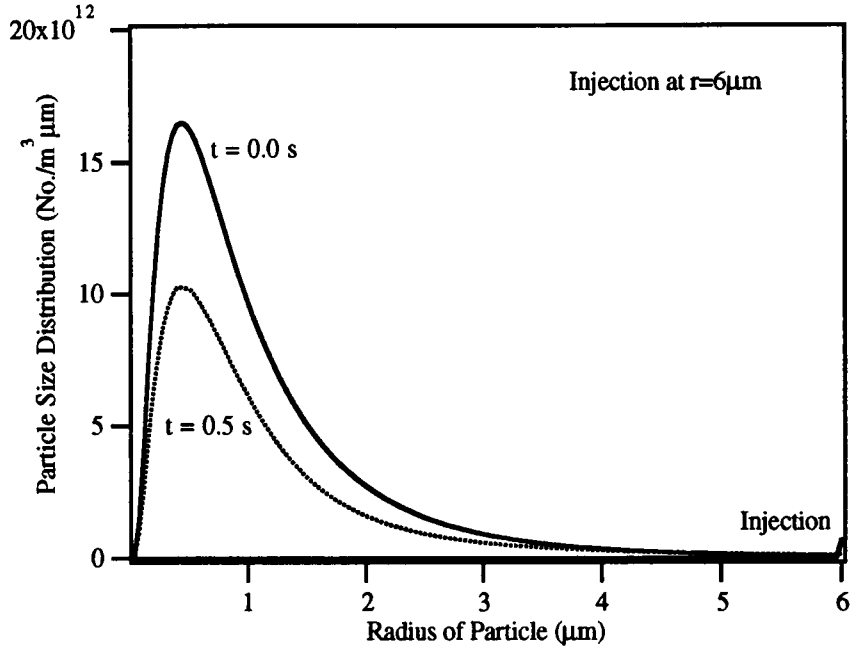


Figure 2.3.2.3 Injection at r = 6 μm with V = 1.0 m/s

Figures (2.3.2.1) and (2.3.2.4) have the same injection particle size (2μm) and injected particle number density, $16x10^{+12}$ /m^3, but different injection velocities, V = 1.0 m/s and V = 0.1 m/s, respectively. Consequently, they have different injection mass fluxes. The Figure (2.3.2.4) case has one-tenth injection mass flux as the other case. The result shows that higher injection velocity causes only slightly more agglomeration. Higher velocity means high mass flux so that more particles (collection centers) are injected.

Figures (2.3.2.1) and (2.3.2.5) have the same injection particle size (2μm) and mass flux, but have different injected particle number densities, $16x10^{+12}$/m^3 and $1.6x10^{+12}$/m^3, respectively. The injection velocity is also different, being V = 1.0 m/s and V = 10.0 m/s, respectively. The result indicates that higher number density plays a more significant role than larger injection velocity on particle agglomeration. This can be understood since more injected particles provide more collection centers.

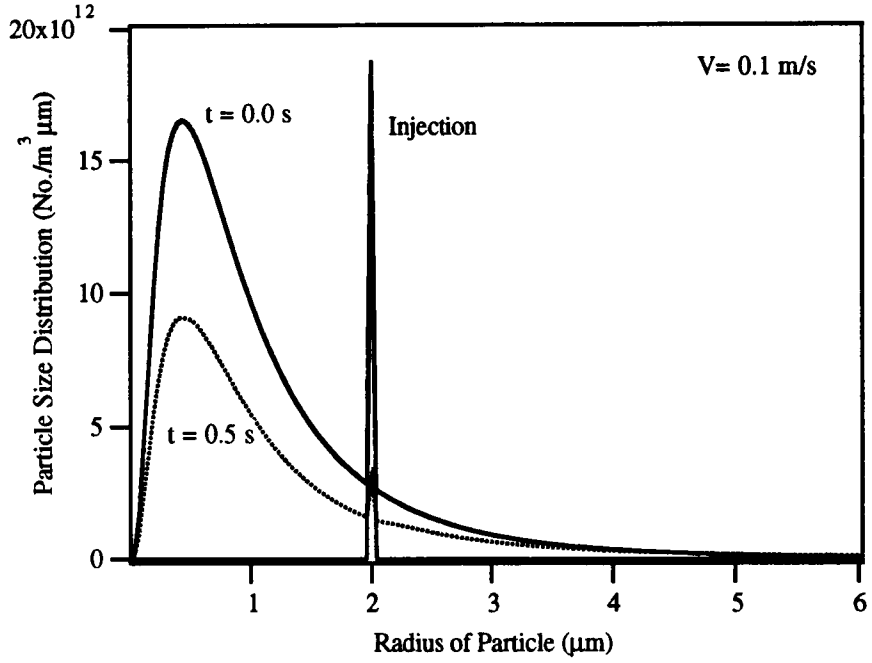


Figure 2.3.2.4 Injection at $r = 2$ µm and $V = 0.1$ m/s

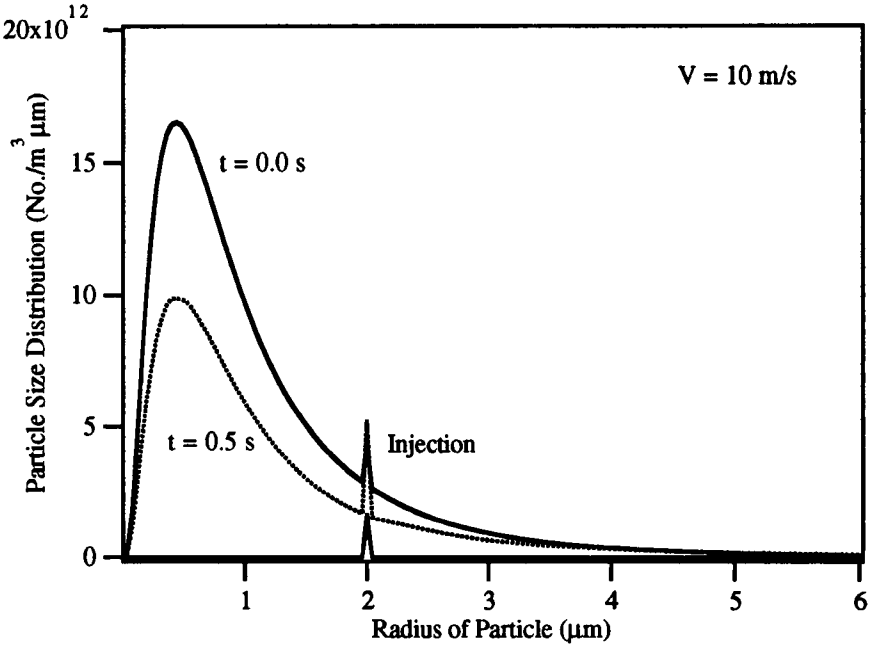


Figure 2.3.2.5 Injection at $r = 2$ µm and $V = 10.0$ m/s

Figures (2.3.2.1) and (2.3.2.6) have the same injection particle size (2μm) and injection velocity (V = 1.0 m/s), but have different particle number density, $16x10^{+12}/m^3$ and $4.0x10^{+12}/m^3$, respectively. The result indicates more explicitly that a higher number injected particle density causes more particle agglomeration.

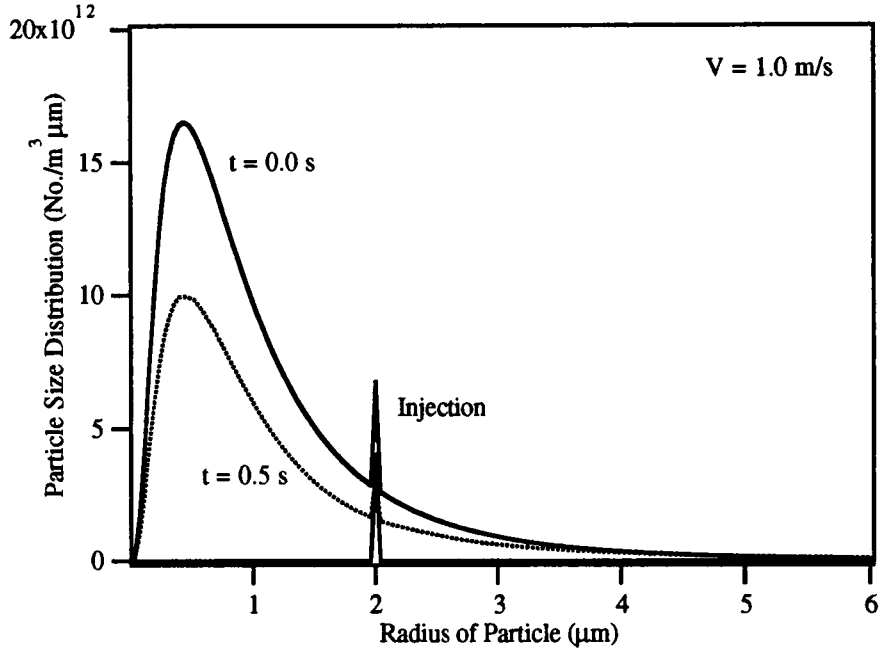


Figure 2.3.2.6 Injection at r = 2 μm and V = 1.0 m/s

It can be concluded that a higher number density of injection particles has more effect on fine particle agglomeration than injection velocity. Optimal agglomeration results are obtained with less injection mass loading but greater injection number densities by injecting smaller particles. To meet these requirements, appropriately small injection particle sizes at a high number density are needed. A good size is about 2.0μm, which gives a high collection efficiency and a low injection mass loading with high particle number density for a reasonable injection velocity. For different initial particle distributions, sizes of injected particles will be different in order to obtain optimal agglomeration.

For a better view of the differences between distributions in these figures, table 2 gives the particle concentrations at the peak of the PSD, 1.0μm, and 3.0μm.

Table 2 Predicted Particle Concentration (No./m^3-μm) at t=0.5s

Figure	Peak (0.44μm)	at 1.0μm	at 3.0μm
2.3.1	$1.02\text{x}10^{13}$	$6.15\text{x}10^{12}$	$5.94\text{x}10^{11}$
2.3.2.1	$8.80\text{x}10^{12}$	$5.34\text{x}10^{12}$	$6.97\text{x}10^{11}$
2.3.2.2	$1.01\text{x}10^{13}$	$6.07\text{x}10^{12}$	$5.89\text{x}10^{11}$
2.3.2.3	$1.03\text{x}10^{13}$	$6.14\text{x}10^{12}$	$5.93\text{x}10^{11}$
2.3.2.4	$9.08\text{x}10^{12}$	$5.49\text{x}10^{12}$	$6.52\text{x}10^{11}$
2.3.2.5	$9.88\text{x}10^{12}$	$5.94\text{x}10^{12}$	$6.52\text{x}10^{11}$
2.3.2.6	$9.95\text{x}10^{12}$	$5.97\text{x}10^{12}$	$6.22\text{x}10^{11}$

On the other hand, if the injected particles have a given distribution function $n_s(r)$, Q_t and mass loading can be expressed in Eq.(2.3.2.3) and Eq.(2.3.2.2), respectively, when solving Eq.(2.3.2.1). Since the injection particles are ash collected at the CFFF BH and DESP, it is assumed that the injection particles have a log-normal distribution:

$$n_s(r) = \frac{n_0}{\sqrt{2\pi}\sigma r} e^{-\frac{(\ln r + a)^2}{2\sigma^2}} \quad . \tag{2.3.2.9}$$

There are three parameters, n_0, σ, a, to be selected to fit the desired injection particle distribution. Figures (2.3.2.7), (2.3.2.8), and (2.3.2.9) have the same injection velocities and injection distributions except for their particle magnitudes n_0. They show that a higher particle count increases agglomeration. The higher particle magnitude means more particles and a higher injection mass flux.

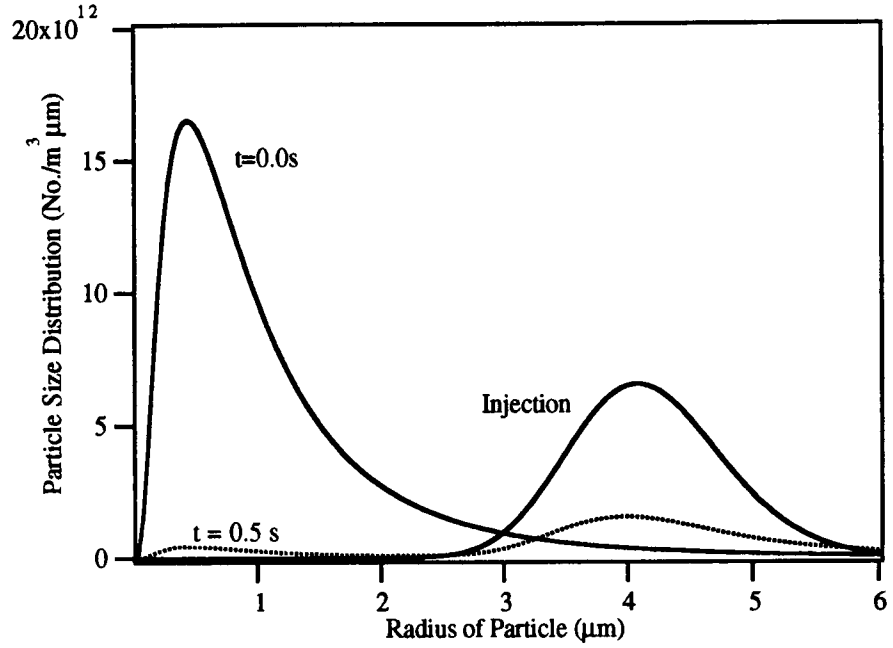


Figure 2.3.2.7 Injection of n_0=1.0x10^{+13}/m^3, σ=0.15, a =12.39, V=1.0 m/s

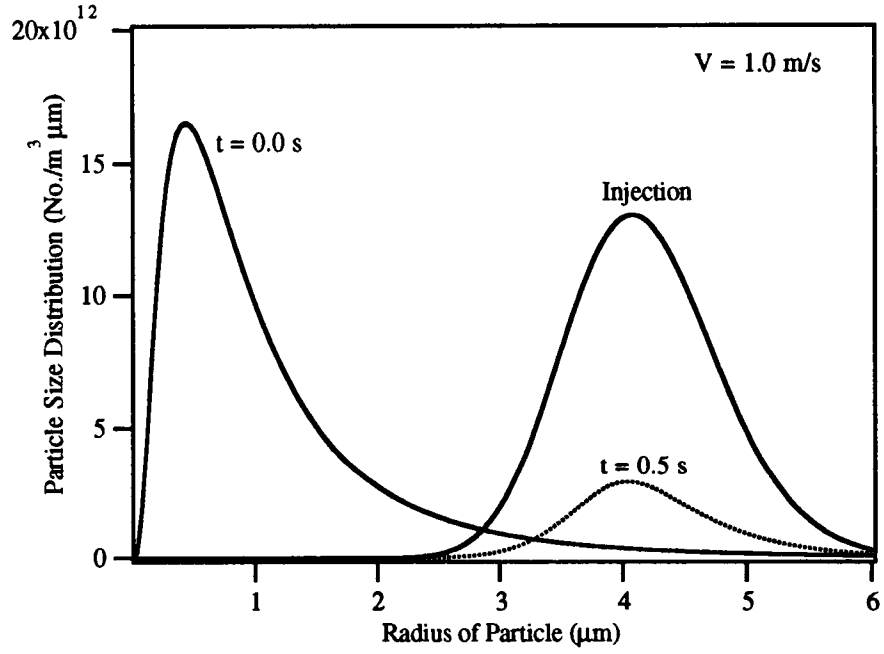


Figure 2.3.2.8 Injection of n_0=2.0x10^{+13}/m^3, σ=0.15, a=12.39, V=1.0 m/s

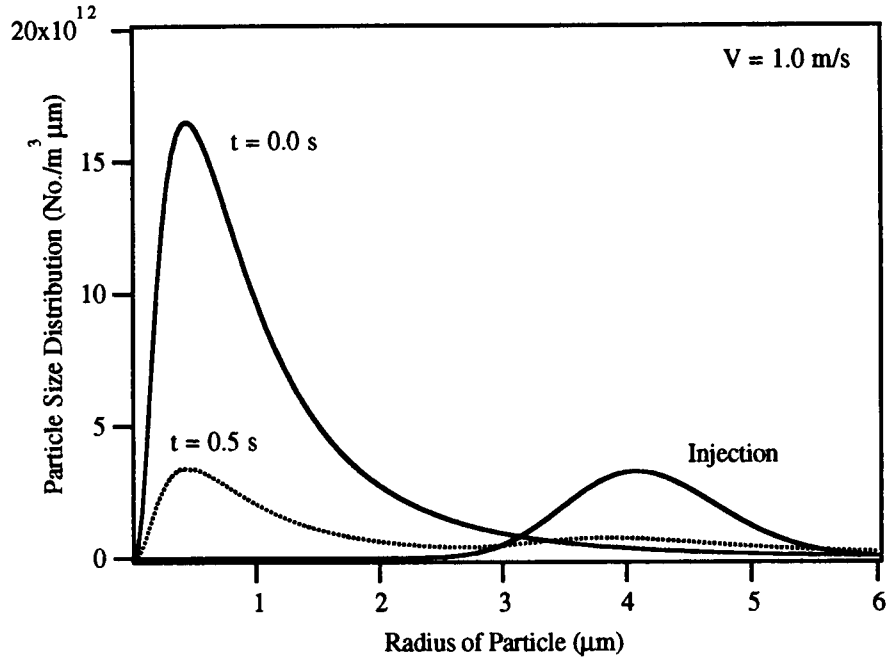


Figure 2.3.2.9 Injection of $n_0 = 0.5 \times 10^{+13}/m^3$, $\sigma = 0.15$, $a = 12.39$, $V = 1.0$ m/s

Figures (2.3.2.7) and (2.3.2.10) have the same injection distribution, but different injection velocities, $V = 1.0$m/s and $V = 0.1$m/s, respectively. A higher injection velocity improve agglomeration. Higher injection velocity also means more injected particles and higher injected mass flux.

Figures (2.3.2.7) and (2.3.2.11) have the same injection distribution, but different location of the peak of the distribution of the injected particles. The mass flux in the latter case is one-tenth the first case mass flux and less agglomeration than the first case.

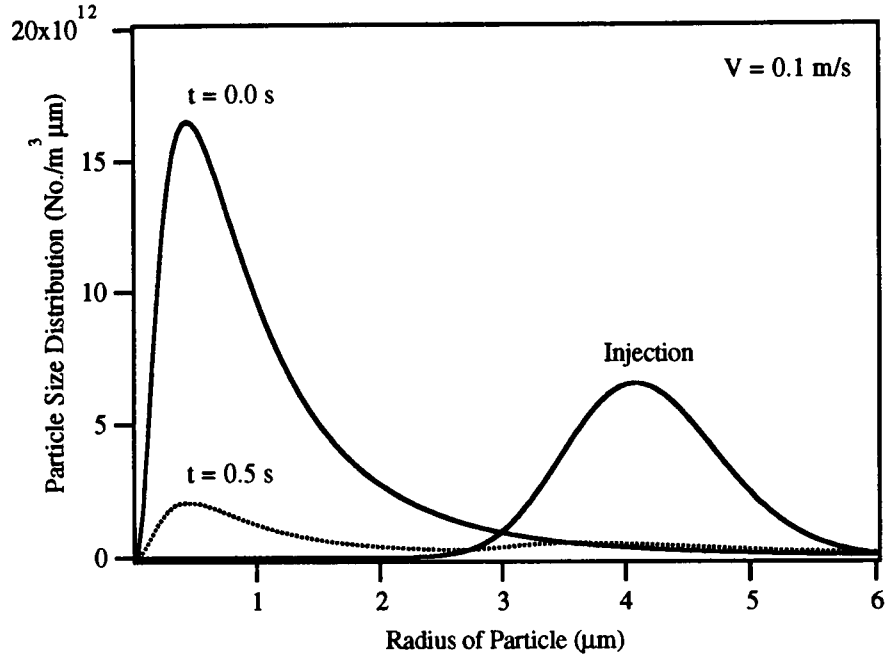


Figure 2.3.2.10 Injection of n_0=1.0x10^{+13}/m^3, σ=0.15, a=12.39, V=0.1m/s

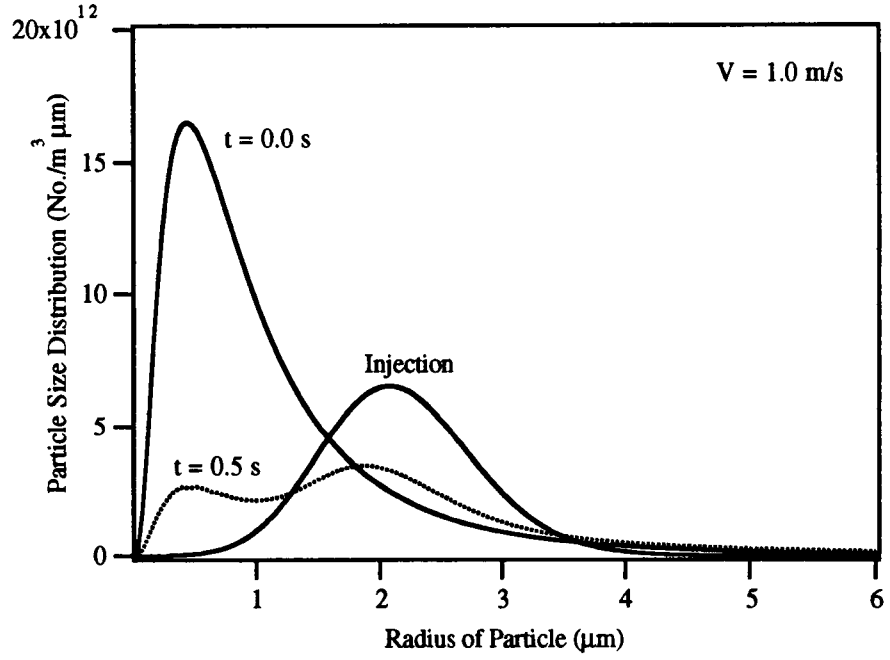


Figure 2.3.2.11 Injection of n_0=1.0x10^{+13}/m^3, σ=0.29, a=13.04, V=1.0 m/s

Figures (2.3.2.11), (2.3.2.12), and (2.3.2.13) also have the same injection velocities and injection distributions except for their particle magnitudes n_0. They verify that a higher particle magnitude increases agglomeration. Comparing Figures (2.3.2.7-9) to Figures (2.3.2.11-13), the latter figure set has less mass flux than the first figure set, Figures (2.3.2.7-9). Although the three cases of Figures (2.3.2.7-9) induce stronger agglomeration, the three cases of Figures (2.3.2.11-13) are more practical since it is not acceptable to inject excessive number of particles in practical applications.

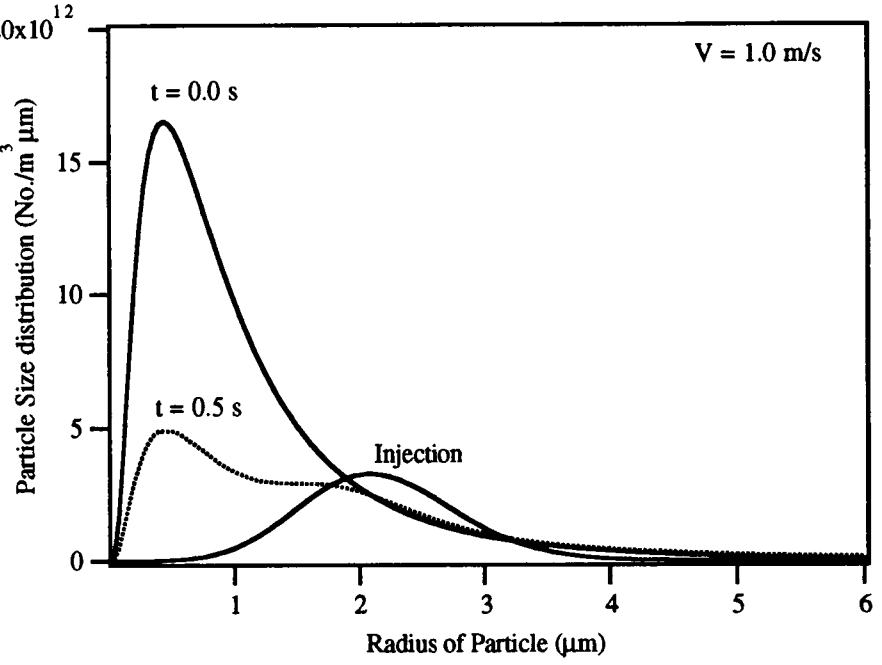


Figure 2.3.2.12 Injection of n_0=0.5x10^{+13}/m^3, σ=0.29, a=13.04, V=1.0 m/s

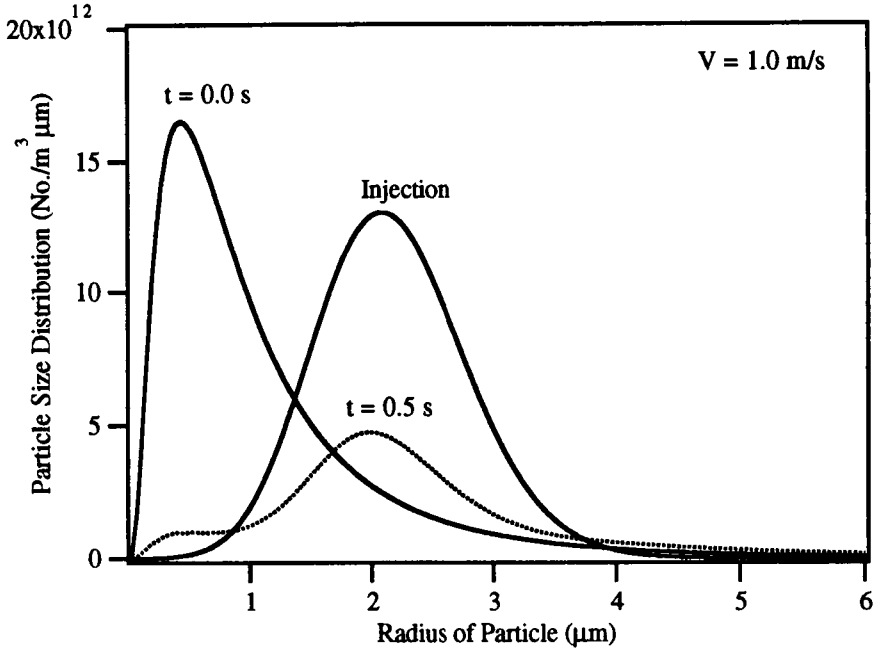


Figure 2.3.2.13 Injection of n_0 =1.0x10^{+13}/m^3, σ=0.29, a=13.04, V=1.0 m/s

When the injected particles have significant number of smaller sizes (i.e.,< 0.5μm) in their distributions, like Figures (2.3.2.14) and (2.3.2.15), they will introduce a comparable number of small particles as in the original flow and that causes a relatively high concentration of small particles. But a low concentration of small particles in the injected flow will be a great help in reducing the number of small particles in the original flow.

It also can be concluded that a higher number density of injection particles has more of an effect on particle agglomeration than injection velocity. Optimal agglomeration results for particle injection requires minimizing injection mass loading while achieving particle agglomeration. To meet these requirements, one can select appropriate mean injection particle sizes (i.e.,1.0μm - 2.0 μm) and minimizing the small particles injected (< 0.5μm).

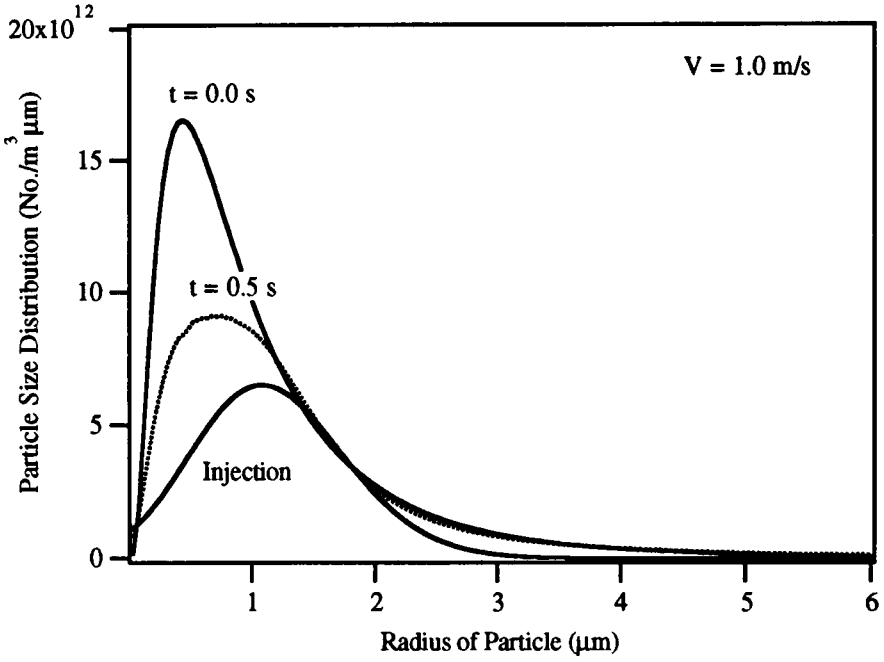


Figure 2.3.2.14 Injection of n_0=1.0x10^{+13}/m^3, σ=0.55, a=13.61, V=1.0 m/s

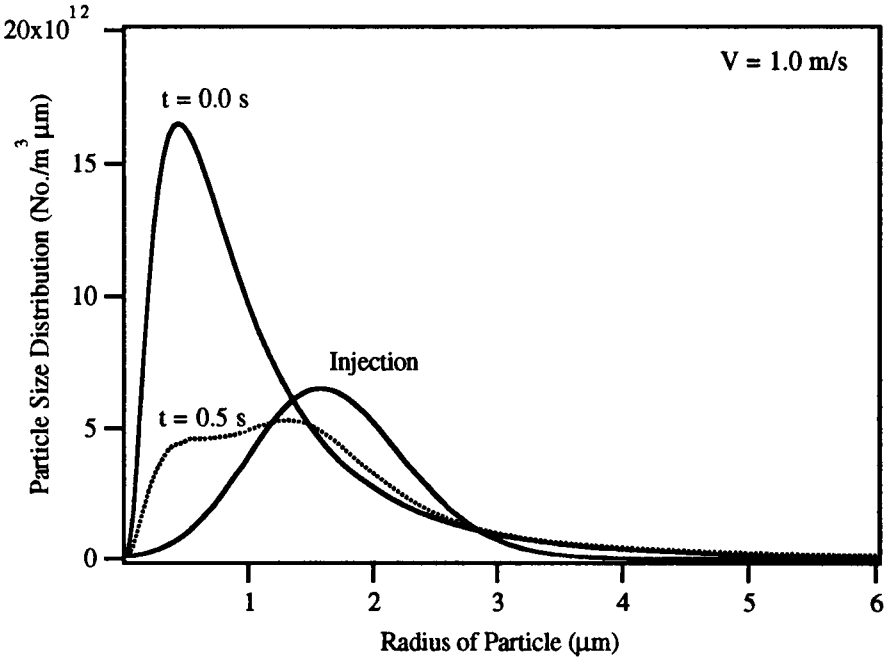


Figure 2.3.2.15 Injection of n_0 =1.0x10^{+13}/m^3, σ=0.38, a=13.29, V=1.0 m/s

Also for a better view of the differences between these Figures (2.3.2.7-2.3.2.15), table 3 gives the particle concentration at different particle radii.

Table 3 Predicted Particle Concentration (No./m^3-μm) at t = 0.5s

Figure	Peak	at 1.0μm	at 3.0μm
2.3.1	$1.02x10^{13}$ (0.44μm)	$6.15x10^{12}$	$5.94x10^{11}$
2.3.2.7	$4.37x10^{11}$ (0.44μm)	$2.11x10^{11}$	$3.44x10^{11}$
2.3.2.8	$3.84x10^{9}$ (0.40μm)	$2.44x10^{9}$	$2.31x10^{9}$
2.3.2.9	$2.37x10^{12}$ (0.40μm)	$2.04x10^{12}$	$4.61x10^{11}$
2.3.2.10	$2.03x10^{12}$ (0.40μm)	$1.23x10^{12}$	$3.74x10^{11}$
2.3.2.11	$2.66x10^{12}$ (0.52μm)	$2.14x10^{12}$	$1.37x10^{12}$
2.3.2.12	$4.90x10^{12}$ (0.44μm)	$3.36x10^{12}$	$1.03x10^{12}$
2.3.2.13	$1.01x10^{12}$ (0.52μm)	$1.23x10^{12}$	$1.66x10^{12}$
2.3.2.14	$9.13x10^{12}$ (0.68μm)	$8.57x10^{12}$	$8.21x10^{11}$
2.3.2.15	$4.60x10^{12}$ (0.56μm)	$4.94x10^{12}$	$9.85x10^{11}$

At the CFFF, particles to be injected were collected at the BH and DESP. The size distribution of these collected particles was measured by Insitec as they were injected. This distribution was not optimized as is discussed in Chapter 3.

2.3.3 Coagulation Equation with Condensation

At the outlet of the secondary combustor, the gas temperature is about 1600 K. Flow has particles in solid, liquid and gas phases. One of important chemical compounds, K_2SO_4, has vapor phase and is in the supersaturated state. This vapor K_2SO_4 is condensing to form very small particles as the gas temperature decreases. Very small solid ash is also known to be in the flow, and some of the condensed K_2SO_4 has solidified.

2.3.3.1 Rate of Solid Particle Growth

Particle growth rate relation are derived in Appendix E. The expression for growth rate is,

$$\dot{r} = \frac{12}{5}\frac{p_{sat}(T_g)}{\rho\sqrt{2\pi R_v T_g}} K_n f\left(S - \frac{p_{sat}(T_s)}{p_{sat}(T_g)}\left(\frac{T_g}{T_s}\right)^{\frac{1}{2}} e^{\frac{\phi}{kT_s}} \right) \tag{E.25}$$

and

$$T_s = T_g\left\{ 1 + \frac{fL_c p_{sat}(T_g)(S - e^{\frac{\phi}{kT_s}})}{\frac{25}{8} pgT_g\sqrt{R_v R_g} + fL_c p_{sat}(T_g)\left(\frac{L_c}{R_v T_g} - \frac{\phi}{kT_g} - \frac{1}{2}\right)e^{\frac{\phi}{kT_s}}} \right\} \tag{E.26}$$

with

$$f = \frac{K_n + 1}{1 + \frac{12}{5\alpha_c}(K_n + 1)} \tag{E.27}$$

$$g = \frac{K_n + 1}{1 + 15\left(\frac{3\gamma - 1}{\gamma - 1}\right)(K_n + 1)}. \tag{E.28}$$

The saturated pressure of K_2SO_4 is given by Eliezer et. al.[37] and Gurvich et. al.[38] If only particle growth is considered, the particle size distribution is governed by

$$\frac{\partial n_k(r,t)}{\partial t} + \frac{\partial}{\partial r}\left(\dot{r} n_k(r,t)\right) = 0, \quad k = 1,2..... \tag{2.3.3.1}$$

It is a typical Euler equation. If the rate of the condensation growth is constant, $\dot{r} = c$, the solution to Eq.(2.3.3.1) is

$$n_k = n_k(r - ct, t) \tag{2.3.3.2}$$

At different locations, however, the rate of the condensation growth will vary since the temperatures and supersaturation ratio are different. The particle size distribution can be

obtained by numerical methods. Applying a first-order upwind scheme[39] to Eq.(2.3.3.1), one can generate the results presented in Figure (2.3.3.1).

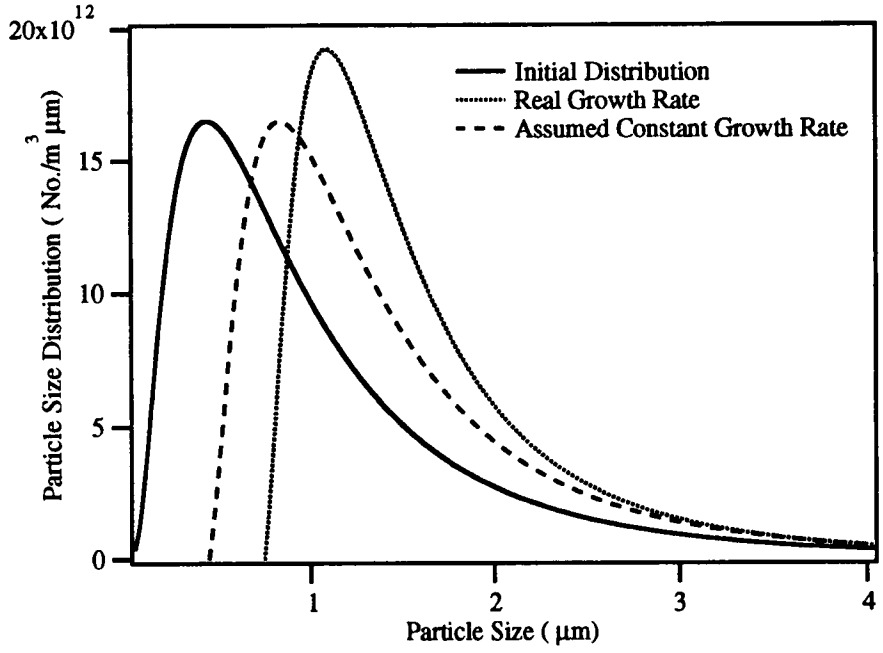


Figure 2.3.3.1 Condensation Growth at the CFFF

From this plot, it can be seen that there are cut-off radii. For a smaller growth rate, the cut-off radius is smaller, for example, r = 0.5μm for the growth rate of 0.5μm/s with an elapsed time of approximately 1.0 second. However, a cut-off radius was not observed from experimental measurements since there are other processes besides the condensation, such as nucleation, which continues to produce very small particles. Also, as particles grow by condensation, the thermophoretic coagulation also is taking place. The modification to Eq.(2.3.3.1) with thermophoretic coagulation is

$$\frac{\partial n_k(r,t)}{\partial t}+\frac{\partial}{\partial r}\left(\dot{m}_k(r,t)\right)=\frac{1}{2}\sum_{i+j=k} b_{ij}n_i n_j - n_k\sum_{i=1}^{\infty} b_{ik}n_i, \quad k=1,2..... \tag{2.3.3.3}$$

A solution is obtained with a first-order upwind scheme as shown in Figure (2.3.3.2).

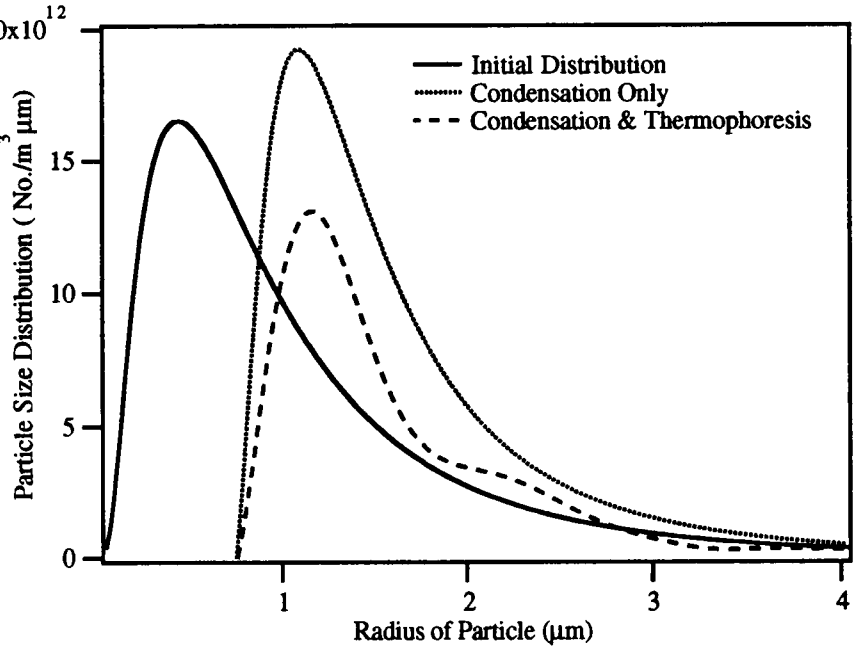


Figure 2.3.3.2 PSD with Condensation Growth and Thermophoretic Coagulation

As shown previously in section (2.3.2), thermophoretic coagulation increases particle sizes and decreases particle number concentration. But, introduction of thermophoresis does not affect the existence of a cut-off radius.

2.3.4 Coagulation Equation with Heterogeneous Nucleation

Particle nucleation is discussed in Appendix F. At the CFFF, since there are a huge number of different particles, heterogeneous nucleation is the primary event. Heterogeneous nucleation rate is given by

$$J(r,t) = \frac{p}{\sqrt{2\pi m_c kT}} 4\pi^2 r^2 r^{*2} n_{ads} n(r,t) \exp(-\frac{\Delta G_c^*}{kT}). \qquad \text{(F.24)}$$

where

$$\Delta G_c^* = \frac{16\pi\sigma_{LG}^3 V_L^2}{3(kT\ln S)^2} f(x,z), \tag{F.19}$$

and

$$f(x,z) = 1 + \left(\frac{1-xz}{\tilde{g}}\right)^3 + x^3\left[2 - 3\frac{z-x}{\tilde{g}} + \left(\frac{z-x}{\tilde{g}}\right)^3\right] + 3xz^2\left(\frac{z-x}{\tilde{g}} - 1\right), \tag{F.21}$$

and the critical size of nucleation is

$$r^* = \frac{2\sigma}{n_l kT\ln S} = \frac{2\sigma V_l}{kT\ln S}. \tag{F.11}$$

Other parameters can be found in Appendix F. If only nucleation is considered, the particle size distribution is governed by

$$\frac{\partial n(r,t)}{\partial t} = -I^0(r,t)n(r,t). \tag{2.3.4.1}$$

If I^0(r, t) is constant, the solution to Eq.(2.3.4.1) is

$$n(t) = n_0 \exp(-I^0 t). \tag{2.3.4.2}$$

Note that particle number density decreases with time in this solution. Smaller particles, however, have smaller nucleation rates (see Appendix F). Thus, for the larger particles, their number densities increase significantly if J is not very small. If J is not dependent on the sizes of nucleating particles, the particle number density is

$$n(t) = n_0 \exp(-\int I^0(t')dt').$$ (2.3.4.3)

Generally, since J is the function of the radius of the particles and time, Eq.(2.3.4.1) can be solved numerically with the first-order upwind scheme. Applying conditions representative of the CFFF, one can plot the solution to Eq.(2.3.4.1) as

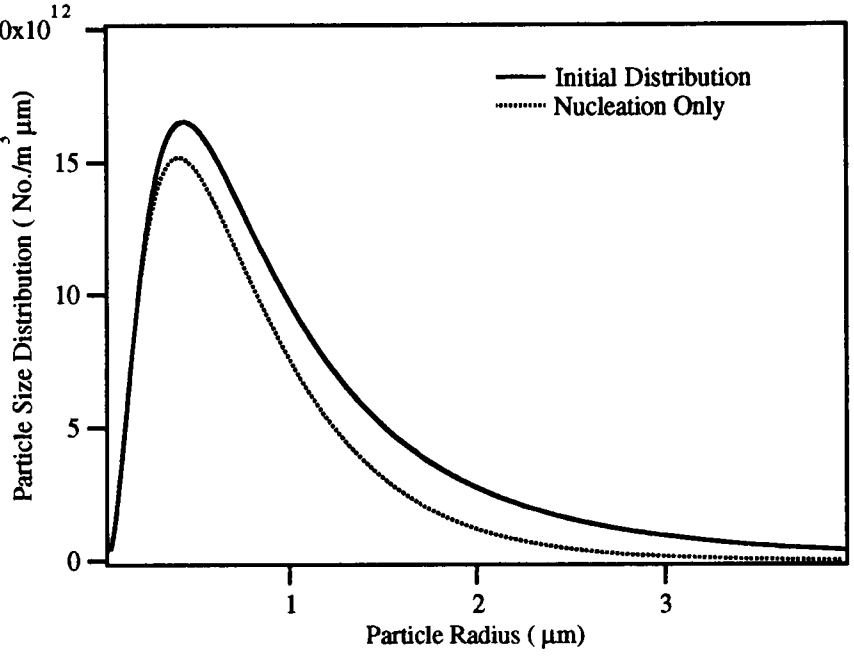


Figure 2.3.4.1 PSD with Heterogeneous Nucleation

If collision of particles by thermophoresis is considered, Eq.(2.3.4.1) can be rewritten as

$$\frac{\partial n_k(r,t)}{\partial t} = \frac{1}{2}\sum_{i+j=k} b_{ij} n_i n_j - n_k \sum_{i=1}^{\infty} b_{ik} n_i - J_k, \quad k = 1,2.....$$ (2.3.4.2)

Again, applying conditions representative of the CFFF and solving equation (2.3.4.2) numerically, provides the solution plotted in Figure (2.3.4.2). With the thermophoretic

coagulation, the particle number magnitude is lower than that without it, especially, at larger particle size(i.e.,>1.0μm).

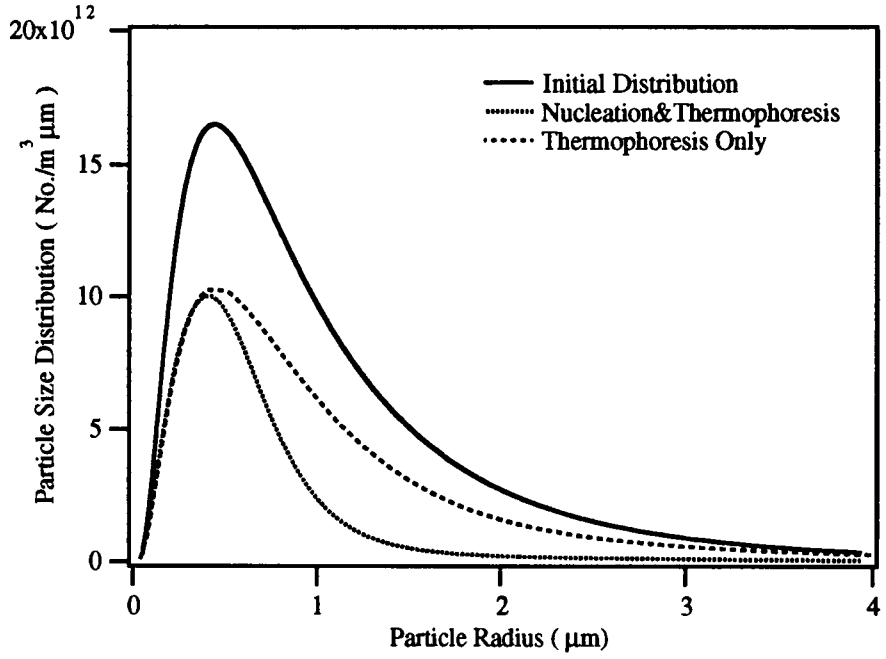


Figure 2.3.4.2 PSD with Nucleation and Thermophoretic Coagulation

2.3.5 Modified Coagulation Equation with Heterogeneous Nucleation, Condensation, and Particle Injection

As mentioned in the section (2.3.3), not only does condensation growth occurred at the CFFF but also heterogeneous nucleation and thermophoretic coagulation will occur. Additionally, after the secondary combustor at the CFFF, particles as nuclei can be injected into the original flow to enhance thermophoretic coagulation. According to previous discussions, those processes will increase particle sizes, increase the number concentration of the larger particles, and reduce the number concentration of the smaller particles. Modification of the coagulation equation with condensation growth, heterogeneous nucleation, and particle injection gives

$$\frac{\partial n_k(r,t)}{\partial t}+\frac{\partial}{\partial r}\left(\dot{r}n_k(r,t)\right)$$
$$=\frac{1}{2}\sum_{i+j=k}b_{ij}n_i n_j-n_k\sum_{i=1}^{\infty}b_{ik}n_i-J_k+Q_k,\quad k=1,2.....\qquad(2.3.5.1)$$

In Eq.(2.3.5.1), $\dot{r}$, b_{ij}, J, and Q are defined in the previous sections. In this section, Q is related to the real distribution of particles injection at the CFFF just after the secondary combustor. This equation requires a numerical solution did the earlier equations in the section (2.3.1). Because a first-order upwind scheme is used to compute the evolution of the particle size distribution in this section instead of Runge-Kutta time integration, modification of Eq.(2.3.5.1) to include the two independent variables *(r,t)* is slightly different. Let

$$N=\sum_{i=1}^{\infty}n_i(r,0)\quad\text{and}\quad\hat{n}_i(r,t)=\frac{n_i(r,t)}{N}.\qquad(2.3.5.2)$$

Eq.(2.3.5.1) then can be rewritten as

$$\frac{\partial \hat{n}_k(r,t)}{\partial t}+\frac{\partial}{\partial r}\left(\dot{r}\hat{n}_k(r,t)\right)$$
$$=\frac{1}{2}N\sum_{i+j=k}b_{ij}\hat{n}_i\hat{n}_j-\hat{n}_kN\sum_{i=1}^{\infty}b_{ik}\hat{n}_i-\frac{J_k}{N}+\frac{\dot{Q}_k}{N},\quad k=1,2.....\qquad(2.3.5.3)$$

A numerical solution to this equation assuming only condensation and nucleation is occurring results in Figure (2.3.5.1). It is clear that the cut-off radius appearing in the condensation section vanishes because condensation together with heterogeneous nucleation results in an amount of small particles which condensation alone removes. This result close to the experimental measurements, where the distribution can be measured (particle larger than 0.3μm).

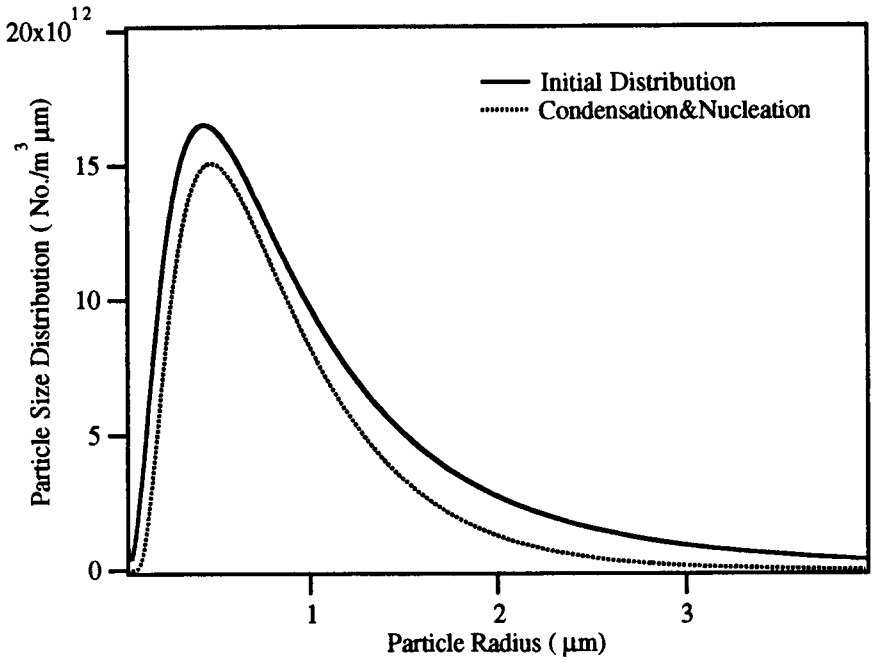


Figure 2.3.5.1 PSD with Condensation and Heterogeneous Nucleation

Figure (2.3.5.2) gives the computed PSD with thermophoresis, condensation, and nucleation. With the thermophoretic coagulation, concentration of particle size is lower than that in the case of combination of the condensation and the nucleation. Again, there is not a cut-off radius. Figure (2.3.5.3) is the computed PSD with condensation, nucleation, thermophoresis and particle injection. Obviously, the competing mechanisms of condensation, nucleation, thermophoresis and agglomeration due to injection particles a signification reduction in the number of submicron particles in the flow.

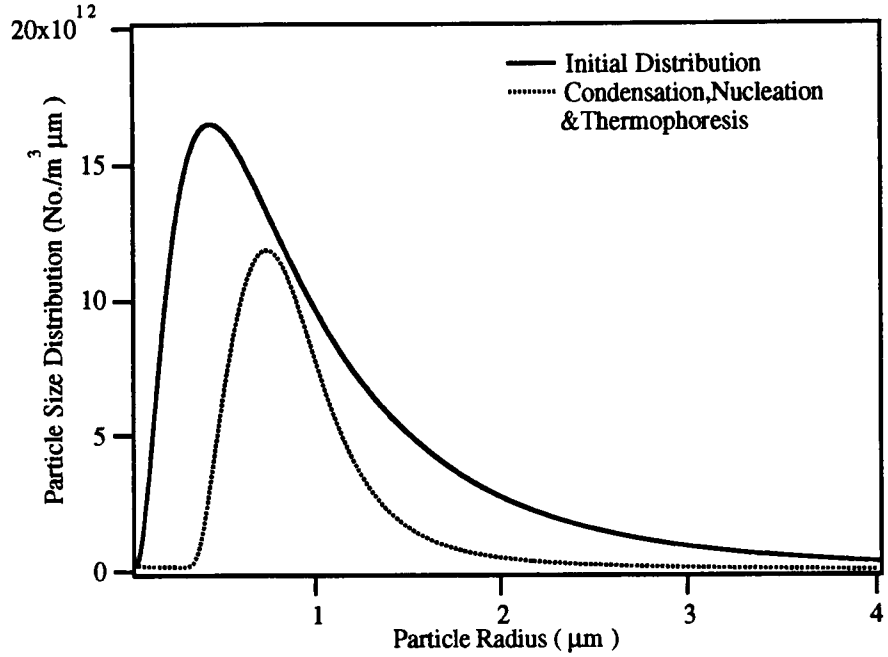


Figure 2.3.5.2 PSD with Condensation, Nucleation &Thermophoresis

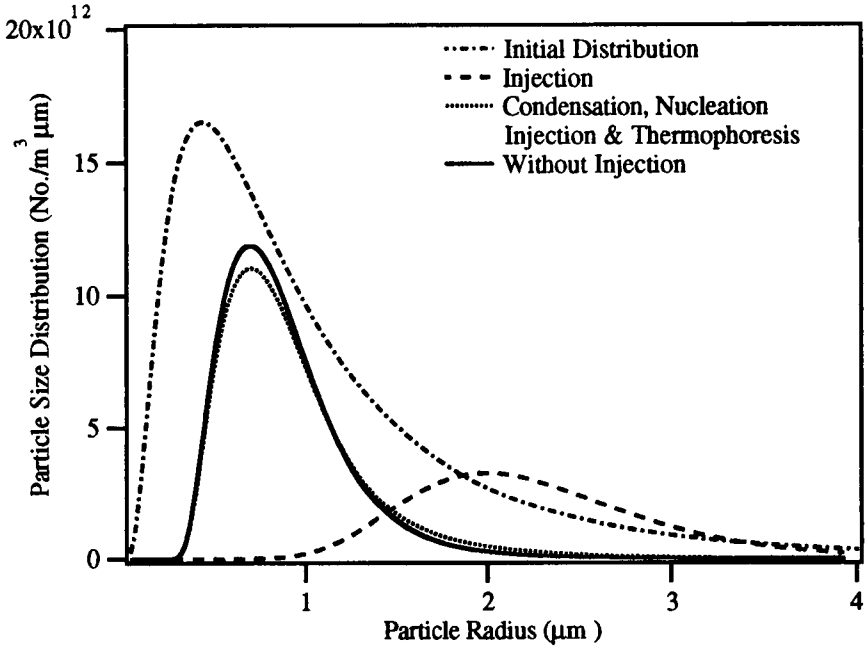


Figure 2.3.5.3 PSD with Condensation, Nucleation, Thermophoresis & Injection

2.4 Particle Agglomeration After Injection

After the particle injection location, which is located between the secondary combustor and CS1, the flow is cooled and becomes a two phase flow containing flyash, mostly solid K_2SO_4 and K_2CO_3 particles and flue gases. After the injection location, there are 14 cooling sections before the BH and the DESP. Thermophoresis self-agglomeration of particles will occur for some of the larger particles that have relatively lower temperatures compared with the smaller particles due to the radiation heat transfer balance between the larger particles and the cooler duct walls. Thermophoresis is primary mechanism of fine particles agglomeration. In these sections, the governing equation of the particle size distribution is the coagulation equation.

$$\frac{dn_k(t)}{dt} = \frac{1}{2}\sum_{i+j=k} b_{ij} n_i n_j - n_k \sum_{i=1}^{\infty} b_{ik} n_i, \quad k = 1,2..... \tag{2.4.1}$$

This equation can be numerically solved with Runge-Kutta time integration as was done in section (2.3.1).

Residence time t for each section has to be calculated to determine time integral. Residence time depends on the flow train mass flux and the length of each section, L. After careful evaluation, t is expressed as

$$t = \frac{pALM_g}{\dot{m}R_g(T_{g2} - T_{g1})} \ln \frac{T_{g2}}{T_{g1}}. \tag{2.4.2}$$

Table 4 gives the residence time and temperatures in each section.

Table 4 Residence Time and Gas Temperature in Each Section

Section	Length(m)	Residence Time (sec.)	Inlet Gas Temp.(K)	Outlet Gas Temp.(K)
TS1	1.78	0.24	1440	1386
CS1	3.10	0.43	1386	1288
CS2	3.10	0.45	1288	1238
TS2	1.78	0.27	1238	1189
CS3	3.10	0.50	1189	1092
CS4	3.10	0.53	1092	1049
TS3	1.78	0.33	1049	984
CS5	3.10	0.60	984	906
CS6	3.10	0.65	906	831
ELB	4.40	0.96	831	855
CS7	3.10	0.72	855	744
CS8	3.10	0.81	744	674
CS9	3.10	0.87	674	622
AH	7.68	2.44	622	540
CS10	3.10	1.14	540	466

CHAPTER 3 EXPERIMENTS

Experiments were performed at the CFFF to evaluate particle injection. The region of interest for the experiments is between the secondary combustor and the inlet of the BH and DESP. Between these two locations is the superheater test module, including a transition section, TS1 (Test Section 1), CS1 (Cooling Section 1), CS2, TS2, CS3, CS4, TS3, CS5, CS6, ELB, CS7, CS8, CS9, and an Air Heater, and CS10. The gas flow temperature range is from 1600 K to 460 K. The flow velocity is approximate 8.0 m/s. The flow is three phase from the secondary combustor to CS1 where the flow temperature is down to 1280 K. After CS1, the flow is two phase gas-solid particle flow. The three-phase flow contains ash particles, gas, and condensed K_2SO_4. At the transition section, the vapor of K_2SO_4 is supersaturated. Particle injection was initiated at the entrance to the transition section. Injected particles are collected at the BH and DESP, and considered as ash particles with a large component of K_2CO_3 and K_2SO_4.

The particle size distribution is the object of measurement diagnostics. Three crews performed this diagnostic with three different methods. The first method is five-stage cyclone. The cyclone can be used at the inlet of the BH and DESP as well as at the secondary combustor but condensation limits it usefulness at the secondary combustor. The second is a laser optical method developed and employed by Insitec, Inc., which was used at the inlet of the BH and ESP and TS1. The third is the SEDS method, which dilutes the flow while preventing condensation and counts number of particles in different range of particle sizes. The SEDS system was used at the inlet of the BH and DESP.

3.1 Particle Size Measurement at the Secondary Combustor and Comparison with Im's Theoretical Prediction

The particle size distribution at the outlet of the secondary combustor has not been studied since the CFFF was built. The only theoretical prediction available was found in Im's paper, which is given in detail in Appendix A. The primary feature of Im's distribution is that the particle size distribution is bimodal due to coal combustion ash and condensation growth and homogeneous nucleation of the slag, which is mostly S_iO_2. Only two experimental measurements were made during the final CFFF tests at the outlet of the secondary combustor by means of a heated 5-stage cyclone. Data were taken on the east side on the east side of the flow train just under the secondary combustor, but this data is subject to condensation is the 5 cyclone stage and sampling lines. A schematic of the flow train at this location is provided in Figure (3.1.1).

Measured result is plotted in Appendix A with two empirical formulas. These two formulas were used for the initial particle size distribution.

3.2 Particle Size Measurements at TS1 and the BH and ESP Inlet

Particle size measurements at TS1 were performed by Insitec, Inc. using their optical size distribution probe during the test LMF5I. Three sets of data were taken with the Insitec optical probe inside the wall of the flow duct 10 inches, 6.25 inches and 5.25 inches. These three penetrations were near the wall since the center line of the flow duct is about 2 feet from the wall. Because the flow temperature at TS1 is fairly high (1440K), the Insitec's probe went 10 inches at most inside the wall during the LMF5I test in order to

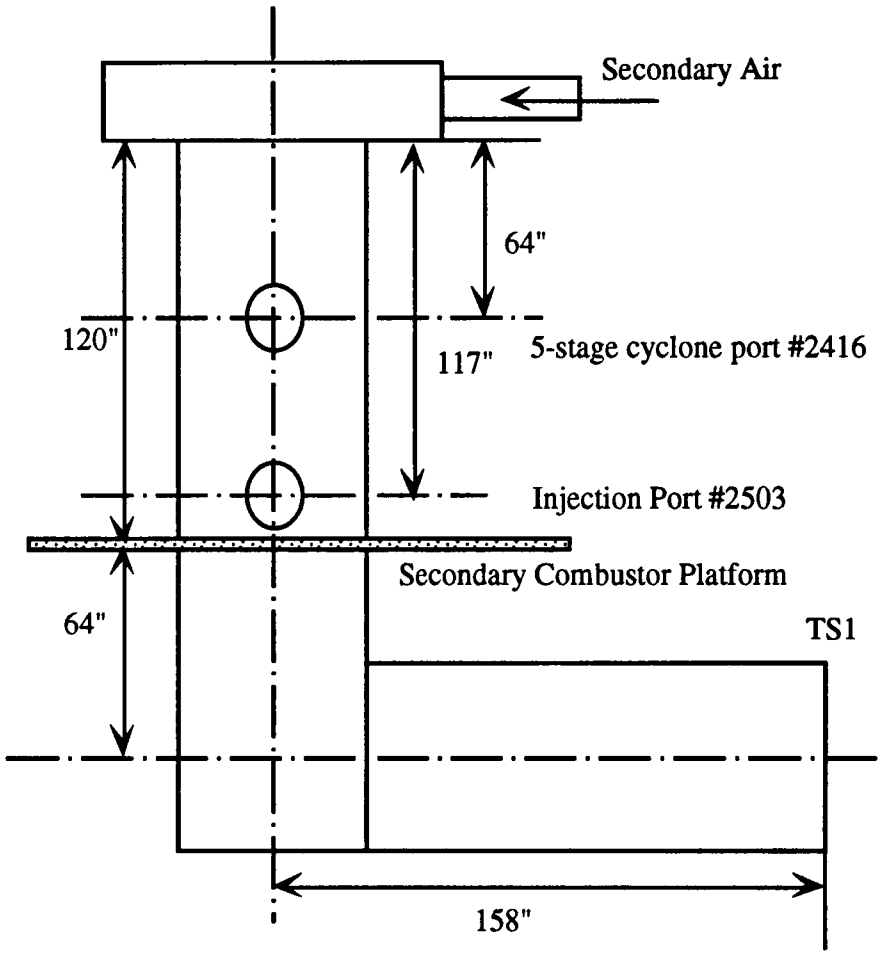


Figure 3.1.1 Locations of Injection Port and Measurement Port

avoid being overheating. Since the probe was close to the wall, the data might not reflect the real particle size concentration at the center line of the flow due to wall effects. Figure (3.2.1), however, is plotted as a reference. Unfortunately, because of many different reasons, scheduled measurements of particle size distribution at the center line of the flow at TS1 with Insitec has not been carried out during the last test. Therefore, these three sets of data are the only data available.

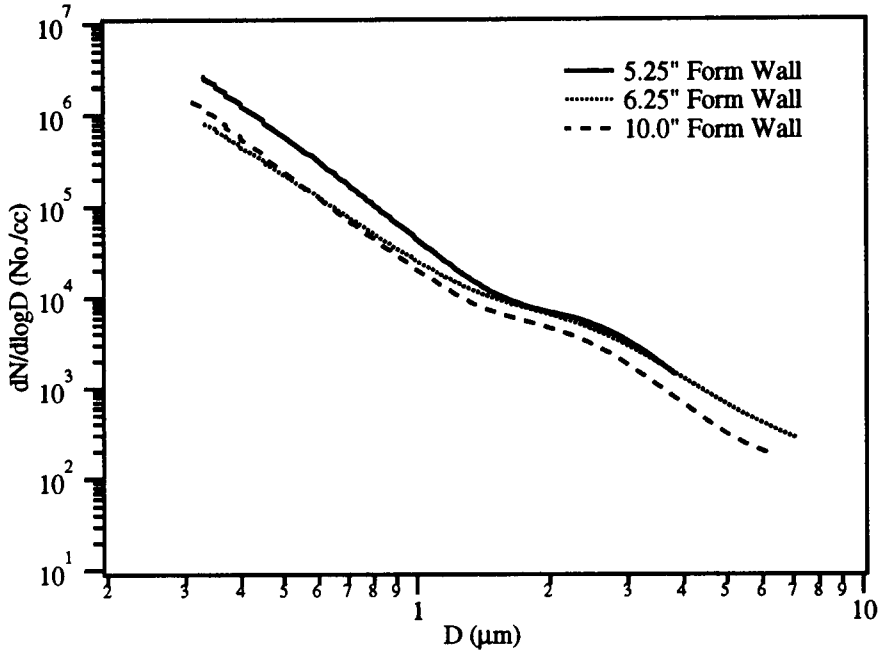


Figure 3.2.1 Particle Size Measurements at TS1 by Insitec, Inc.

Particle size measurement at the inlet of the BH and ESP has been performed by three different methods: 1) the five-stage cyclone method, 2) Insitec's probe, and 3) the SEDS. From Figure (3.2.2), it is clear that these methods show the distribution is bimodal, but the different methods show some magnitude differences. The five-stage cyclone method gives the highest magnitude of the distribution and measures to the smallest particle sizes, but poorest resolution. The Insitec's method gives a lower magnitude because it can only measure down to about 0.7μm in this heavy loading. The SEDS was not operating

properly. The five-stage cyclone has provided consistent data in the past several tests and so has Insitec's probe and their agreement is reasonable for similar test conditions. Insitec's probe gives near real-time distribution data so it can examine instantaneous changes of the particle size distribution, which is important to determine differences with and without particle injection. However, its limitation on measuring small particle sizes makes submicron particle agglomeration unidentifiable.

The 5-stage cyclone was used at the entrance to the BH and ESP and was tried at the outlet of the secondary combustor, but experienced significant internal condensation there. The Insitec's probe was used at TS1 and also at the inlet of the BH and DESP.

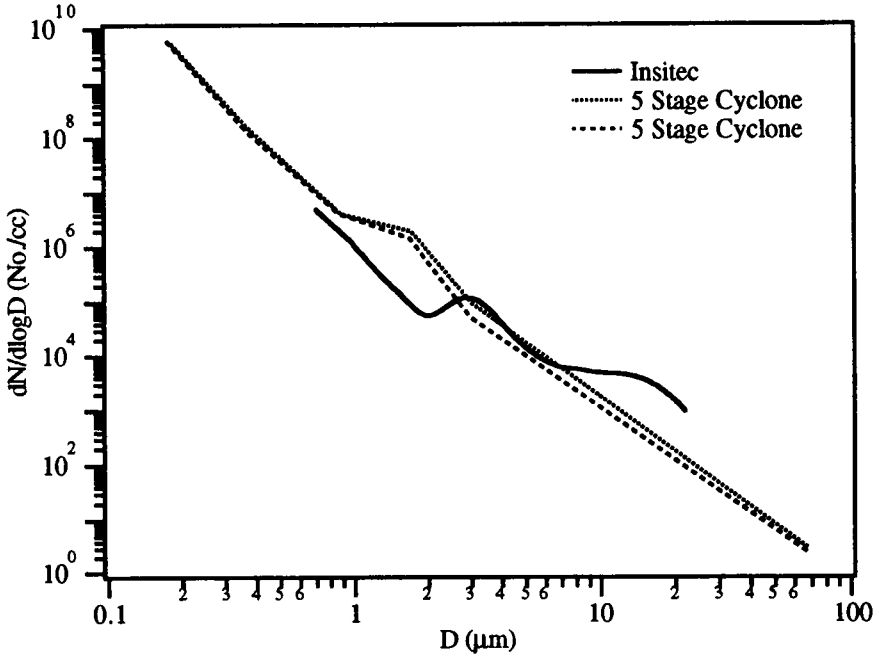


Figure 3.2.2 PSD at the Inlet of the BH and ESP During LMF5I Test

3.3 Theoretical Calculation without Particle Injection

Before comparing experimental results to theoretical predictions, several theoretical calculations are plotted to see how thermophoresis, condensation, heterogeneous nucleation, and particle injection affect the particle size distribution with a real initial particle size distribution, which is given in Appendix A. There are significant differences from a standard log-normal distribution.

From Appendix G, it can be seen that turbulent and gravitational coagulation can be ignored to the modified coagulation equation. Also, wall effects to the coagulation can be neglected from the discussion of Appendix H.

Figure (3.3.1) gives the initial PSD and predicted PSD at outlet of the CS1, and predicted changes of the particle loading from the secondary combustor to CS1 with thermophoretic coagulation only. Because of the initial bimodal distribution, coagulation causes an increase in the distribution at both of the large particle size end and the very small size end, which causes an overall higher number density than that of the initial PSD. Because formation and destruction of a certain size particle involve entire spectrum of particle size, the bimodal distribution will be averaged, which can be seen in Figure (3.3.1).

Figure (3.3.2) is the initial PSD and predicted PSD at outlet of the CS1, and predicted changes of the particle loading from the secondary combustor to CS1 with nucleation only. Condensation shifts the first peak of the bimodal distribution toward larger sizes.

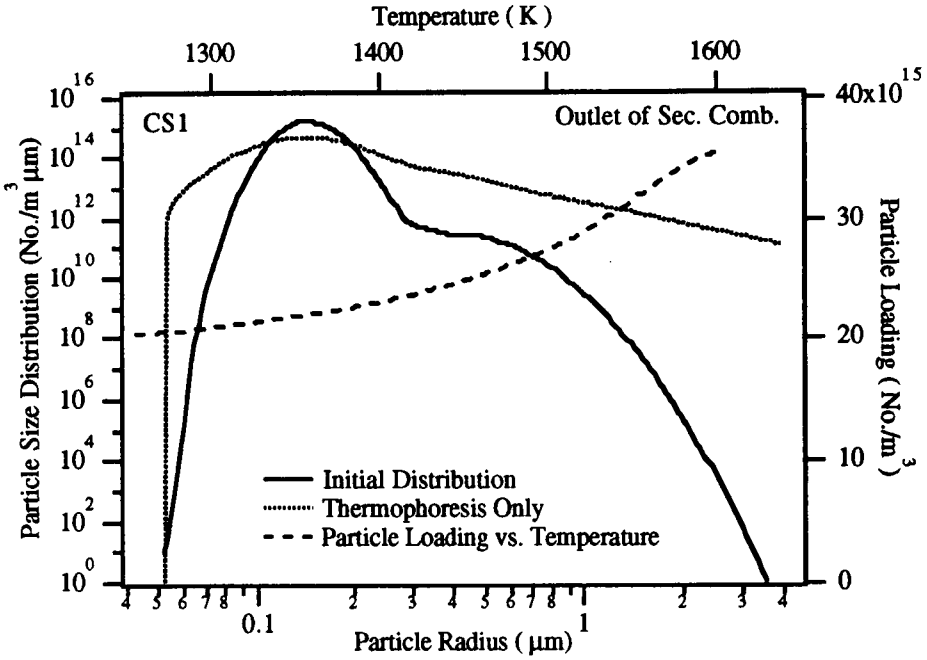


Figure 3.3.1 PSD with Thermophoretic Coagulation

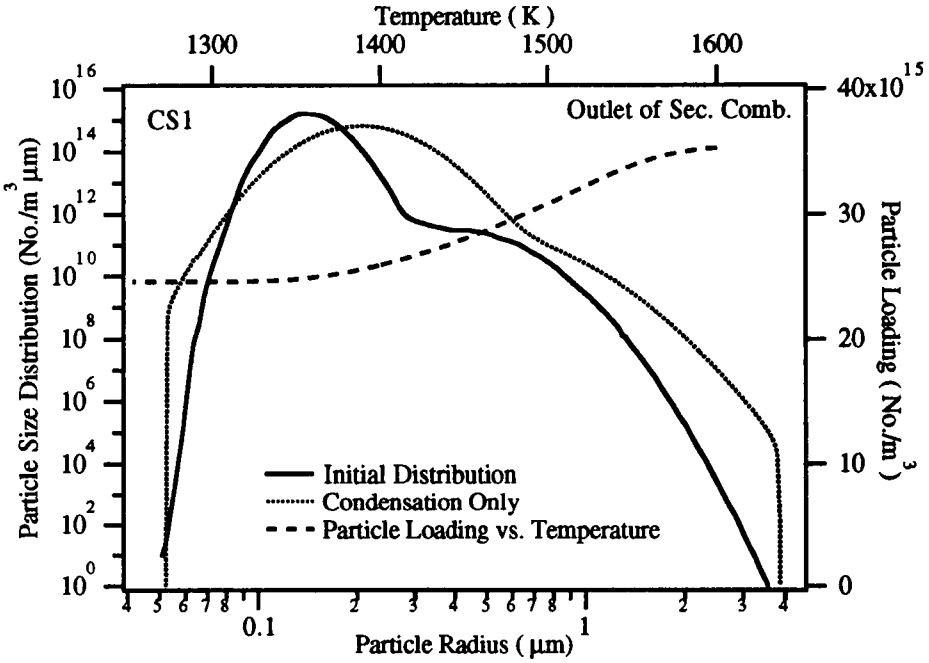


Figure 3.3.2 PSD with Condensation

Figure (3.3.3) is the initial PSD and predicted PSD at outlet of the CS1, and predicted changes of the particle loading from the secondary combustor to CS1 with heterogeneous nucleation only. Because of a higher nucleation rate for large particles even with low concentrations, concentrations of larger size particles are reduced more by nucleation.

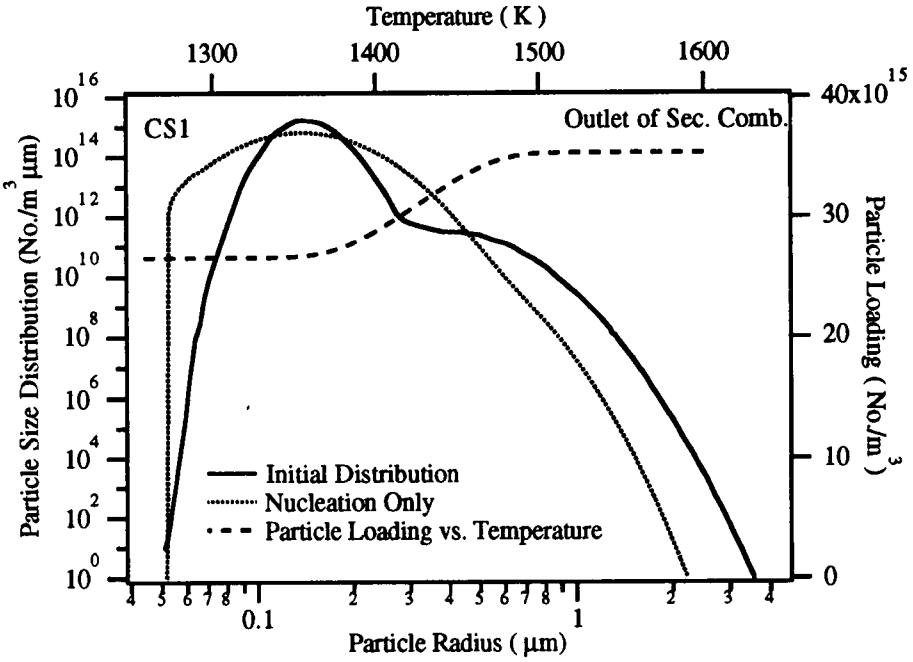


Figure 3.3.3 PSD with Heterogeneous Nucleation

Figure (3.3.4) is the initial PSD and predicted PSD at outlet of the CS1, and predicted changes of the particle loading from the secondary combustor to CS1 with condensation and nucleation. Figure (3.3.5) is the initial PSD and predicted PSD at outlet of the CS1, and predicted changes of the particle loading from the secondary combustor to CS1 with condensation growth and thermophoretic coagulation.

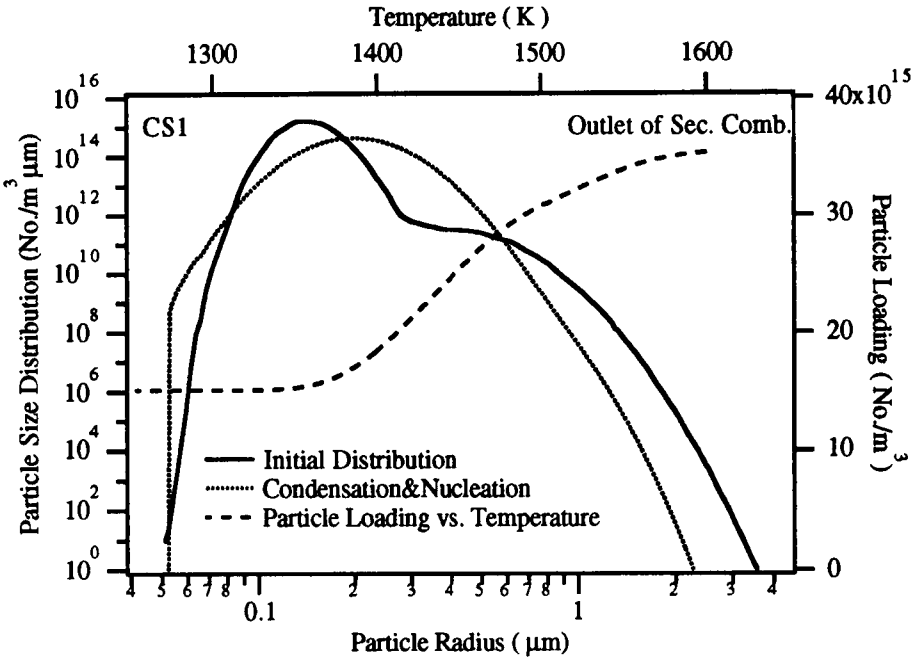


Figure 3.3.4 PSD with Nucleation and Condensation

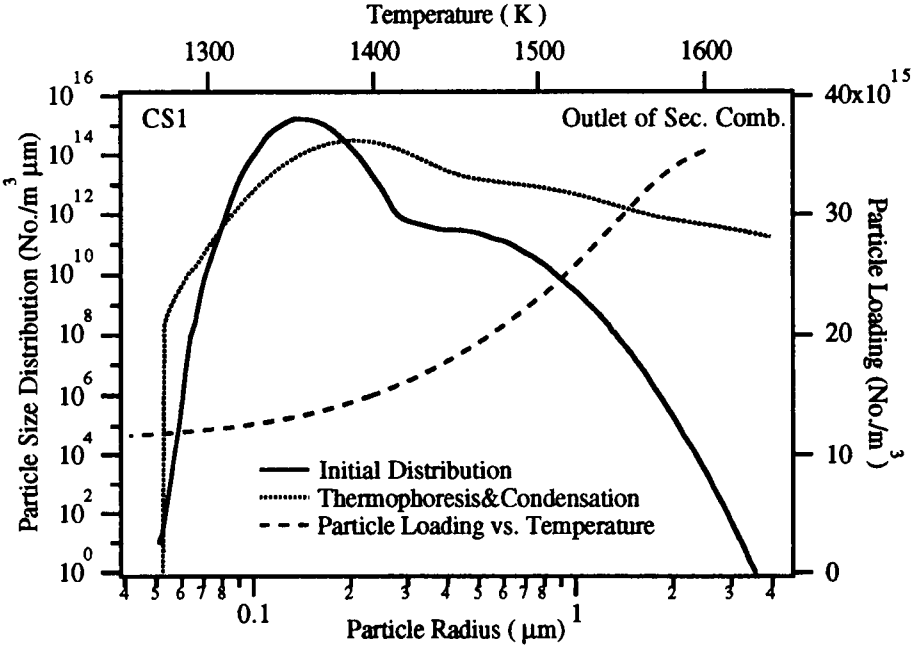


Figure 3.3.5 PSD with Thermophoresis and Condensation

Figure (3.3.6) is the initial PSD and predicted PSD at outlet of the CS1, and predicted changes of the particle loading from the secondary combustor to CS1 with heterogeneous nucleation and thermophoretic coagulation.

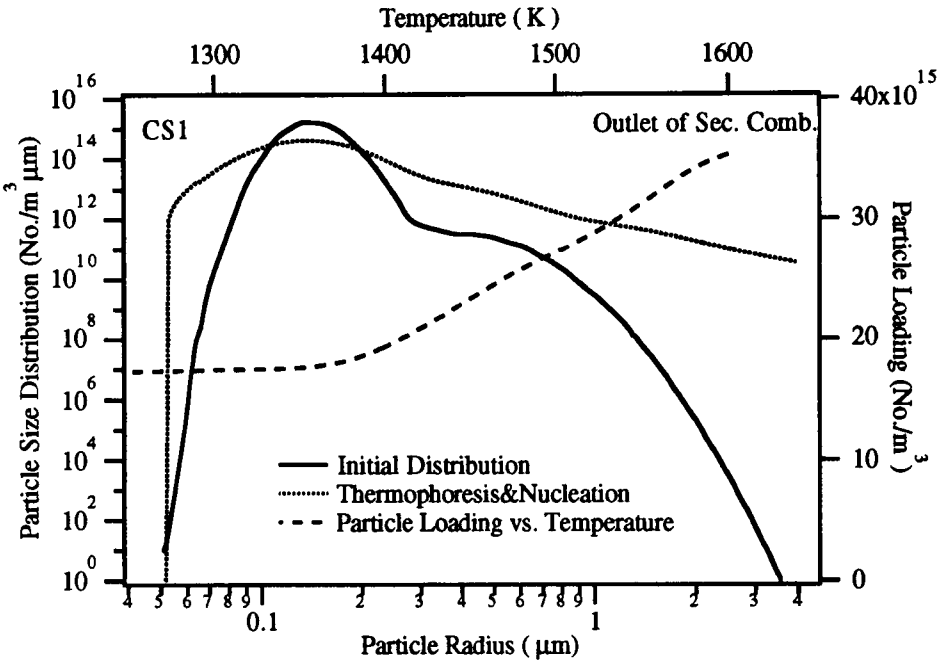


Figure 3.3.6 PSD with Thermophoresis and Nucleation

From these six figures (3.3.1-3.3.6), it can be seen that with the bimodal initial distribution, three phenomena by themselves will keep this bimodal distribution with respect to time and will decrease particle loading, but raise particle concentration at both small and large size end of the distribution. Thermophoretic coagulation has the largest particle number reduction while heterogeneous nucleation gives the least.

3.3.1 Evolution of Particle Size Distribution from the Secondary Combustor to CS1

Between the secondary combustor and the CS1, the flow at CFFF is three-phase. Condensation, heterogeneous nucleation and thermophoresis take place. These three

phenomenon are taken account in the modified coagulation equation. The PSD at CS1 is plotted in Figure (3.3.7).

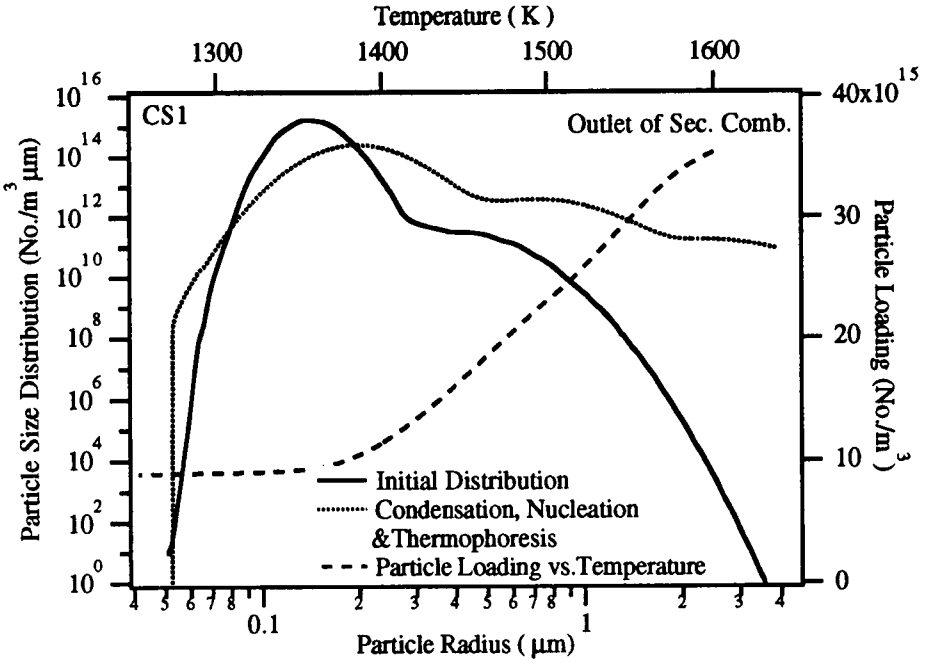


Figure 3.3.7 Predicted PSD at CS1 without Particle Injection

With these three phenomena together, the particle loading is reduced approximate 60% and the peak concentration is 40% lower.

3.3.2 Evolution of Particle Size Distribution from TS1 to the Inlet of the BH

After the CS1 section, the flow is considered as gas-solid particle flow. Only thermophoretic coagulation can exist. The result of the PSD at CS1 in section (3.3.1) is the initial size distribution at this section. Thermophoretic coagulation continues to reduce total particle number and increase particle sizes, as shown in Figure (3.3.8).

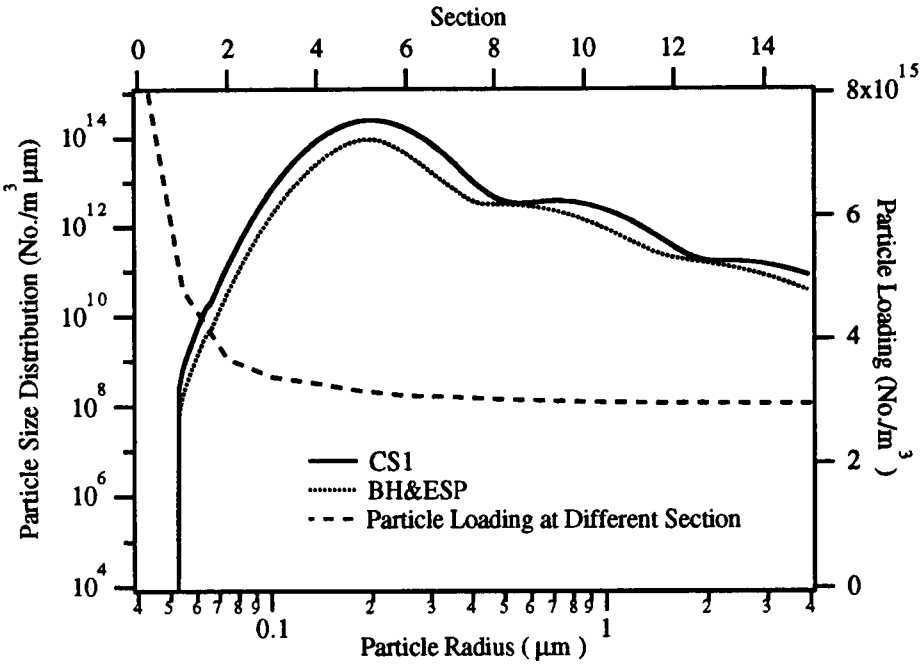


Figure 3.3.8 Predicted PSD and Particle Loading From CS1 to the BH and ESP Inlet

3.4 Theoretical Calculation with Particle Injection

At CFFF, ash particles collected at the BH and ESP were fed back into the flow train at the location of the outlet of the secondary combustor. The ash was cooled to the temperature of the surrounding air and was filtered to get rid of very large particles. The details of injector is described in Appendix I.

Injection was carried out when MHD flow was stable. The mass flux of the injection was controlled by adjusting air pressure. In the test, only a mass flux at 40psi was injected. In the subsequent test, 10psi, 20psi, 30psi, and 40psi resulting mass flux as were tested. Since these different air pressures resulted in only slight differences at the inlet of the BH and ESP, and 40psi air pressure was measured by a five stage cyclone measurement, the

mass loading at 40psi is used to discuss the particle injection. Figure (3.4.1) shows the measured PSD with different injected mass fluxes.

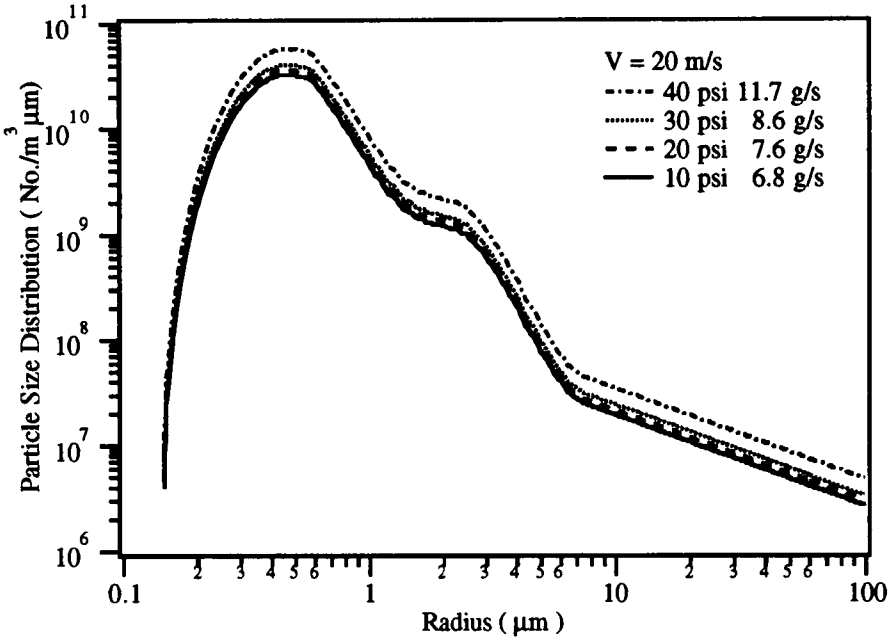


Figure 3.4.1 Measured PSD of Injected Particles at Different Mass Loading

At the injection section, the theoretical PSD with thermophoresis and injection is plotted in Figure (3.4.2).

3.4.1 Evolution of Particle Size Distribution from the Secondary Combustor to TS1 with particle injection

If injection is added, the coagulation equation is modified with four terms, condensation, heterogeneous nucleation, thermophoresis and injection. The PSD at CS1 is plotted in Figure (3.4.3). This PSD is the initial PSD for the next calculation from CS1 to the BH and ESP.

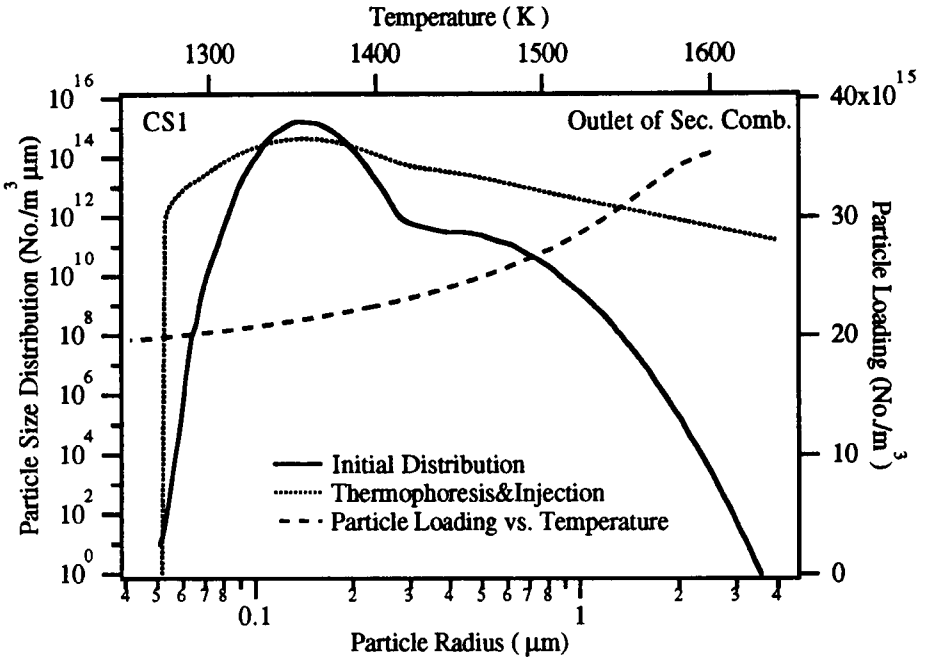


Figure 3.4.2 Predicted PSD at Injection Section and Particle Loading with Injection

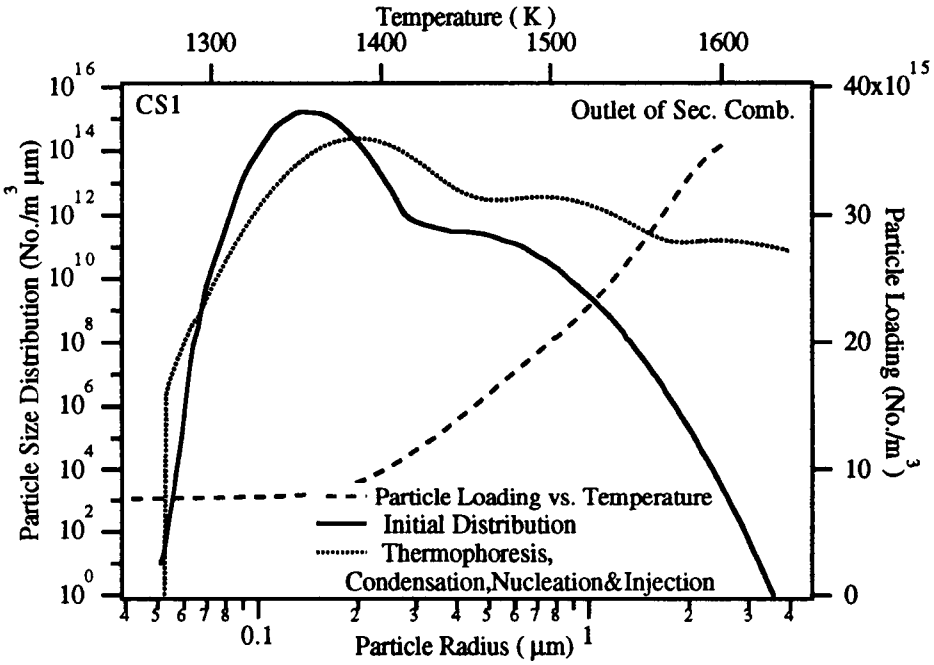


Figure 3.4.3 Predicted PSD and Particle Loading at Injection Section with Injection

3.4.2 Evolution of Particle Size Distribution from CS1 to the Inlet of the BH with Particle Injection

When particles are injected at the transition section, the particle size distribution at CS1 is lower than that without injection. The predicted PSD at the inlet of the BH and ESP with PSD at CS1 as initial PSD is plotted in Figure (3.4.4).

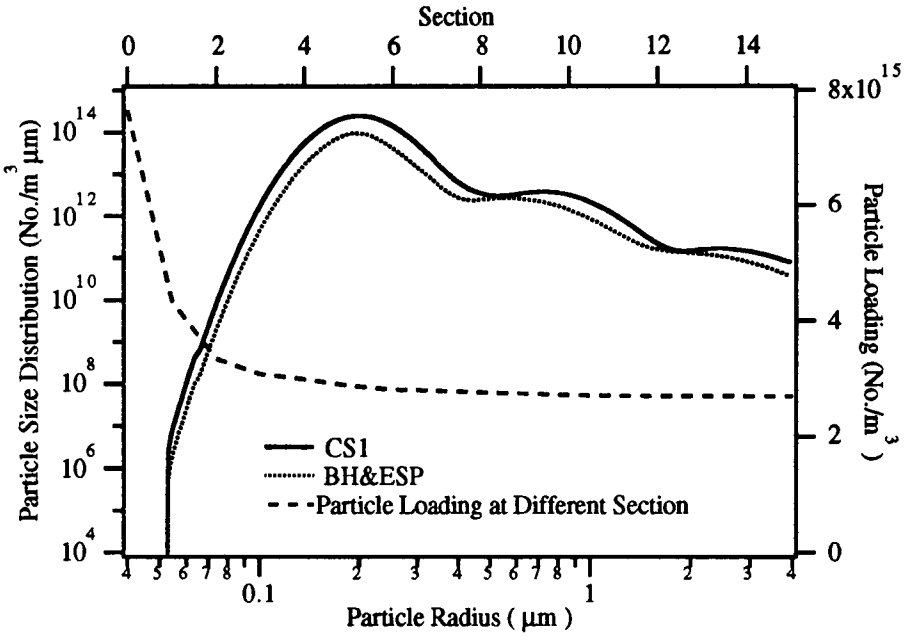


Figure 3.4.4 Predicted PSD and Particle Loading at the BH and ESP Inlet

3.5 Comparison of Theoretical and Experimental Results with Injection and without Injection

In this section comparisons are made to give particle size distribution and particle loading differences between with injection and without injection. Figure (3.5.1) gives the theoretical PSD at the CS1 section. It is clear to seen that even with particles injected into the original flue gas flow, the PSD with the injection is lower than the PSD without the

injection, especially in the smaller size region. This indicates that the PSD is affected by injection under the same flow conditions.

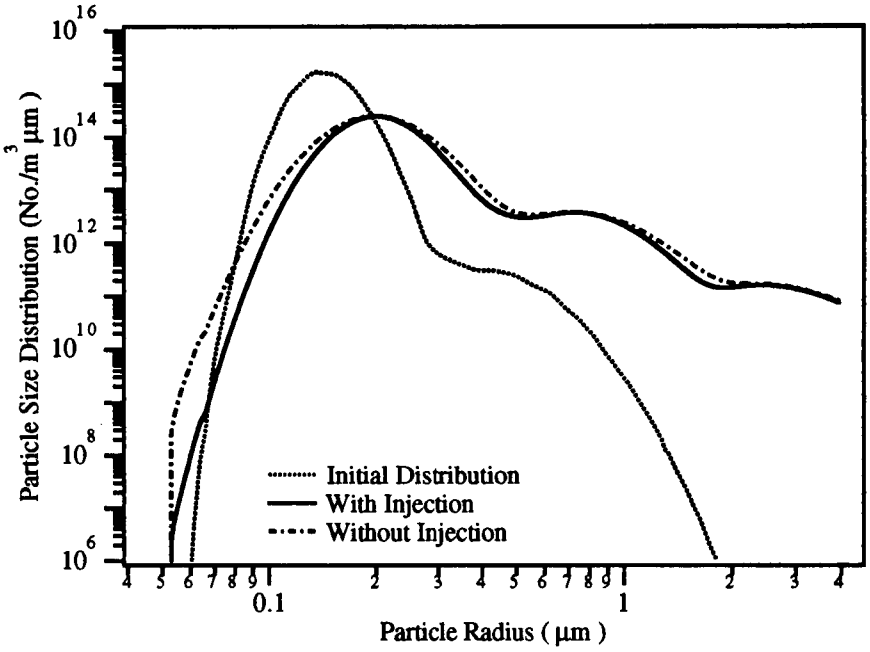


Figure 3.5.1 Predicted PSD at CS1 with and without Injection

Figure (3.5.2) shows the particle loading in the different locations, which is represented by different temperatures. It also shows that the total number of the particles with more particles added in the original flow does not increase the total number of the particles, but decreases the particle loading. Condensation, heterogeneous nucleation and thermophoresis cause more particle agglomeration and decreases particle loading in the flow even with additional particles introduced into the system.

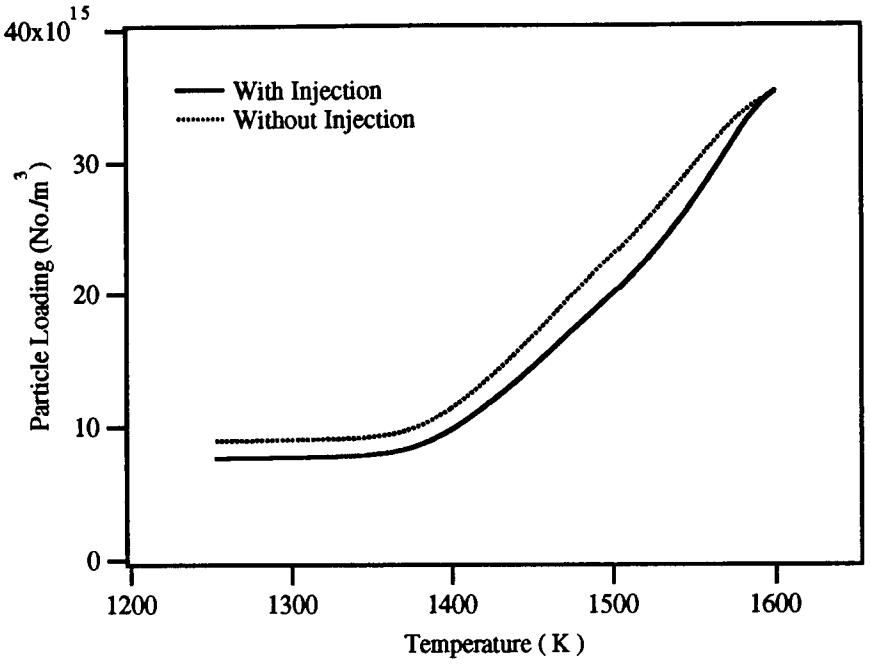


Figure 3.5.2 Particle Loading vs. Gas Temperatures From the SC to CS1

After the injection section, thermophoretic coagulation plays a major role in particle agglomeration. Figure (3.5.3) gives the comparison of the predicted PSD at the inlet of the CFFF BH and ESP. The PSD at the outlet of the CS1 is used as the initial particle size distribution for this prediction. The predicted particle loading is plotted in Figure (3.5.4). These two plots of the predicted PSD and the particle loading also show that particle injection reduces particle concentration. At the inlet of the BH and ESP, the lower PSD and total number of particles with injection is the result of the lower PSD and total number of particles at CS2.

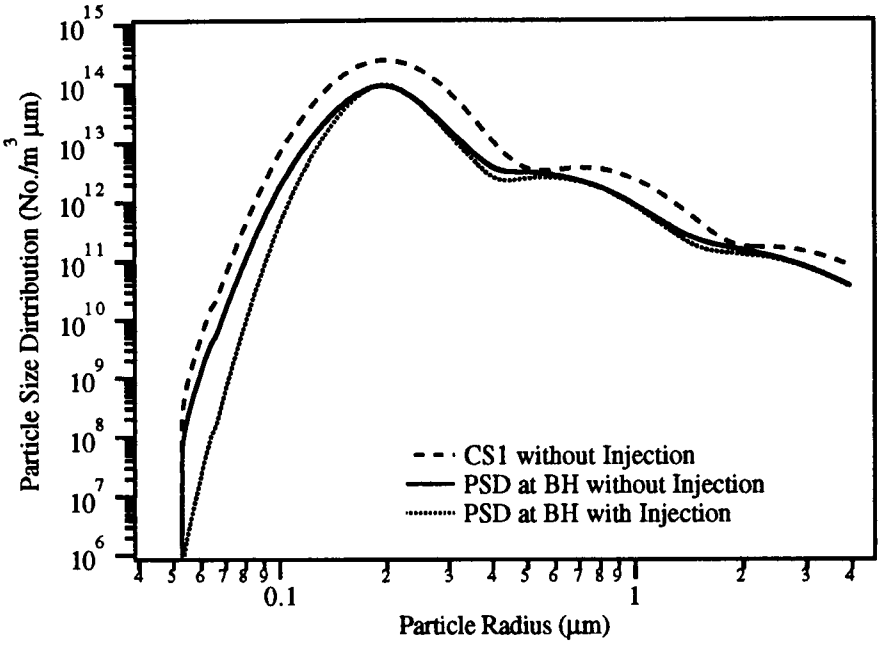


Figure 3.5.3 PSD at the inlet of the BH and ESP with and without Injection

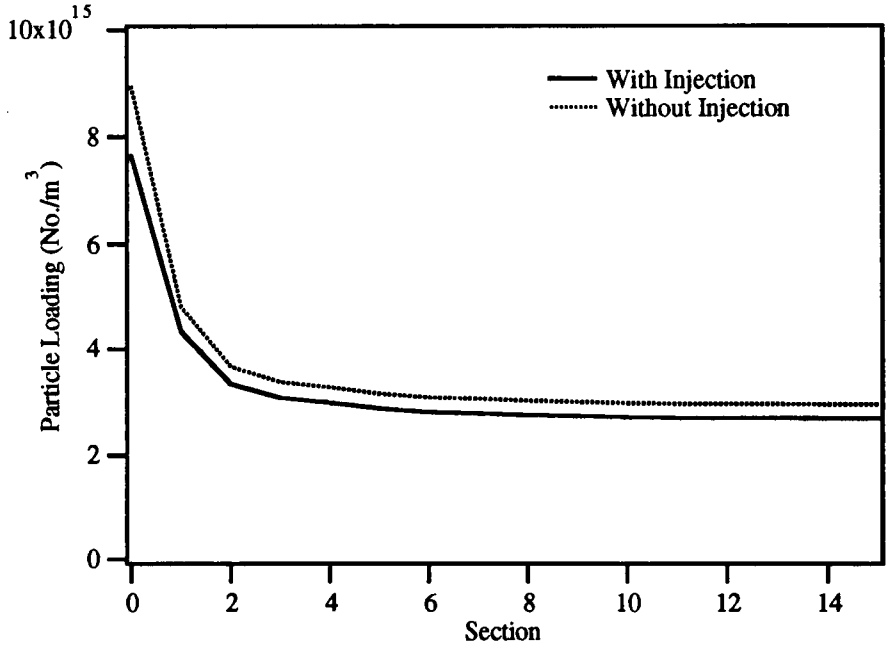


Figure 3.5.4 Particle Loading at Different Section

There are few experimental data sets available. With 5-stage cyclone, there were two sets of data taken with particle injection. These two sets of the data with two sets of data without injection are plotted in Figure (3.5.5). From the Figure (3.5.5), it can be seen that 5-stage cyclone method confirms a decrease in the small particle sizes due to the injection, but because it only provides 6 sizing ranges, no change is obvious in the larger particle size regimes. The Insitec's probe could not measure below 0.7μm in the heavily loading flow at the BH and ESP inlet, and so could not indicate the most significant effects of particle injection.

Figure (3.5.6) compares theoretical predications and experimental measurements at the BH and DESP inlet. The theoretical calculation basically matches the experimental results except at the large particle size end. This theoretical calculation predicts more agglomeration of fine particles with particle injection. The differences between theory and experiment are caused by many factors, including measurement methods, impinging, turbulence.

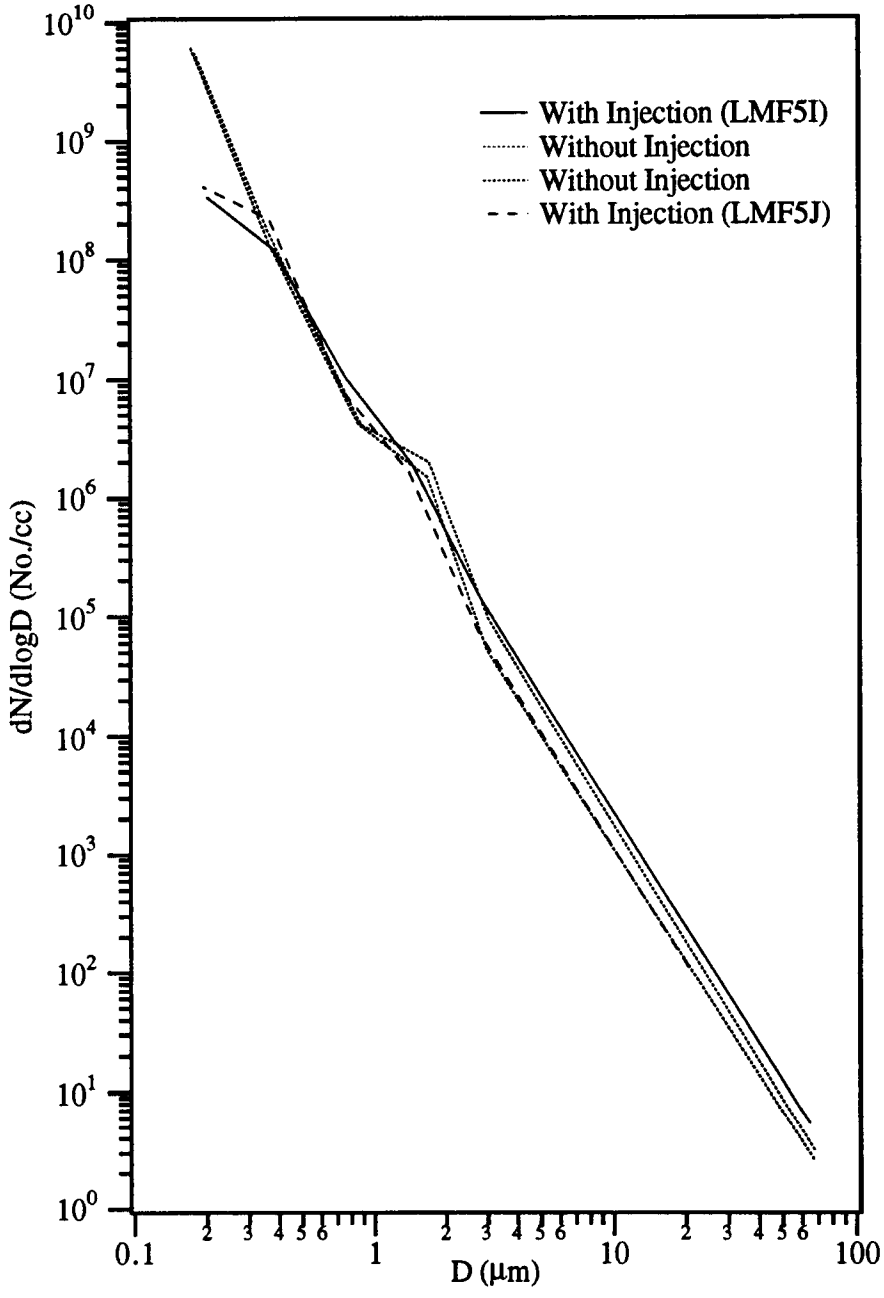


Figure 3.5.5 Experimental Measurements with and without Injection

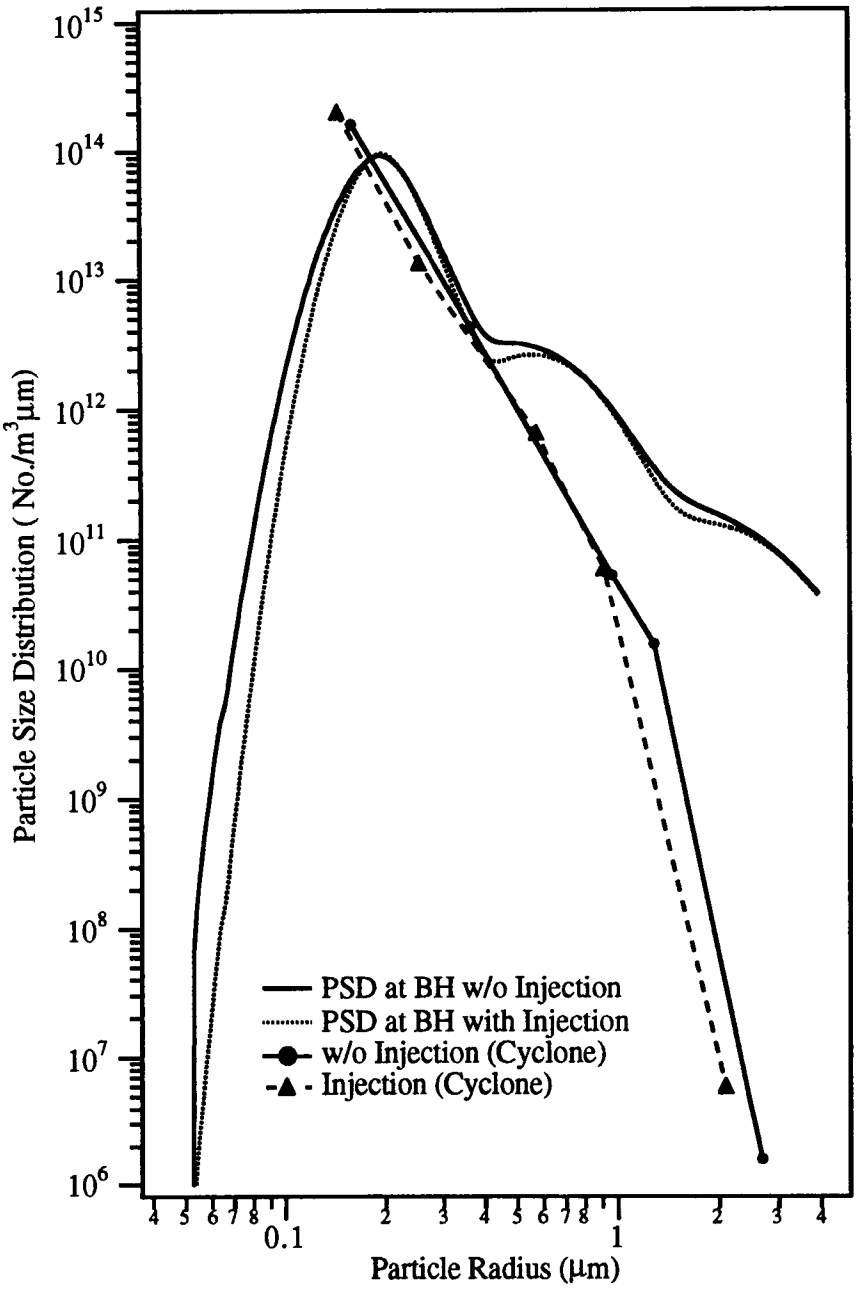


Figure 3.5.6 Comparison of Theoretical and Experimental Results

CHAPTER 4 CONCLUSIONS

A method of particle injection for enhancing particle agglomeration is developed in this dissertation. With a small amount of cool particles injected into a hot particle-gas flow containing a huge number of fine particles (i.e.,0.05μm), the fine particles will agglomerate to the larger particles, which are in both the original flow and the injected particle flow, by mechanism of thermophoresis. If there is a supersaturated vapor phase, condensation and heterogeneous nucleation will cause particle growth. With the correct combination of injected particle size distribution and velocity, this enhancement can be maximized.

In this dissertation, three phenomena related to particle growth, thermophoresis, condensation, and heterogeneous nucleation, have been evaluated. Thermophoresis, as a mechanism of fine particle agglomeration in gas-solid particle flow in a flow duct, can be applied to any similar systems, but condensation and nucleation are only applied to a system in which a vapor phase exists, for instance at the CFFF secondary combustor.

Each phenomena has its own properties for particle growth. Thermophoretic coagulation takes place where there is any temperature gradient. In the CFFF exhaust flow duct, different sizes of particles have different temperatures, thus creating a temperature gradients around larger particles which have lower temperatures than the smaller particles. The smaller particles are driven to the larger particles by the thermophoretic force. The smaller particles will collide with the larger particles and after adhere together. The thermophoretic collection efficiency of the larger particles is proportional to the number density of the larger particles. With particle injection, the number density of larger, cooler particle will

increase so that their collection efficiencies also increase. Therefore, thermophoretic coagulation increases with particle injection. Condensation occurs between vapor phase and liquid phase of K_2SO_4 or K_2CO_3, which is in the supersaturated state after the secondary combustor of the CFFF. Along with condensation, nucleation simultaneously takes place. With cold particle injection, the nucleation rate is increased causing nucleating particle growth. The nucleated vapor molecules form a condensed liquid layer on the nucleating particles. This liquid layer will also interact with the vapor phase to drive more condensation, which can be treated as condensation growth. In addition to these particle growth mechanisms, there are some liquid droplets formed by homogeneous nucleation as the vapor phase cools, and this can also be treated as condensation growth. However, homogeneous nucleation produces few particles since homogeneous nucleation rarely occurs before the other mechanisms deplete the vapor phase.

In the theoretical model particle injection reduces the particle loading from $3.85x10^{+16}/m^3$ to $3.0x10^{+15}/m^3$. The model indicates that particle loading reduces to $3.5x10^{+15}/m^3$ without injection. The mean particle size increases from 0.4μm to 0.6μm with a mass flux of injected particle of only 5 percent of that in the original flow. With the increase in particle size and decrease in particle loading, it is expected that emission control equipment will have higher efficiency. For the CFFF, heat transfer efficiency is also expected to rise due to less deposition on the surfaces of the heat exchanger tubes since, as was pointed out by Im, the surfaces have a has higher collection efficiency for small particles (i.e., 0.1μm) due to thermophoresis.

The particle injection method of particle agglomeration will overcome the disadvantages of the electrical induction method and the acoustic agglomeration method and can be more economically employed.

The theory compares reasonably well with experimental measurements at the CFFF. As mentioned before, differences between the theory and experiment are produced from both theoretical and experimental inadequacies. The theory needs further development in a number of areas. For example, the interaction between ash particles and vapor K_2SO_4, which may provide different expressions for the condensation growth rate and the heterogeneous nucleation rate and this needs to be better modeled. At this point, however, experimental improvements are more important. The entire theoretical prediction is based on the 5-stage cyclone measurement at the outlet of the secondary combustor. This measurement gives six points to define a particle size distribution. Because condensation occurs in and on the 5-stage cyclone, different interpretations of the particle size distribution are possible and the interpretations result in very different final distributions at the BH and ESP. At the outlet of the secondary combustor, the flow is turbulent and is in a three-phase state, making it very difficult to measure the particle size distribution with a collection device like 5-stage cyclone. At the inlet of the BH and ESP, more precise measurement equipment is also needed. Since there is difference of an order of magnitude between the PSD with and without particle injection, it is desired that diagnostic equipment gives a real-time distribution to detect the small particle the injection effects and gives high resolution in the PSD to clearly distinguish the injection and non-injection PSDs. For high mass loading flow, it is very hard to achieve this measurement with currently available measurement systems. It may be necessary to set up a laboratory system with lower particle loadings to study this phenomenon more closely using available instrumentation.

CHAPTER 5 RECOMMENDATIONS

Recommendations to further improve understanding of the particle growth by thermophoresis are given in this chapter. Primarily, a laboratory study is recommended, which addresses the many problems. Some theoretical problems also need more study (i.e., rate of heterogeneous nucleation, collection efficiency of larger particles), but the laboratory study is needed first to provide data to improve the theory.

5.1 Laboratory Study and Apparatus

Because of the complexity of the CFFF, the experimental data is affected by many factors, such as the structure of the flow train, heat exchanger tubes in the flow train, soot blowing of these tubes, and difficulties of sampling the small size high number concentration of particles with adequate resolution and time response, a laboratory study where these problems can be avoided is desired. This laboratory set-up should include a high temperature burner, which can produce high temperature three phase particle-gas flow with adjustable mass loading and also simulate the conditions of the corresponding ducting at the CFFF without the heat exchanger tube complexities. A flow train which can flow the three phase gas-particle mixture with gradual cooling is also needed. The flow duct is required to have a large enough diameter in order to minimize the effects of the duct walls and have a small enough diameter to not need too large mass flow. The duct should have at least three pairs of ports: one pair for cold particle injection, and two pairs for two diagnostic devices. Finally, two sets of the diagnostic equipment are needed. A laser optical system with fast

time response that has the precise particle size measurement capability, including size resolution and loading, and has the least interference with the flow, would be ideal if it can be identified.[40,41,42] One set of the diagnostics would be is used to measure the particle size distribution before particle injection while the other would be used after the injection. Because a long straight duct with well controlled hot three-phase particle flow and cold particle injection, at a light mass loading of both the original and the injected flow, for adequate optical diagnostics can be achieved in the laboratory, the theory developed in this dissertation can be examined closely in the laboratory. The proposed laboratory test configuration is given in Figure (5.1).

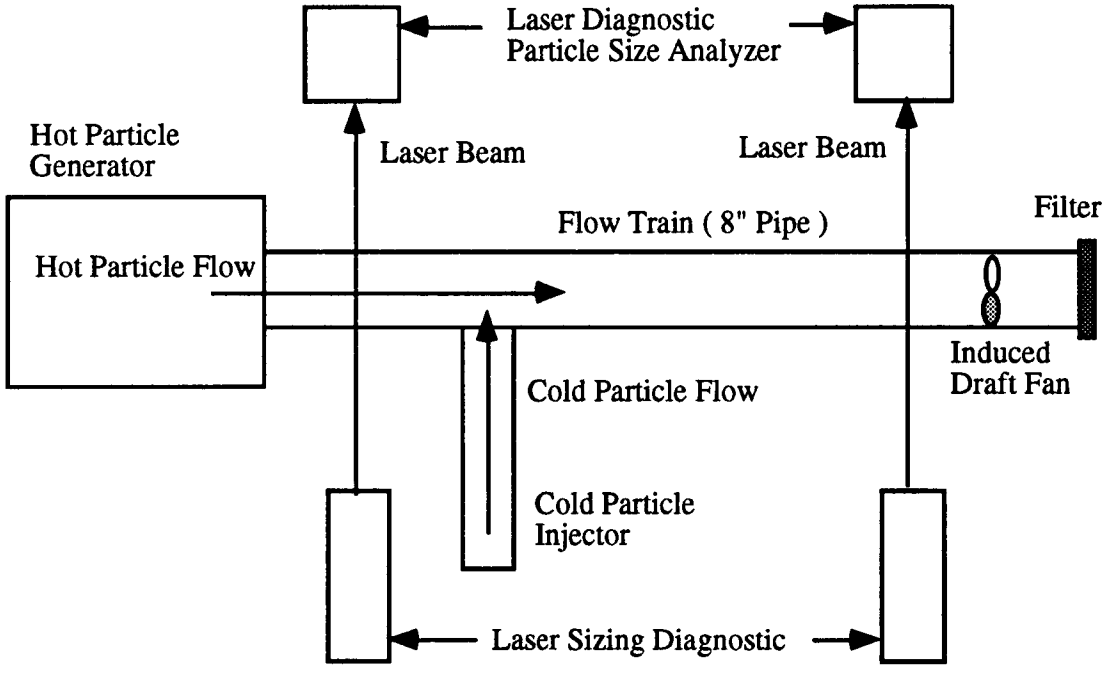


Figure 5.1 Proposed Laboratory Test Configuration

Besides particle size distribution, other problems, like relative velocities and temperatures of individual particles and the walls, will be experimentally adjustable in order to confirm the thermophoretic coagulation theory although it is theoretically reasonable.

5.2 Study of Collision Efficiency of Large Particle

From the analysis of collection efficiency due to the thermophoresis, one can see that the temperatures of the injected particles will affect particle agglomeration, as well as the injection velocity relative to flow velocity. It must, however, be remembered that this analysis deals only with the motion of single particles agglomeration from smaller diameter and as such, neglects the important contributions of aerodynamic and thermal interaction forces between the two particles. Further study is needed to treat the interaction of two particles during the transition time, which is the time requires for the injected particles to reach their equilibrium temperatures.

Collection efficiency under the different conditions and forces has been studied for years,[43,44,45,46,47] but thermophoretic collection. As two particles come closer together, they start to influence each other aerodynamically and thermodynamically. It is these interactions which finally determine whether or not the two approaching particles will or will not collide. The calculation of the effects of these interaction forces requires the use of particle collision cross sections which are different from the geometrical collision cross section, determined solely by the size of the particles. Figure (5.2) illustrates a possible grazing trajectory of particle 2 relative to particle 1. The effective collision cross section is πy_i^2, where y_i, the impact parameter, is defined such that when particle 2 is placed within the boundary defined by this impact parameter, a collision between particle 1 and 2 does take place. The ratio of the effective collision cross section, πy_i^2, to the geometrical collision cross section, $\pi(a_1+a_2)^2$, i.e.,

$$\eta_{12} = \frac{\pi y_i^2}{\pi(a_1 + a_2)^2} = \frac{y_i^2}{(a_1 + a_2)^2}. \qquad (5.1)$$

is defined as the collection efficiency.[48]

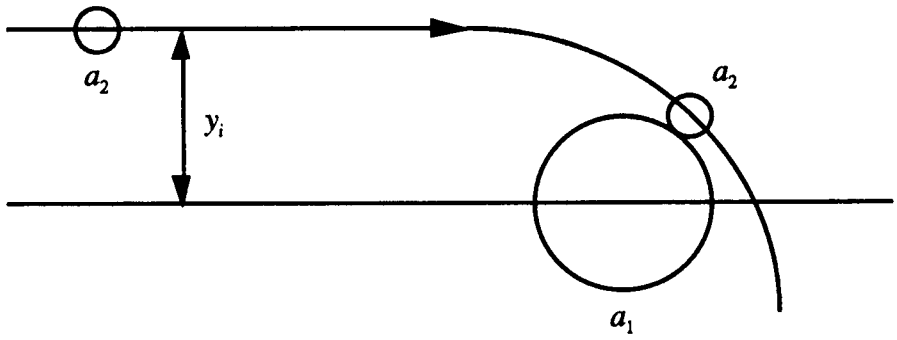


Figure 5.2 Illustration of Collection Efficiency

The determination of the collision efficiency is very important but rather involved mathematically because several different physical phenomena affect it simultaneously. The collision efficiency of a pair of particles, for example, is determined by the trajectories of the particles when they are subjected to gravitational, aerodynamic and thermal forces. Generally, the motion of a particle can be described by Eq.(C.4) and Eq.(C.5) and the thermophoretic force is described by Eq.(D.27). If all the forces are known, the equations of motion can be integrated numerically and trajectories obtained from given initial conditions. Repeating this process and changing the initial conditions, the grazing trajectory can eventually be established and the collision efficiency determined.

If two colliding particles with radii a_1 and a_2, masses m_1 and m_2, temperature T_1 and T_2, respectively, are moving with velocities U_1 and U_2 in the x-direction, and V_1 and V_2 in the y-direction, then the equations of motion can be written as follows: (see Appendix C and D)

$$m_1 \frac{dU_1}{dt} = F_{1x} - 6\pi\mu a_1 U_1$$

$$
\begin{aligned}
m_2 \frac{dU_2}{dt} &= F_{2x} - 6\pi\mu a_2 U_2, \\
m_1 \frac{dV_1}{dt} &= F_{1y} - 6\pi\mu a_1 V_1, \\
m_2 \frac{dV_2}{dt} &= F_{2y} - 6\pi\mu a_2 V_2, \\
\frac{dx_1}{dt} &= U_1, \\
\frac{dx_2}{dt} &= U_2, \\
\frac{dy_1}{dt} &= V_1, \\
\frac{dy_2}{dt} &= V_2,
\end{aligned}
\tag{5.2}
$$

These equations constitute an interlocking system of eight equations for eight unknowns. If the thermal force and the aerodynamic force are given, one can integrate these equations to solve for the trajectory of each of the particles starting from given initial conditions.

5.3 Heterogeneous Nucleation

The rate of the heterogeneous nucleation for an individual particle, Eq.(F.24), is an approximate expression. Since Fletcher first introduced this formula, three decades have passed without significant improvements.[49,50] It is difficult to find papers related to heterogeneous nucleation on particles. For an MHD system, it is important to study this phenomenon since MHD has higher temperature combustion, which produces more fine particles than conventional coal-fired combustion, and high temperature combustion with potassium seed adds the interaction of potassium and sulfur to form K_2SO_4 and K_2CO_3 in a supersaturated vapor state. This vapor K_2SO_4 will nucleate homogeneously and heterogeneously. But details of the vapor K_2SO_4 nucleating on the surfaces of the ash particles is not clear. Further study is necessary to understand this process. It may be

important in the future to reduce pollution, such as sulfur compound emissions produced in the power plants.

LIST OF REFERENCES

1 Elliott, M. A. and Yohe, G. B., " The Coal Industry and Coal Research and Development in Perspective", Chemistry of Coal Utilization, edited by M.A. Elliott, John Wiley & Sons, Inc., 1981.

2 Fuchs, N. A., The Mechanics of Aerosols, New York, The MacMillan Co., 1964.

3 Patterson, H. S. and Cawood, W., Nature , V. 127, p. 667, 1931.

4 Newmann, E. P., and Norton, J. L., Chem. Eng. Prog. Sym., Sec. 1, V.47, 1, 4 (1951)

5 Nord, M., Chem. Eng.,V.57, 10, 116 (1950).

6 Boncher, R. M. G., Chem. Eng., V.68, 20, p.83 (1961).

7 Mednikov, E.P., Acoustic Coagulation and Precipitation of Aerosols, English translation by Consultants Bureau, New York, 1966.

8 Melcher, J. R., and Sachar, K. S., "Electrical Induction of Particulate Agglomeration," National Technical Information Service, U. S. Department of Commerce, 1971.

9 Dahlin, R.S., Snyder, T.R., and Bush, P.V., "Effects of Sorbent Injection on Particulate Properties: Part 1. Low-Temperature Sorbent Injection," ISSN 1047-3829, J. Air&Waste Managenment Association, V.42, 1992.

10 Dahlin, R.S., Snyder, T.R., and Bush, P.V., "Effects of Sorbent Injection on Particulate Properties: Part 2. High-Temperature Sorbent Injection," ISSN 1047-3829, J. Air&Waste Managenment Association, V.43, 1992.

11 Epstein, P.S., Zeitschrift fuer Physik , V.54, p.537-563, 1929.

12 Talbot, L., Cheng, R.K., Schefer, R.W. and Willis, D.R., "Thermophoresis of Particles in a Heated Boundary Layer" , J. Fluid Mech. V. 101, part 4, pp.737-758, 1980.

13 Im, Kwan H. and Chuang, Paul M., "Particulate Deposition form Turbulent Parallel Streams", Argonne Report, ANL/MHD-81-2, 1981.

14 Im, Kwan H. and Chuang, Paul M., "Slag and Other Liquid Behavior on Vertical Surface at Near-Freezing Temperature", AIAA Journal, V.18, No.11, 1980.

15 Weinberg, Michael C., "Efficiency Improvement in Thermophoretic Deposition" , Communications of the American Ceramic Soc. C-30, 1983.

16 Park, H. M. and Rosner, D.E.,"Combinaed Inertial and Thermophorestic Effects on Particle Deposition Rates in Highly Loaded Dudty-gas Systems", Chem. Engineering Science, V. 44, No.10, p.2233-2244, 1989.

17 Postma, Arlin K., "Thermophoretic Separation of Aerosol Particles from a Sampled Gas Stream", U.S. Patent number 4572007, 1986.

18 Yang, D. and Crawford, L. W., "Thermophoresis in Mechanism of Agglomeration of Fine Particles in Magnetohydrodynamic Systems", AIAA 93-3211, Orlando, FL., July 6-9, 1993.

19 Yang, D. and Crawford, L. W., " Evolution Of Particle Size Distribution After the CFFF Secondary Combustor ", 31st Symposium on SEAM, Whitefish, Montana, June, 1993.

20 Li, Jun, Master Thesis, University of Tennessee, 1991.

21 Data provided by M. White.

22 Holve, D.J. and Bonin, M. P., "In-situ Measurements of Particulates from MHD Combustion Processes", First Semi-Annual Report, DOE Grant #DE-FG03-91ER81124, November 1992.

23 Parker, J.L., Giel, T.V., Winkleman, B.C., Hodges, M.E., Holt, J. K., and Douglas, J. R., "Development of a Particle Monitor for the CFFF", 31st SEAM, Whitefish, Montana, June, 1993.

24 Brock, J.R., J. Colloid Science, V.17, p768-780, 1962.

25 Prasad, J., "Mechanisms of Agglomeration of Fine Particles in a Magneto-hydrodynamic System," Thesis, The University of Tennessee, Knoxville, 1981.

26 Williams, F. A., Combustion Theory, Addison-Wesley Publishing Company, Inc., 1965.

27 Brock, J. R., "Processes, Sources and Particle Size Distribution," Faraday Symposia of the Chemical Society No. 7, Fogs and Smokes, The Faraday Division, Chemical Society, London, 1973.

28 Friedlander, S.K., in Aerosol: Physical Chemistry and Applications, ed. K. Spurny, Gordon&Breach, Inc., N.Y., 1965.

29 Mockros, L., Quon, J. and Hjelmfelt, T., Jr., J. Colloid Interface Sci., V.23, 90, 1967.

30 Smoluchowski, M. V., Z. Physik. Chem., V.92, 129, 1917.

31 Smoluchowski, M. V., Z. Physik., V.17, 557, 1916.

32 Hidy, G. M. and Brock, J. R. , The Dynamics of Aerocolloidal Systems, First Edition, Pergamon Press Inc., 1970.

33 Hidy, G.M. and Lilly, D.K., "Solutions to the equation for the kinetics of coaglation", J. Colloid Science, V.20, p.867-874, 1965.

34 Drake. R., Topics in Current Aerosol Research, Part II, (G.M. Hidy and J.R. Brock, ed.), Pergamon Press. Oxford, 1971.

35 Berry, E.X., "Cloud Droplet Growth by Collection," J. Atmopheric Sciences, V. 24, p.688, 1966.

36 Middleton, P. and Brock, J.R., " Simulation of Aerosol Kinetics", J. Colliod and interface Sci., V.54, No.2, 1976.

37 Eliezer, I. and Howald, R. A., "Thermodynamics of the Vaporation Processes for Potassium Sulfate," J. Chem. Phys., V.65, No. 8, 1976.

38 Gurvich, L.V., Dorofeeva, O.V., and Yungman, V.S., "The Thermodynamic Functions of Gaseous K2SO4 and Cs2SO4 in the Standard State", Argonne National Laboratory, ANL-77-21, 1977.

39 Hirsch, C., Numerical Computation of Internal and External Flows, Vol. 2, John Wiley & Sons, 1990.

40 Farmer, M., "Measurement of Particle Size, Number Density , and Velocity Using a Laser Interferometer", Applied Optics , V.11, No.11, 1972.

41 Yamauchi, T. and Ohyama, Yoshishige, "A Study on the Measurement of Particle Size Distribution with Laser Diffraction System", Bulletin of the JSME, V.25, No.210, 1982.

42 Edith, Thomalla and Heinrich, Quenzel, "Information Content of Aerosol Optical Properties with Respect to Their Size Distribution" , Applied Optics, V. 21, No.17, 1982.

43 Davis, M. H. and Sartor, J.D. "Theoretical Collision Efficiencies for Small Cloud Droplets in Skokes Flow", Nature, V.215, 1967.

44 Shafrir, Uri and Neiburger, Morris, " Collision Effeciencies of Two Spheres Falling in a Viscous Medium for Reynolds Number Up to 19.2", University of California Press, 1964.

45 Kobashi, M., "Particle Agglomeration Induced by Alternating Electric Fields", Dissertation, Stanford University, 1979.

46 Lindblad, N.R. and Semonin, R.G., "Collision Efficiency of Cloud Droplets in Electriv Fields", Journal of Geophysical Research, V.68, No.4, Feb. 1963.

47 Hocking, L.M., " The Collision Efficiency of Small Drops", Quart. J. Roy. Meteorol. Soc., V.85, p.44-50, 1959.

48 Mason, B. J., The Physics of Clouds, Claredon Press, Oxford, Second Edition, 1971.

49 Kotake, S. and Glass, I. I., "Condensation of Water Vapor in Rarefaction Waves: Heterogeneous Nucleation," AIAA Journal, V.15, No.2, Feb., 1977.

50 Chen, M.S. and Jones, B.W., "Condensation by heterogeneous nucleation in a thermal boundary layer", Int. J. Heat and fluid flow, V.11, No. 4, 1990.

51 Im, K. H. and Chung, P. M., "Nucleation anf Evolution of Slag Droplets in Coal Combustion", AIChE Journal, July, 1980.

52 Sedunov, Yu. S. , Physics of Drop Formation in the Atmosphere, John Wiley & Sons, Ltd., 1974.

53 Dunning, W.J., Nucleation, A.C. Zettlemayer, ed., Chapter 1, Marcel Dekker, New York, 1969.

54 Feder, J., Russell, K. C., Lothe, J. and Pound, M., "Homogeneous Nucleation and Growth of Droplets in Vapours," Adv. in Phys., V.15, 111, 1966.

55 Brock, J.R., J. Colloid Interface Science, V.23, p.448-452, 1967.

56 Waldmann, L., Rarefied Gas Dynamics, (L. Talbot, ed.), Academic Press, N.Y., p.323-344, 1967.

57 Dwyer, H.A., Physics of Fluids, V.15, p.976-984, 1967.

58 Vestner, H., Kübell, M., and Waldmann, L., Nuovo Cimento, V.25, p.405-412 (1975).

59 Sone, Y., Physics of Fluids, V.15, p.1418-1423 (1972).

60 Derjaguin, B.V. and Yalamov, Yu., J. Colloid Science, V.20, p.555-570 (1965).

61 Williams, M.M.R., J. Phys. D: Appl. Phys., V.19, p.1631-1642 (1986).

62 Loyalka, S. K., "Momentum and Temperature Slip Coefficients with Arbitary Accommodation at the Surface" J. Chem. Phys., V. 48, No. 12, 1968.

63 Talbot, L., Rarefied Gas Dynamics, (S.S. Fisher, ed.), V.74. Pt. 1, p.467-488, Progress in Astronautics and Aeronautics, AIAA, New York, 1981.

64 Williams, M.M.R., J. Phys. D: Appl. Phys., V.19, p.1631-1642, 1986.

65 Williams, M.M.R., J. Phys. D: Appl. Phys., V.20, p.354-359, 1987.

66 Williams, M.M.R., J. Colloid and Interface Science, V.122, No. 1, p.110-119, 1988.

67 Reed, L.D. and Morrison, Jr., F. A., " Motion of an Aerosol Particle in an Unsteady Temperature Gradient", J. Colloid and Interface Science, V. 42. No.2, Feb. 1973.

68 Morse, P.M. and Feshbach, H., Methods of Theoretical Physics, Part II, McGraw-Hill, New York, 1953.

69 Happel, J. and Brenner, H., Low Reynolds Number Hydrodynamics, Prentice-Hall, Englewood Cliffs, New Jersey, 1965.

70 Reed, L.D. and Morrison, F.A., Jr., J. Aerosol Science, V.6, p.349-365, 1975.

71 Kennard, E.H., Kinetic Theory of Gases, McGraw-Hill, New York, 1938.

72 Schaaf, S.A., "Recent Progress in Rarefied Gasdynamics", ARS J., V.30, No. 5, pp.443 (1960).

73 Schaaf, S.A., and Chambre, P.L., "Flow of Rarefied Gases; in High Speed Aerodynamics and Jet Propulsion", III , Sec. H, pp.687, Princetion, 1958.

74 Stimson, M. and Jeffery, G.B., Proc. R. Soc., A111, 110, 1926.

75 Yang, D., "Thermophoretic Force Acting on a Sphere in a Temperature Gradient by a Spherical Heat Source", AIAA Paper 93-2856, Orlando, FL., July 6-9,1993.

76 Reid, R.C., and Sherwood, T. K., The Properties of Gases and Liquids, 2nd. ed., McGraw-Hill Book Company, 1966.

77 Vincenti, W. G., and Kruger Jr., C. H., Introduction to Physical Gas Dynamics, John Wiley & Sons, Inc., 1965.

78 Abraham, F. F., Homogeneous Nucleation Theory, Academic Press, 1974.

79 Volmer, M. and Weber, A., Z. Phys. Chem. V.119, 277(1925).

80 Hirth, J. and Pound, G., Condensation and Evaporation, Pergamon, N. Y. , 1963.

81 Hirth, J. and Pound, G., J. Chem. Phys. V.36, 630, 1966.

82 Reiss, H., Katz, J. and Cohen, E., J. Chem. Phys., V.48, 5553, 1968.

83 Volmer, M., Kinetik der Phasenbildung, Steinkopff, Dresden, 1939.

84 Fletcher, N. H., The Physics of Rainclouds, Cambridge University Press, 1962.

85 Fletcher, N. H.,"Size Effect in Heterogenous Nucleation ", J. Chem. Phys., V.29, No.3, 1958

86 Batchelor, G. K., Proc. Cambridge Phil. Soc, V.47, 359, 1951.

87 Schlichting, H., Boundary Layer Theory, Sixth Edition, McGraw-Hill Book Company, 1968.

88 Incropera, F.P., and DeWitt, D.P., Fundamentals of Heat and Mass Transfer, Third Edition, John Wiley&Sons, Inc., 1990.

89 Wagoner, C. L., Foote, John P., el. " Advanced Combustion System For Industrial Boilers, Final Report, Phase II Activities", DOE Contract No. DE-AC22-87PC79653, December, 1991.

APPENDICES

APPENDIX A THEORETICAL PREDICATION OF INITIAL PARTICLE SIZE DISTRIBUTION AND EXPERIMENTAL MEASUREMENTS AT CFFF

Theoretical predictions of the particle size distribution in an MHD system was first investigated by K. H. Im and Paul M. Chung.[51] Since this study is very important to this dissertation, it is briefly discussed in this section and then compared with the particle size distribution measurements at the CFFF. In their research, formation of slag droplets from MHD combustion vapor and the evolution of the droplet sizes in the generator or after bottoming cycle was studied. Specifically, Im and Chung considered that a gaseous mixture containing certain initial amount of slag vapor and slag droplets was given. Also given initially are the size distribution of slag droplets and properties of the gas mixture. Their analysis was based on the solution of the spray equation[26] in the time-size coordinate system with appropriate kinetics describing the nucleation and the droplet size variation with time.

Governing Equations

It is considered that gas and slag droplets are mixed spatially homogeneous at $t=0$. All necessary properties of the mixture including the number density and size distribution of the droplets are considered to be given at the initial time. Then the time evolution of the number density of the various size droplets is governed by the spray equation:

$$\frac{\partial n(r,t)}{\partial t}+\frac{\partial}{\partial r}[\dot{r}n(r,t)]=J(r,t)\delta(r-r^{*}). \tag{A.1}$$

On the other hand, conservation of the slag vapor in the system is described by the equation:

$$\frac{\partial \rho_v}{\partial t} = -4\pi\rho_l \int_{r_0}^{\infty} r^2 \dot{r} n(r,t) dr - \frac{4\pi(r^*)^3}{3}\rho_l J(r^*,t) + \frac{\rho_v}{\rho_g}\frac{\partial \rho_g}{\partial t} \qquad \text{(A.2)}$$

Eq.(A.1) for the droplets and Eq.(A.2) for the slag vapor are coupled. In order to solve them, the rate of the droplet growth and nucleation must be known.

Rate of Droplet Growth

The droplets carried out of the combustor are expected to have sizes of the order of several microns. The typical mean free path in the gas flowing in the MHD system is estimated to be of the order of a micron. Therefore, the droplet gas interactions would encompass the free molecular to the mixed interaction regimes, that is, the regimes where the Knudsen number is very large down to the order of 0.1. They divided the gas surrounding the droplet into two layers, the layer adjacent to the droplet surface of one mean free path thickness (Knudsen layer) and that outside of this layer.[52] The interface between the two layer is labeled as *b* in Figure (A.1). It is assumed that the state of the gas at *b* and beyond is in kinetic equilibrium; that is, the velocity distribution is near Maxwellian owing to the numerous gas-gas collisions. No gas-gas collision occurs between *b* and the droplet surface *s*. It is also assumed that slag vapor molecules emitted from the surface *s* are in a kinetic equilibrium at T_S.

The rate of droplet growth can be expressed as:

$$\dot{r} = \frac{m_e(I_+ - I_-)}{4\pi r^2 \rho} \tag{A.3}$$

where

$$I_- = 4\pi r^2 \left(\frac{n_{cs} V_{cs}}{4}\right) e^{\frac{\phi}{kT}} \tag{A.4}$$

and

$$I_+ = 4\pi r^2 \left(\frac{n_{cs} V_{cs}}{4}\right) \tag{A.5}$$

I_- is rate of emission of the slag vapor molecules from the droplet surface and ϕ is the energy function which represents the energy needed to vaporize molecules from the droplet of a given radius r. I_+ is mass rate of vapor moving from b toward the droplet surface.

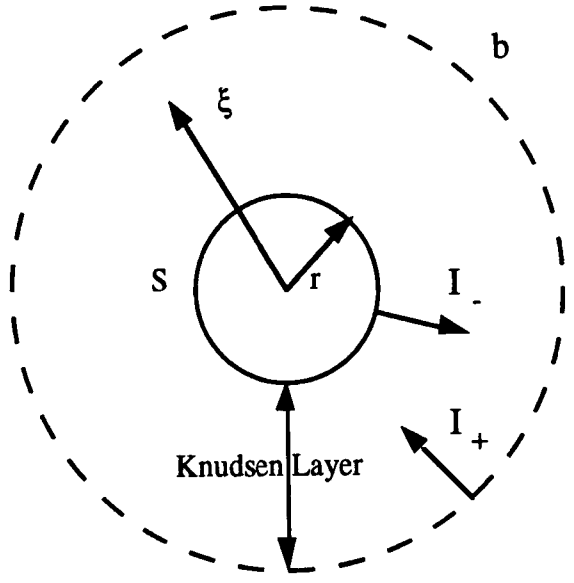


Figure A.1 Particle Growth Evaporation Model

In order to obtain I_+ and I_-, Im and Chung constructed vapor-mass and total energy balances at the interface b as

$$4\pi(r+\lambda)D_v(n_{c\infty} - n_{cb}) = 4\pi r^2 \left[\frac{n_{cb} v_{cb}}{4} - \frac{n_{cs} v_{cs}}{4} e^{\frac{\phi}{kT_s}}\right] \tag{A.6}$$

$$4\pi(r+\lambda)k(T_g - T_b) = 4\pi r^2\left[\frac{n_{cb}v_{cb}}{4}\left(\frac{3}{2}kT_b\right) - \frac{n_{cs}v_{cs}}{4}\left(\frac{3}{2}kT_s\right)\right]. \tag{A.7}$$

Because the vapor constitutes only a trace in the gas mixture, its effect on the above energy equation can be neglected.

Since the only properties given are those in the free stream, the two equations, Eq.(A.6) and Eq.(A.7) contain nine unknowns, n_s, n_{cb}, n_{cs}, v_b, v_{cb}, T_b, D_v, K, and T_s. Three simple relationships, however, can be readily obtained from the kinetic theory as,

$$v_b = \sqrt{\frac{8kT_b}{\pi m}} \quad \text{and } v_s = \sqrt{\frac{8kT_s}{\pi m}} \tag{A.8}$$

$$v_{cb} = \sqrt{\frac{8kT_b}{\pi m_c}} \quad \text{and} \quad v_{cs} = \sqrt{\frac{8kT_s}{\pi m_c}} \tag{A.9}$$

and

$$n_s v_s = n_b v_b = n_\infty v_b, \tag{A.10}$$

Diffusivity, D_v, and conductivity, K, can also be found in the kinetic theory.

$$D_v = \frac{3}{5} r \sqrt{\frac{8kT_g}{\pi m_c}} K_n, \tag{A.11}$$

$$K = \frac{15}{8} k n_\infty r \sqrt{\frac{8kT_g}{\pi m}} K_n, \tag{A.12}$$

In addition, n_{cs} is the number density of the vapor molecules corresponding to the saturated state at T_s. Therefore, the relationship,

$$n_{cs} = n_{cs}(T_s) \tag{A.13}$$

can be considered known. One additional relationship would comprise the necessary nine equations for the nine unknowns. This equation is obtained by constructing a complete energy balance on the ash particle as,

$$4\pi r^2\left\{\left[\frac{n_b v_b}{4}\left(\frac{3}{2}kT_b\right)-\frac{n_s v_s}{4}\left(\frac{3}{2}kT_s\right)\right]+\left[\frac{n_b v_b}{4}-\frac{n_s v_s}{4}e^{\frac{\phi}{kT_s}}\right]m_c L\right\}=0. \tag{A.14}$$

Equation (A.6) through (A.14) constitute nine algebraic equations with nine unknowns. These equations are solved and the following equations are obtained for the particle growth rate,

$$\dot{r}=\frac{12}{5}\frac{K_n P_{sat}(T_g)}{\rho_l\sqrt{2\pi R_v T_g}}f\left[S-\sqrt{\frac{T_g}{T_s}}\frac{P_{sat}(T_s)}{P_{sat}(T_g)}e^{\frac{\phi}{kT_s}}\right], \tag{A.15}$$

where

$$T_s = T_g\left[1+\frac{fP_{sat}L(S-e^{\frac{\phi}{kT_s}})}{\frac{25}{8}P_g T_g g\sqrt{R_v R_g}+fP_{sat}Le^{\frac{\phi}{kT_s}}(\frac{L}{R_v T_g}-\frac{\phi}{kT_g}-\frac{1}{2})}\right]. \tag{A.16}$$

The two functions of the Knudsen number, f and g are defined as,

$$f=\frac{1+K_n}{1+\frac{15}{2}K_n(1+K_n)}, \tag{A.17}$$

and

$$g=\frac{1+K_n}{1+15(\frac{\gamma-1}{\gamma+1})K_n(1+K_n)}, \tag{A.18}$$

The supersaturation ratio, S, is defined as,

$$S = \frac{P_v(T_g)}{P_{sat}(T_g)}.$$

In deriving Eq.(A.15), the number densities are replaced by appropriate partial pressures via equation of state of gas. The energy function ϕ is defined as

$$\phi = \frac{2\sigma m_c}{\rho_l r}. \tag{A.19}$$

Homogeneous Nucleation

Collisions and the attendant cohesions of the monomers are considered to cause nucleation. Zeldovich formulated the equation for the nucleation rate:[53,54]

$$J = \beta(4\pi r^2) Z C_1 \exp(-\frac{\Delta G_n^*}{kT_g}) \tag{A.20}$$

C_1 is the concentration of the monomer, and G_n^* is the Gibbs free energy function for the formation of n-mers with the radius r^*. Z is the Zeldovich factor. The critical radius r^* is given by the Gibbs-Thompson relationship:

$$r^* = \frac{2\sigma\hat{v}}{kT_g \ln S} \tag{A.21}$$

Finally, the rate of nucleation is

$$J = \sqrt{\frac{2}{\pi}}\left(\frac{P_v}{kT_g}\right)^2 \hat{v}\sqrt{\frac{\sigma}{m_c}} \exp\left(-\frac{4\pi r^{*2}\sigma}{kT_g}\right) \tag{A.22}$$

With the expressions for $\dot{r}$ and J, Eq.(A.1) and Eq.(A.2) can be solved numerically. The boundary conditions are:

$$n(r,t) = n(r,0), \quad \text{and} \quad P_v(T_g,t) = P_v(T_g,0) \tag{A.23}$$

and at $r=r_0$

$$n(r_0,t) = 0. \tag{A.24}$$

The initial condition is given by Nukiyama-Tanasawa

$$n(0,r) = 130.2\frac{N_0}{\bar{r}}\left(\frac{r}{\bar{r}}\right)^4 e^{-\frac{5r}{\bar{r}}} \tag{A.25}$$

Numerical Solutions for MHD system

The numerical calculation was carried out for two different ash carryovers. The first is 10% ash carryover and the second is 50%. Figures (2-10) in his paper are comparison of effects of ash carryover for (1) supersaturation ratio and nucleation rate through channel; (2) evolution of the droplet size distribution; and (3) the average droplet radius and total density, for 10% and 50% ash carryover. The average particle radius is defined by

$$\bar{r}(x) = \frac{1}{N_0}\int_{r_0}^{\infty} rn(x,r)dr \tag{A.26}$$

The total number density is

$$N(x) = \int_{r_0}^{\infty} n(x,r)dr \tag{A.27}$$

The numerical solutions show that the evolution of the droplet size distribution proceeds through a succession of rather delicate balances between the size dependent condensation evaporation rate and nucleation rates. These balances are largely dictated by the amount of ash carryover and the supersaturation ratio. Evaporation and or growth at an early stage of the submicron size droplets and the subsequent nucleation of the extremely small droplets engender a bimodal size distribution either in the channel or in the diffuser, depending on the supersaturation ratio. Calculations indicates that bimodal nature is preserved at least through the diffuser.

At the CFFF, ash carryover is approximately 50%. Measurements of the particle size distribution was performed at the secondary combustor and the inlet of the BH and ESP. Figure (A.2) is the experimental measurement at the inlet of the BH and the ESP by Insitec. and clearly shows the bimodal distribution. Thus, the tests at the CFFF indicate that this bimodal PSD occurs and remains at the inlet of the BH and the ESP.

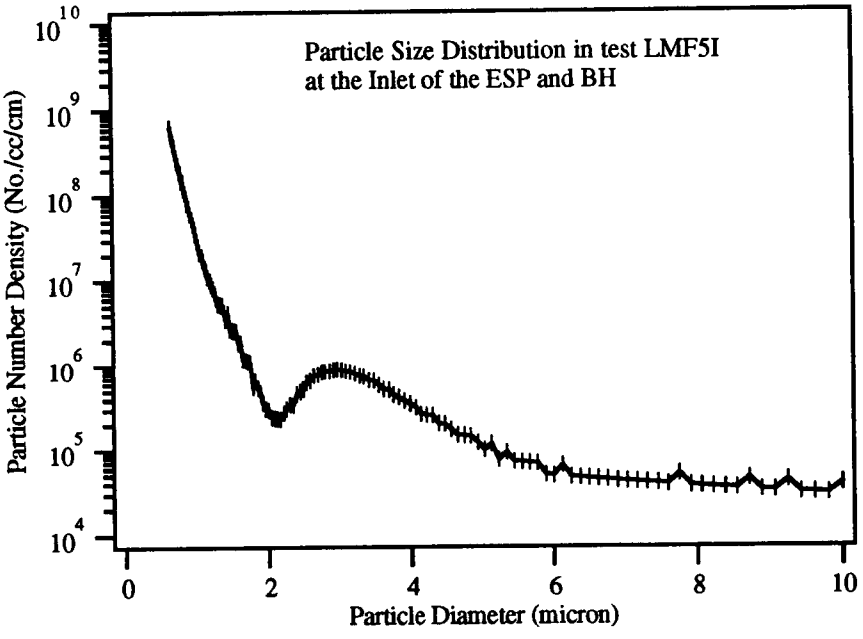


Figure A.2 Measured PSD at the ESP and BH Inlet by Insitec

Im's theory shows a bimodal distribution that is consistent with measurements at the CFFF, however, the measured PSD is very different from the Im's prediction due to the many differences, i.e., coal-loading, flow velocity, and actual vs. theoretical MHD channel and flow train structure. In this dissertation, two empirical formulas are used as the initial particle size distributions based on the measurement at the outlet of the secondary combustor. These formulas assume the distribution to be log-normal.

$$n(r) = \frac{n_0}{\sqrt{2\pi}r\sigma}\exp(-\frac{(\ln r + a)^2}{2\sigma^2}) \tag{A.28}$$

For curve 1 (left peak):

$$n_0 = 1\times10^8 / cc,\ \ \sigma = 0.18,\ \ a = 15.85,\qquad r < 0.28\mu m.$$

For curve 2 (right peak):

$$n_0 = 1\times10^5 / cc,\ \ \sigma = 0.30,\ \ a = 14.65,\qquad r \geq 0.28\mu m.$$

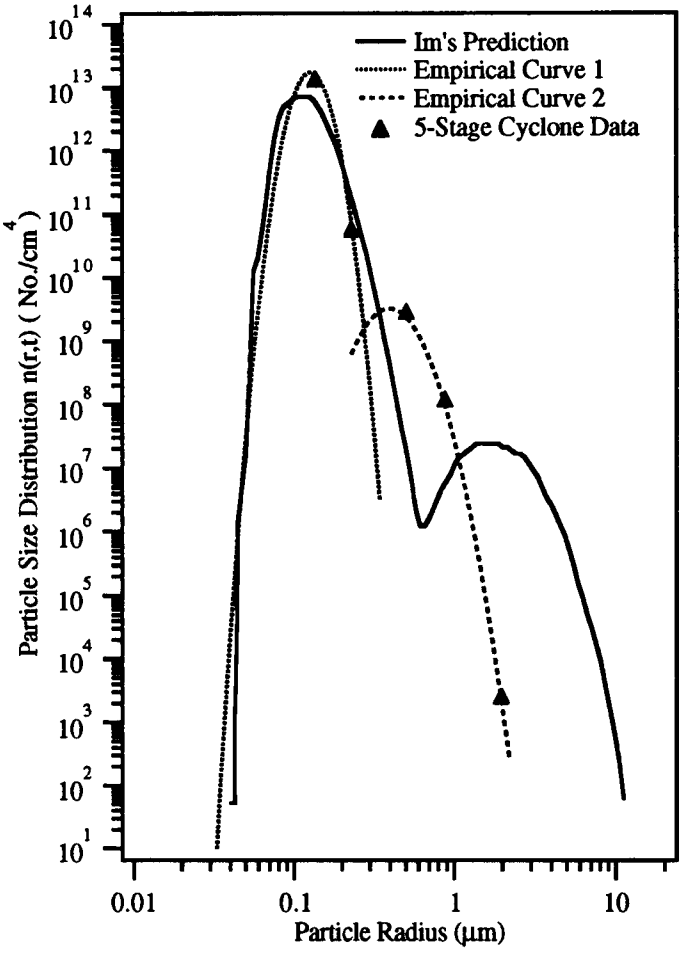


Figure A.3 Im's Prediction and 5-stage Cyclone Measurement at the Outlet of the Secondary Combustor

APPENDIX B THERMOPHORESIS

Small particles suspended in a gas in which there is a temperature gradient experience thermophoretic force which drives them towards a lower temperature region. The thermophoretic force has been studied for years[55,56,57,58,59,60,61] and is known as primarily being proportional to local temperature gradient. In our system the temperature gradient is established between the low and high temperature particles in a very small region around the lower temperature particles which are normally larger. Because of this temperature gradient, higher temperature and small particles will be pulled to the lower temperature and larger particles.

The thermophoretic force also depends on the Knudsen number, as

$$K_n = \frac{\lambda}{r}. \tag{B.1}$$

where λ is mean free path and r is the dimension of particle. At different region of K_n, there are different theories. In our system, the Knudsen number is larger than one because small particles are studied. The particle size is from 0.01 micron to 0.5 micron. The mean free path is usually at micron range. At this Knudsen number, the thermophoretic force is given by Waldmann[56] as

$$F_t = -2\pi r \mu_g \frac{r^2}{\lambda} \frac{\nabla T}{T_0}. \tag{B.2}$$

where ν is the kinematic viscosity of the gas. μ_g is the viscosity of the gas and r is the radius of the particle. When the Knudsen number is less than one, flow is nearly continuous and thermophoretic force is first investigated by J.R. Brock[55] and he gave

$$F_t = \frac{-12\pi\nu\mu_g r C_s (\frac{k_g}{k_p} + C_t \frac{\lambda}{r}) \frac{\nabla T}{T_0}}{(1+3C_m \frac{\lambda}{r})(1+2\frac{k_g}{k_p}+2C_t \frac{\lambda}{r})}. \qquad \text{(B.3)}$$

Where the C_t is defined as the temperature jump coefficient, C_m as the momentum exchange coefficient and C_s as the thermal slip coefficient. The C_t, C_m and C_s are determined by kinetic theory and are of order of unity.[62] The thermophoretic force is constant over this Knudsen number region when system is determined.

In our case, Brock's formula is used to calculate thermophoretic velocity although this formula is good for small Knudsen number. Note that when Knudsen number goes to infinity, Eq.(B.3) reduces to Eq.(B.2), except for the factor C_s / C_m=1.03 and hence, only three percent deviation is introduced by using Eq.(B.3). This has been pointed out by Talbot et al.[63]

Assuming that there are only thermophoretic and drag forces in the system, the thermophoretic velocity for the entire range of the Knudsen number is obtained by equating thermophoretic force to the Milikan drag force F_v.

$$F_t = -F_v. \qquad \text{(B.4)}$$

Where

$$F_v = \frac{6\pi\mu_g r U_t}{1+\frac{\lambda}{r}(a'+b'e^{-c'\frac{r}{\lambda}})}. \tag{B.5}$$

Then the thermophoretic velocity is

$$U_t = \frac{-2\nu C_s(\frac{k_g}{k_p}+C_t\frac{\lambda}{r})(1+\frac{\lambda}{r}(a'+b'e^{-c'\frac{r}{\lambda}}))\frac{\nabla T}{T_0}}{(1+3C_m\frac{\lambda}{r})(1+2\frac{k_g}{k_p}+2C_t\frac{\lambda}{r})}. \tag{B.6}$$

Where

a'=1.2

b'=0.41

c'=0.88

C_m=1.14

C_s=1.17

C_t=2.18.

Eq.(B.6) can be also written as

$$U_t = -f(\frac{\lambda}{r})\frac{\nabla T}{T_0}. \tag{B.7}$$

where

$$f(\frac{\lambda}{r}) = \frac{2\nu C_s(\frac{k_g}{k_p}+C_t\frac{\lambda}{r})(1+\frac{\lambda}{r}(a'+b'e^{-c'\frac{r}{\lambda}}))}{(1+3C_m\frac{\lambda}{r})(1+2\frac{k_g}{k_p}+2C_t\frac{\lambda}{r})}. \tag{B.8}$$

When the temperature gradient exists between particles, U_t is in the direction of decreasing temperature and is proportional to the local temperature gradient like the thermophoretic force.

In this dissertation, the temperature gradient can be approximately expressed as

$$\frac{\nabla T}{T_0} = \frac{T_f - T_p}{T_0} \times \frac{1}{r}. \tag{B.9}$$

and the temperature of a particle, T_p, is obtained by Eq.(2.2.1.14).

From Figure (B.1), it can be seen that the function f is not sensitive to particle size. So the local temperature gradient may be an important factor.

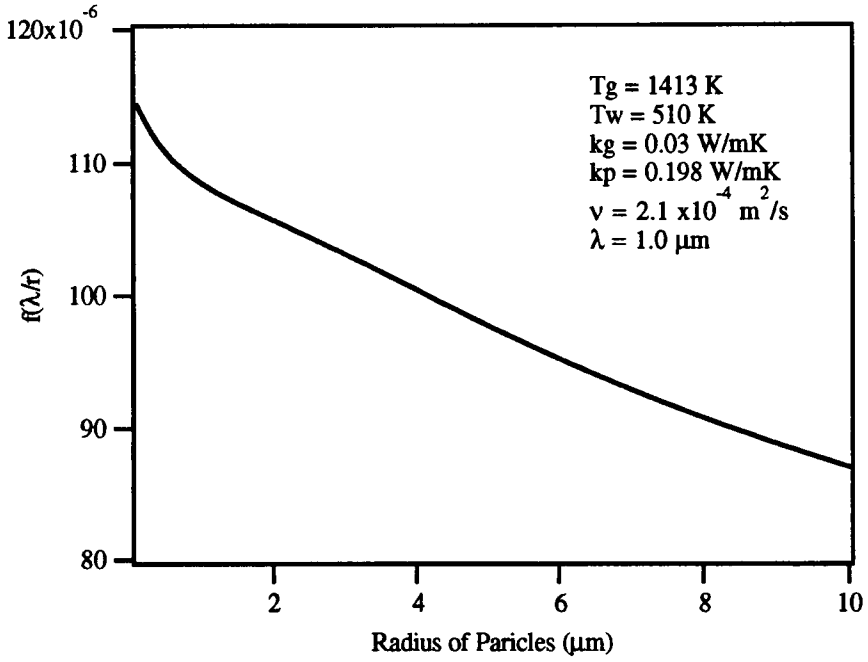


Figure B.1 f(λ/r) vs. Radius of Particle

From Figure (B.2), it is obvious that thermophoretic velocity strongly depends on particle size. Smaller particles have larger velocities because smaller particles have relatively larger local temperature gradients and smaller masses.

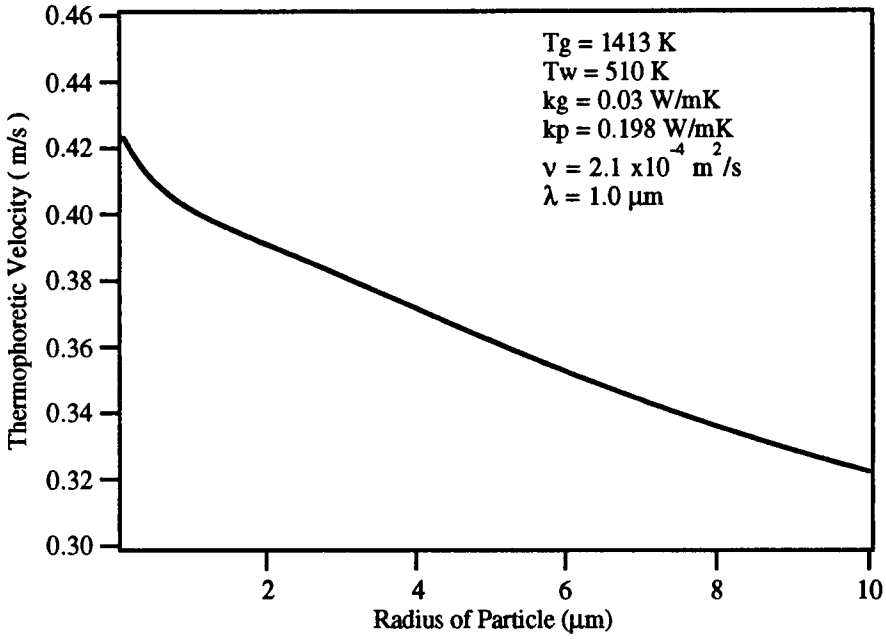


Figure B.2 Thermophoretic Velocity

APPENDIX C THERMAL FORCE BETWEEN TWO PARTICLES

With reference to Figure (C.1), the equation of motion for each sphere can be expressed as follows:

$$m_1 \frac{d^2\vec{x}_1}{dt^2} = \vec{F}_1 - 6\pi\mu a_1 (\frac{d\vec{x}_1}{dt} - \vec{u}(\vec{x}_1)) \tag{C.1}$$

$$m_2 \frac{d^2\vec{x}_2}{dt^2} = \vec{F}_2 - 6\pi\mu a_2 (\frac{d\vec{x}_2}{dt} - \vec{u}(\vec{x}_2)). \tag{C.2}$$

Where the first term of the right hand side of these equations ($\vec{F}_1$ & $\vec{F}_2$) represents the thermophoretic force, which is along the line of centers of the spheres, and the second term represents the drag force. The quantity $\vec{u}(\vec{x}_1)$ *and* $\vec{u}(\vec{x}_2)$ denote the fluid velocities at the positions $\vec{x}_1$ and $\vec{x}_2$, respectively. For simplicity, Stokesian flow has been assumed.

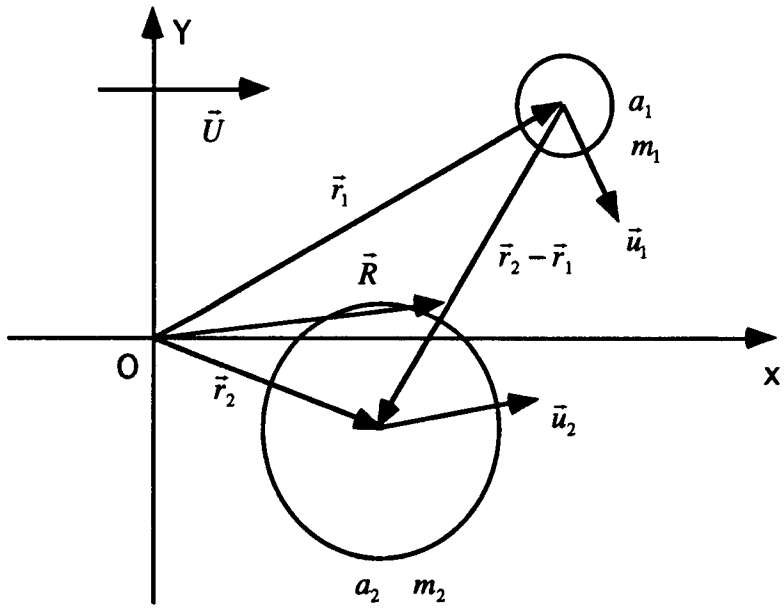


Figure C.1 Interaction of Two Spherical Particles

Transforming to center-of-mass and relative coordinates using the relationship

$$\vec{R} = \frac{m_1\vec{x}_1 + m_2\vec{x}_2}{m_1 + m_2} \qquad and \qquad \vec{r} = \vec{r}_1 - \vec{r}_2. \tag{C.3}$$

and assuming the fluid velocity to be a constant, U, one can obtain the following equations:

$$m\frac{d^2\vec{r}}{dt^2} = (\frac{m}{m_1}\vec{F}_1 - \frac{m}{m_2}\vec{F}_2) - 6\pi\mu m\left\{(\frac{a_1}{m_1} - \frac{a_2}{m_2})\frac{d\vec{R}}{dt} + m(\frac{a_1}{m_1^2} - \frac{a_2}{m_2^2})\frac{d\vec{r}}{dt}\right\} - 6\pi\mu m\vec{u}(\frac{a_1}{m_1} + \frac{a_2}{m_2}) \tag{C.4}$$

$$m\frac{d^2\vec{R}}{dt^2} = \frac{m}{m_1 + m_2}(\vec{F}_1 + \vec{F}_2) - \frac{6\pi\mu m}{m_1 + m_2}\left\{(a_1 + a_2)\frac{d\vec{R}}{dt} + m(\frac{a_1}{m_1} - \frac{a_2}{m_2})\frac{d\vec{r}}{dt}\right\} - \frac{6\pi\mu m\vec{u}}{m_1 + m_2}(a_1 + a_2). \tag{C.5}$$

where $m=(m_1m_2)/(m_1+m_2)$, is defined as the reduced mass.

APPENDIX D TWO PARTICLE INTERACTION IN THERMOPHORESIS

Force applied on particles under temperature gradient has been studied in many practical applications.[64,65,66,67] The interaction of two particles by thermophoresis coupled with aerodynamic force is along the line of the centers of the two particles. These particles have different velocities.

Consider the thermophoretic motion of two spheres in a temperature gradient applied along their line of centers. In this dissertation, the temperature gradient is established by the particles. It is uniform and is the difference of temperatures of the particles divided by their separation distance. The bispherical coordinate system (ξ, η, ϕ) which is related to the cylindrical polar coordinate (r, ϕ, z) by the following relations

$$r = \frac{c \sin \eta}{\cosh \xi - \cos \eta}; z = \frac{c \sinh \xi}{\cosh \xi - \cos \eta}; \phi = \phi \tag{D.1}$$

is particularly convenient for studying two sphere bounded flows. In Figure (D.1), c is a scale factor for the bispherical system, ξ varies from -∞ to +∞ and defines nonconcentric spheres centered along the z-axis. The $\xi=\xi_0$ surface is a sphere of radius $c\ csch\xi_0$ with its center located at a distance h from the midplane where $h=c\ cosh\xi_0$, and the variable η ranges from 0 to π and defines a spindle-like surface of revolution about the z-axis. The metric coefficients of the bispherical system are given by

$$h_\xi = h_\eta = \frac{c}{\cosh \xi - \cos \eta}; h_\phi = \frac{c \sinh \xi}{\cosh \xi - \cos \eta}. \tag{D.2}$$

The coordinate system shown in Figure (D.1) is described by Morse and Feshbach.[68] Since Stokesian flow is assumed, the Navier-Stokes equation is justified and the differential equation governing this axisymmetric viscous fluid is given by[69]

$$D^4\psi = 0. \tag{D.3}$$

ψ is the Stokes' stream function and D^4 is a differential operator in bispherical coordinates given by

$$D^2 \equiv \frac{\cosh\xi - \mu}{c^2}\left\{\frac{\partial}{\partial\xi}\left[(\cosh\xi - \mu)\frac{\partial}{\partial\xi}\right] + (1-\mu^2)\frac{\partial}{\partial\mu}\left[(\cosh\xi - \mu)\frac{\partial}{\partial\mu}\right]\right\} \tag{D.4}$$

where μ is $cos\eta$.

Linearity of the governing equation and boundary conditions for the thermophoretic motion of two spheres along their line of centers permits the flow to be separated into three distinct cases. Consider first the case of two spheres translating along their line of centers, each having a frictional slip at its surface proportional to the local tangential shear stress in the fluid. The solution to this flow is obtained by superposing the case when the spheres have equal velocities along their line of centers with that of two spheres moving with equal and opposite velocities along their line of centers. These two cases were previously investigated by Reed and Morrison.[70] To these cases the fluid motion produced by two stationary spheres in a uniform temperature gradient is superposed and the spheres induced thermal creep velocities at their surfaces as well as frictional slip. These three flows when superimposed create a model of the fluid motions which would be observed with the thermophoresis of two spheres along their line of centers.

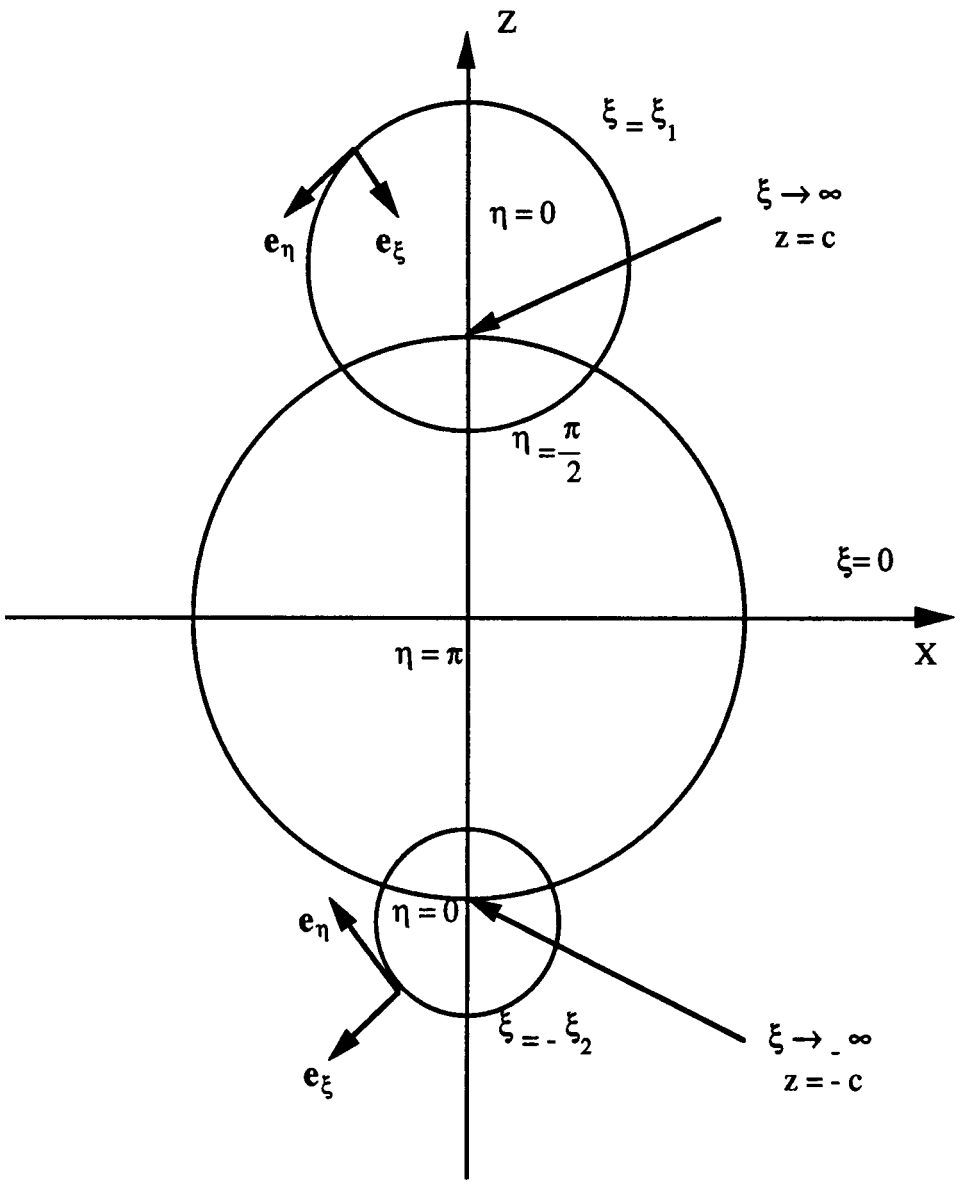


Figure D.1 Bispherical Coordinates

Division of the flow in this manner allows simplification of the boundary conditions. Because of prior analyses, one needs only analyze the fluid motion past stationary spheres. Impermeability of the aerosol particles requires that there be no normal fluid motion at their spherical boundary so that

$$v_\xi = 0; \quad \text{at} \quad \xi = \xi_1, -\xi_2. \tag{D.5}$$

The thermal creep and frictional slip velocities along the particle surfaces yield

$$v_\eta = \frac{3\kappa}{4\rho T}\left(\nabla T_f\right)_\eta \pm C_{m1,2}\frac{\lambda}{\kappa}\sigma_{\xi\eta}; \qquad at \qquad \xi = \xi_1, -\xi_2 \tag{D.6}$$

where $(\nabla T_f)_\eta$ is the tangential component of the temperature gradient in the fluid and $\sigma_{\xi\eta}$ is the tangential stress component evaluated at the particle surfaces. The upper sign here refers to positive values of ξ and the lower to negative ξ values. It is this boundary condition that provides the coupling between the temperature gradient and the fluid motions that result.

The differential equation governing the steady-state energy equation is the Laplace equation written for the fluid and each particles.

$$\nabla^2 T_f = 0; \quad \nabla^2 T_1 = 0; \quad \nabla^2 T_2 = 0. \tag{D.7}$$

where T_f is the fluid temperature, T_1 the temperature within sphere 1 and T_2 the temperature inside sphere 2.

When this analysis is applied to slip-flow regime, it is necessary to use temperature-jump condition in matching conditions. The phenomenon of the temperature-jump in rarefied

gases is well known and has been confirmed by experimentation.[71,72,73] Two conditions are imposed at each particle-gas interface. The rate of energy transferred across the interface must be continuous.

$$k_f\left(\nabla T_f\right)_\xi = k_{1,2}\left(\nabla T_{1,2}\right)_\xi; \qquad at \qquad \xi = \xi_1, -\xi_2 \tag{D.8}$$

where $(\nabla T_f)_\xi$ represents the normal component of the temperature gradient at the surface. Furthermore, at low Knudsen numbers, a temperature jump at the gas-solid interface proportional to the normal component of the temperature gradient in the gas is present.

$$T_f - T_{1,2} = \pm C_t\left(\nabla T_f\right)_\xi; \qquad \text{at} \qquad \xi = \xi_1, -\xi_2 \tag{D.9}$$

Finally, the fluid temperature must approach that of the uniformly applied gradient far from the particles.

$$T_f \to gz \qquad as \qquad r \to \infty. \tag{D.10}$$

In this problem, g is assumed to be approximate temperature difference of these two particles, such as

$$g \propto \frac{T_1 - T_2}{\text{separation distance}}, \qquad \text{if} \quad T_1 > T_2. \tag{D.11}$$

The solution to Laplace's equation is effected through straightforward application of the method of separation of variables. Sufficiently general solutions are given by

$$T_f = gc(\cosh\xi - \mu)^{\frac{1}{2}} \sum_{n=0}^{\infty} \left[A_n \sinh(n+\frac{1}{2})\xi + B_n \cosh(n+\frac{1}{2})\xi \right] P_n(\mu) + gz \tag{D.12}$$

$$T_1 = gc(\cosh\xi - \mu)^{\frac{1}{2}} \sum_{n=0}^{\infty} C_n e^{-(n+\frac{1}{2})\xi} P_n(\mu) \tag{D.13}$$

and

$$T_2 = gc(\cosh\xi - \mu)^{\frac{1}{2}} \sum_{n=0}^{\infty} D_n e^{-(n+\frac{1}{2})\xi} P_n(\mu) \tag{D.14}$$

where P_n are the Legendre polynomials of degree n and order zero. Application of the boundary conditions at each sphere yields four recursion relations that 4N unknowns, A_n, B_n, C_n and D_n, which must satisfy.

$$\begin{aligned}
&A_n\left\{n\cosh(n-\tfrac{1}{2})\xi + (n+1)\cosh(n+\tfrac{3}{2})\xi\right\} - A_{n-1}n\cosh(n-\tfrac{1}{2})\xi - A_{n+1}(n+1)\cosh(n+\tfrac{3}{2})\xi \\
&+B_n\left\{n\sinh(n-\tfrac{1}{2})\xi - (n+1)\sinh(n+\tfrac{3}{2})\xi\right\} + B_{n-1}n\sinh(n-\tfrac{1}{2})\xi + B_{n+1}(n+1)\sinh(n+\tfrac{3}{2})\xi \\
&-\frac{k_2}{k_f}\left\{nD_{n-1}e^{-(n-\frac{1}{2})\xi} + (n+1)D_{n+1}e^{-(n-\frac{3}{2})\xi} - nD_n e^{-(n-\frac{1}{2})\xi} - nD_n e^{-(n-\frac{3}{2})\xi}\right\} \\
&= 2\sqrt{2}e^{-(n+\frac{1}{2})\xi}\left\{(2n+1)\sinh\xi - \cosh\xi\right\}; \qquad \text{at} \quad \xi = \xi_2
\end{aligned} \tag{D.15}$$

$$\begin{aligned}
&A_n\left\{n\cosh(n-\tfrac{1}{2})\xi + (n+1)\cosh(n+\tfrac{3}{2})\xi\right\} - A_{n-1}n\cosh(n-\tfrac{1}{2})\xi - A_{n+1}(n+1)\cosh(n+\tfrac{3}{2})\xi \\
&+B_n\left\{n\sinh(n-\tfrac{1}{2})\xi - (n+1)\sinh(n+\tfrac{3}{2})\xi\right\} + B_{n-1}n\sinh(n-\tfrac{1}{2})\xi + B_{n+1}(n+1)\sinh(n+\tfrac{3}{2})\xi \\
&-\frac{k_2}{k_f}\left\{nC_{n-1}e^{-(n-\frac{1}{2})\xi} + (n+1)C_{n+1}e^{-(n-\frac{3}{2})\xi} - nC_n e^{-(n-\frac{1}{2})\xi} - nC_n e^{-(n-\frac{3}{2})\xi}\right\} \\
&= 2\sqrt{2}e^{-(n+\frac{1}{2})\xi}\left\{(2n+1)\sinh\xi - \cosh\xi\right\}; \qquad \text{at} \quad \xi = \xi_1
\end{aligned} \tag{D.16}$$

$$c_i\frac{\lambda}{c}\begin{Bmatrix}A_n\{n\cosh(n-\frac{1}{2})\xi+(n+1)\cosh(n+\frac{3}{2})\xi\}\\-A_{n-1}n\cosh(n-\frac{1}{2})\xi-A_{n+1}(n+1)\cosh(n+\frac{3}{2})\xi\end{Bmatrix}+2A_n\cosh(n+\tfrac{1}{2})\xi$$

$$+c_i\frac{\lambda}{c}\begin{Bmatrix}B_n\{n\sinh(n-\frac{1}{2})\xi+(n+1)\sinh(n+\frac{3}{2})\xi\}\\-B_{n-1}n\sinh(n-\frac{1}{2})\xi-B_{n+1}(n+1)\sinh(n+\frac{3}{2})\xi\end{Bmatrix}+2B_n\sinh(n+\tfrac{1}{2})\xi-2D_ne^{-(n-\frac{1}{2})\xi}$$

$$=2\sqrt{2}e^{-(n+\frac{1}{2})\xi}\{(2n+1)(c_i\tfrac{\lambda}{c}\sinh\xi-1)-c_i\tfrac{\lambda}{c}\cosh\xi\};\qquad \text{at}\quad \xi=\xi_2$$

(D.17)

$$c_i\frac{\lambda}{c}\begin{Bmatrix}A_n\{n\cosh(n-\frac{1}{2})\xi+(n+1)\cosh(n+\frac{3}{2})\xi\}\\-A_{n-1}n\cosh(n-\frac{1}{2})\xi-A_{n+1}(n+1)\cosh(n+\frac{3}{2})\xi\end{Bmatrix}+2A_n\sinh(n+\tfrac{1}{2})\xi$$

$$+c_i\frac{\lambda}{c}\begin{Bmatrix}B_n\{n\sinh(n-\frac{1}{2})\xi+(n+1)\sinh(n+\frac{3}{2})\xi\}\\-B_{n-1}n\sinh(n-\frac{1}{2})\xi-B_{n+1}(n+1)\sinh(n+\frac{3}{2})\xi\end{Bmatrix}+2B_n\cosh(n+\tfrac{1}{2})\xi-2C_ne^{-(n+\frac{1}{2})\xi}$$

$$=2\sqrt{2}e^{-(n+\frac{1}{2})\xi}\{(2n+1)(c_i\tfrac{\lambda}{c}\sinh\xi-1)-c_i\tfrac{\lambda}{c}\cosh\xi\};\qquad \text{at}\quad \xi=\xi_1$$

(D.18)

Solution of these equations is effected by choosing some large N, neglecting the N+1 terms and solving the remaining 4N equations for the 4N unknown coefficients.

Solution of the governing energy equation now permits examination of the fluid motion. A solution to Eq.(D.3) in bispherical coordinates was first presented by Stimson and Jeffery[74] who examined the slow viscous motion of two spheres along their line of centers in the zero Knudsen number limit. The solution is given by

$$\psi=(\cosh\xi-\mu)^{\frac{1}{2}}\sum_{n=0}^{\infty}W_nU_{n+1}^{-\frac{1}{2}}(\mu)\tag{D.19}$$

where

$$W_n=a_n\cosh(n-\frac{1}{2})\xi+b_n\sinh(n-\frac{1}{2})\xi+c_n\cosh(n+\frac{3}{2})\xi+d_n\cosh(n+\frac{3}{2})\xi.$$

(D.20)

$U_{n+1}^{\frac{1}{2}}(\mu)$ is known as the Gegenbauer or Ultraspherical polynomial of order *n+1* and degree *-(1/2)*.

Application of the boundary conditions (D.5) and (D.6) requires evaluation of the tangential component of the fluid stress at each particle surface. The shear stress simplifies considerably at each spherical surface due to the zero normal flow condition (D.5) imposed at the gas-solid interfaces. In terms of $W_n(\xi)$ and $U_{n+1}^{\frac{1}{2}}(\mu)$, the tangential fluid shear stress can be written

$$\sigma_{\xi\eta} = -\frac{\kappa(\cosh\xi-\mu)^{\frac{3}{2}}}{c^3\sin\eta}\sum_{n=1}^{\infty}\frac{d^2}{d\xi^2}W_n(\xi)U_{n+1}^{-\frac{1}{2}}(\mu); \qquad \text{at} \quad \xi=\xi_1,-\xi_2. \tag{D.21}$$

Using Eq.(D.21) and imposing the boundary conditions (D.5) and (D.6) produces four recursion relations of the 4N unknowns a_n, b_n, c_n and d_n.

$$\begin{aligned}
&\mp C_m\frac{\lambda}{c}\frac{n+1}{(2n+5)(2n+3)}\frac{4\rho T}{3\kappa g c^2}\frac{d^2}{d\xi^2}W_{n+2}(\xi)\pm C_m\frac{\lambda}{c}\frac{\cosh\xi}{(2n+3)}\frac{4\rho T}{3\kappa g c^2}\frac{d^2}{d\xi^2}W_{n+1}(\xi)\\
&+\frac{4\rho T}{3\kappa g c^2}\frac{d}{d\xi}W_{n+1}(\xi)\mp C_m\frac{\lambda}{c}\frac{1}{(2n-1)(2n+3)}\frac{4\rho T}{3\kappa g c^2}\frac{d^2}{d\xi^2}W_n(\xi)+\frac{4\rho T}{3\kappa g c^2}\frac{d}{d\xi}W_{n-1}(\xi)\\
&\mp C_m\frac{\lambda}{c}\frac{\cosh\xi}{(2n-1)}\frac{4\rho T}{3\kappa g c^2}\frac{d^2}{d\xi^2}W_{n-1}(\xi)\pm C_m\frac{\lambda}{c}\frac{n}{(2n-1)(2n-3)}\frac{4\rho T}{3\kappa g c^2}\frac{d^2}{d\xi^2}W_{n-2}(\xi)\\
&=-\gamma_{n+2}\frac{(n+2)(n+1)}{2(2n+3)}+\gamma_{n+1}\frac{(n+2)(n+1)}{(2n+3)}\cosh\xi-\gamma_n\frac{2n^2+2n+1}{(2n+3)(2n-1)}\\
&-\gamma_{n-1}\frac{n(n-1)}{(2n-1)}\cosh\xi+\gamma_{n-2}\frac{n(n-1)}{2(2n-1)}-2\sqrt{2}\sinh\xi e^{\mp(n+\frac{1}{2})\xi}\left\{\frac{n(n-1)}{2n-1}e^{\pm\xi}-\frac{(n+1)(n+2)}{2n+3}e^{\mp\xi}\right\}
\end{aligned} \tag{D.22}$$

where

$$\gamma_n = A_n\sinh(n+\frac{1}{2})\xi + B_n\cosh(n+\frac{1}{2})\xi. \tag{D.23}$$

In the Eq.(D.22), it is assumed that $C_{m1}=C_{m2}$ for simplicity. The upper sign corresponds to sphere 1 while the lower sign corresponds to sphere 2.

The zero normal flow boundary condition requires

$$W_n(\xi)=0, \quad \text{at} \quad \xi=\xi_1;-\xi_2 \tag{D.24}$$

Integration of the fluid stress components in the z-direction over each particle surface yields the force exerted by the fluid on the spheres. Stimson and Jeffery[74] presented a general equation for the force on an axisymmetric body in steady low Reynolds number motion. The thermal contribution to the force on the particle surfaces may be written as

$$F_{1,2}=\frac{9\pi\kappa^2 a_{1,2} g}{\rho T}\left(\frac{1}{1+c_m\frac{\lambda}{a_{1,2}}}\right)\left(\frac{1+\frac{k}{k_f}c_m\frac{\lambda}{a_{1,2}}}{\frac{k}{k_f}+2\frac{k}{k_f}c_m\frac{\lambda}{a_{1,2}}+2}\right)\Phi_{1,2} \tag{D.25}$$

where

$$\Phi_{1,2}=\left(1+c_m\frac{\lambda}{a_{1,2}}\right)\left(\frac{\frac{k}{k_f}+2\frac{k}{k_f}c_m\frac{\lambda}{a_{1,2}}+2}{1+\frac{k}{k_f}c_m\frac{\lambda}{a_{1,2}}}\right)\frac{\sinh\xi}{3\sqrt{2}}\sum_{n=1}^{\infty}G_{n1,2} \tag{D.26}$$

and

$$G_{n1,2}=\frac{4\rho T}{3\kappa g c^2}(a_n\pm b_n+c_n\pm d_n). \tag{D.27}$$

Eq. (D.25) gives the thermophoretic force applied on either sphere. However, since temperatures of spheres in the flow are different among different size particles and there are not any external temperature gradients, this thermophoresis problem can be viewed differently. The thermophoretic force is not constant but decreases exponentially with respect to the separation distance between two spheres since the temperature gradient, which is the primary factor inducing thermophoresis, is established by the spheres and

depends on their separation distance. In this dissertation, the classical thermophoresis theory is used. A new theory would require further research.[75]

APPENDIX E DERIVATION OF RATE OF PARTICLE GROWTH

At the CFFF, the mean free path in each section is on the order of 1.0μm. This means that for particles of about one micron the question of the applicability of the diffusion approximation is of paramount importance. Although the Knudsen number is small, the diffusion approximation can not be regarded as sufficiently rigorous and when using this approximation it is necessary to make a correction for the rate of growth by condensation.

The method of the boundary sphere is used to analyze this rate of the growth. This has been used by K.H. Im et. al. (Appendix A). Here, derivation of Im's particle growth rate is given to describe the growth by condensation after the secondary combustor at the CFFF. At this location, the flow temperature is about 1400 K - 1600 K and K_2SO_4 and K_2CO_3 is in gas phase, condensed phase and solid phase. K_2SO_4 and K_2CO_3 vapor condense on existing nuclei rather than nucleating homogeneously, which produces a huge number of fine particles. The final formula is slightly different from Eq.(A.15) since there were a few mistakes in Im's paper.

Starting with Eq.(A.6), if the evaporation coefficient, α_c, is taken into account, the mass balance equation at layer b, Eq. (A.6), can be rewritten as

$$4\pi(r+\lambda)D_v(n_{c\infty}-n_{cb}) = 4\pi r^2\alpha_c\left[\frac{n_{cb}v_{cb}}{4} - \frac{n_{cs}v_{cs}}{4}e^{\frac{\phi}{kT_s}}\right] \qquad \text{(E.1)}$$

where n_{Cb}, n_{Cs}, $n_{C\infty}$ are the vapor densities at b, s, and free stream, which can be expressed as:

$$n_{cb} = \frac{p_{sat}(T_b)}{kT_b}, \qquad n_{cs} = \frac{p_{sat}(T_s)}{kT_s}, \qquad \text{and} \quad n_{c\infty} = \frac{p_v(T_g)}{kT_g}. \tag{E.2}$$

From Eq.(E.1) one can solve

$$n_{cb}v_{cb} = \frac{\alpha_c n_{cb} v_{cb} e^{\frac{\phi}{kT_s}} + (Kn+1)\frac{4D_v n_{c\infty}}{r}}{\alpha_c + (Kn+1)\frac{4D_v}{r}} \tag{E.3}$$

From Eqs.(A.3-5) with evaporation coefficient, α_C, and Eq.(E.3), the mass flux becomes

$$\dot{m} = m_c(I_+ - I_-) = (4\pi r D_v) m_c f \left(n_{c\infty} - n_{cs}\frac{v_{cs}}{v_{cb}} e^{\frac{\phi}{kT_s}} \right) \tag{E.4}$$

where

$$f = \frac{k_n + 1}{1 + (k_n+1)\frac{4D_v}{v_{cb} r \alpha_c}}. \tag{E.5}$$

Substitution of Eq.(E.2) with

$$v_{cb} = \sqrt{\frac{8kT_b}{\pi m_c}}, \quad \text{and} \quad v_{cs} = \sqrt{\frac{8kT_s}{\pi m_c}}. \tag{E.6}$$

gives the rate of particle growth by

$$\dot{r} = \frac{\dot{m}}{4\pi r^2 \rho} = \frac{D_v}{r\rho} f \frac{p_{sat}(T_g)}{R_v T_g} \left(S - \frac{p_{sat}(T_s)}{p_{sat}(T_g)} \left(\frac{T_g}{T_b}\right)^{\frac{1}{2}} \left(\frac{T_g}{T_s}\right)^{\frac{1}{2}} e^{\frac{\phi}{kT_s}} \right) \tag{E.7}$$

where

$$S = \frac{p_v(T_g)}{p_{sat}(T_g)} \quad \text{and} \quad R_v = \frac{k}{m_c}. \tag{E.8}$$

One can see from Eqs.(E.7) and (E.8) that the rate of particle growth is a function of T_S. Now one needs to find T_S by constructing energy balances at the layer b and at the surface of the particle.

At the layer b, the energy balance is

$$4\pi(r+\lambda)K(T_g - T_b) = 4\pi r^2\left[\frac{n_b v_b}{4}(\frac{3}{2}kT_b + \hat{c}_v T_b) - \frac{n_s v_s}{4}(\frac{3}{2}kT_s + \hat{c}_v T_s)\right] \tag{E.9}$$

where

$$c_v = \hat{c}_v \cdot N_A \quad \text{and} \quad c_v = \frac{R_g}{\gamma - 1} \tag{E.10}$$

where N_A is Avogadro's number and R_g is the gas constant. For an ideal gas,

$$\frac{3}{2}kT + \hat{c}_v T = \frac{3}{2}kT + \frac{R_g}{(\gamma-1)N_A}T = \frac{3}{2}kT + \frac{k}{(\gamma-1)}T = \frac{3\gamma-1}{2(\gamma-1)}kT \tag{E.11}$$

with $R_g = kN_A$. The Eq.(E.9) can be rewritten as

$$\frac{K}{r}(K_n+1)(T_g - T_b) = \frac{n_g v_g}{4}\frac{k}{2}(\frac{3\gamma-1}{\gamma-1})(T_b - T_s) \tag{E.12}$$

with an assumption $n_b v_b = n_s v_s = n_g v_g$. After several algebraic manipulations,

$$\frac{T_b - T_g}{T_s - T_g} = \frac{g}{K_n + 1} \tag{E.13}$$

where

$$\frac{1}{g}=\frac{1}{K_n+1}+\frac{\frac{K}{r}}{\frac{n_g v_g}{4}(\frac{3\gamma-1}{\gamma-1})\frac{k}{2}} \tag{E.14}$$

Then the heat flux towards the sphere is

$$\dot{q}"=4\pi rgK(T_s-T_g) \tag{E.15}$$

At the surface of the sphere,

$$4\pi r^2\left[\frac{n_b v_b}{4}(\frac{3}{2}kT_b+\hat{c}_v T_b)-\frac{n_s v_s}{4}(\frac{3}{2}kT_s+\hat{c}_v T_s)+\alpha_c\left(\frac{n_{cb}v_{cb}}{4}-\frac{n_{cs}v_{cs}}{4}e^{\frac{\phi}{kT_s}}\right)m_c L_c\right]=0 \tag{E.16}$$

Use of Eq.(E.1) and Eq.(E.15) gives

$$4\pi rKg(T_s-T_g)=\dot{m}L_c. \tag{E.17}$$

where L_C is the heat of evaporation. From Eq.(E.17), one can obtain

$$T_s-T_g=\frac{1}{g}\frac{\dot{m}}{4\pi r}\frac{L_c}{K}. \tag{E.18}$$

In the free molecular regime, $K_n\to\infty$, it can be seen from Eq.(E.13) that $T_b\to T_g$, It is assumed that T_b is negligibly different from T_g. As presented, the equation for $\dot{r}$ and T_S are coupled, requiring an iterative solution. These can be decoupled in the useful limit of a small temperature difference between T_S and T_g. Let $\Delta T=T_s-T_g<<1$. One can have

$$\left(\frac{T_g}{T_s}\right)^{\frac{1}{2}}=1-\frac{1}{2}(\frac{\Delta T}{T_g}) \tag{E.19}$$

$$\exp(\frac{\phi}{kT_s}) = \exp\left[\frac{\phi}{kT_g}(1-\frac{\Delta T}{T_g})\right]$$
$$= \exp(\frac{\phi}{kT_g})\exp(-\frac{\phi}{kT_g}\frac{\Delta T}{T_g}) = \left(1-\frac{\phi}{kT_g}\frac{\Delta T}{T_g}\right)\exp(\frac{\phi}{kT_g}) \quad \text{(E.20)}$$

For small ΔT, one can apply Clapeyron equation[76] to obtain

$$\frac{p_{sat}(T_s)}{p_{sat}(T_g)} = 1+\left(\frac{L_c}{R_c T_g}\right)\frac{\Delta T}{T_g} \quad \text{(E.21)}$$

With Eqs.(E.19-21), Eq.(E.4) can be expressed as

$$\dot{m} = m_c(I_+ - I_-)$$
$$= (4\pi r D_v) f \frac{p_{sat}(T_g)}{R_v T_g}\left\{S-\left[1+\left(\frac{L_c}{R_v T_g}-\frac{\phi}{kT_g}-\frac{1}{2}\right)\frac{\Delta T}{T_g}\right]e^{\frac{\phi}{kT_g}}\right\} \quad \text{(E.22)}$$

Combining Eq.(E.22) and Eq.(E.18) gives

$$\frac{\Delta T}{T_g} = \frac{fL_c p_{sat}(T_g)(S-e^{\frac{\phi}{kT_g}})}{\frac{K}{D_v}gR_v T_g^2 + fL_c p_{sat}(T_g)\left(\frac{L_c}{R_v T_g}-\frac{\phi}{kT_g}-\frac{1}{2}\right)e^{\frac{\phi}{kT_g}}} \quad \text{(E.23)}$$

Hence, T_S can be solved using Eq.(E.23) and the growth rate can be obtained. According to kinetic theory,[77] the gas conductivity, K, can be expressed as

$$K = \frac{15}{8}kn_\infty r\sqrt{\frac{8kT_g}{\pi m}}K_n, \quad \text{(E.24)}$$

and also diffusivity, D_v, as

$$D_v = \frac{3}{5} r \sqrt{\frac{8kT_g}{\pi m_c}} K_n, \tag{E.25}$$

With these expressions, one can finally obtain

$$\dot{r} = \frac{12}{5} \frac{p_{sat}(T_g)}{\rho\sqrt{2\pi R_v T_g}} K_n f \left(S - \frac{p_{sat}(T_s)}{p_{sat}(T_g)} \left(\frac{T_g}{T_s}\right)^{\frac{1}{2}} e^{\frac{\phi}{kT_s}} \right) \tag{E.25}$$

and

$$T_s = T_g \left\{ 1 + \frac{f L_c p_{sat}(T_g)(S - e^{\frac{\phi}{kT_s}})}{\frac{25}{8} p g T_g \sqrt{R_v R_g} + f L_c p_{sat}(T_g) \left(\frac{L_c}{R_v T_g} - \frac{\phi}{kT_g} - \frac{1}{2} \right) e^{\frac{\phi}{kT_s}}} \right\} \tag{E.26}$$

with

$$f = \frac{K_n + 1}{1 + \frac{12}{5\alpha_c}(K_n + 1)} \tag{E.27}$$

$$g = \frac{K_n + 1}{1 + 15\left(\frac{3\gamma - 1}{\gamma - 1}\right)(K_n + 1)}. \tag{E.28}$$

APPENDIX F NUCLEATION

When the pressure of a vapor p is less than, equal to, or greater than the vapor pressure of the liquid phase p_∞ at the same temperature, the vapor is described as undersaturated, saturated, or supersaturated with respect to the liquid phase. While the undersaturated state and saturated state are thermodynamically stable, the supersaturated state is unstable; i.e., a supersaturated vapor in contact with the bulk liquid phase will condense onto the liquid until saturation is obtained. This phenomenon is called "homogeneous nucleation" of the liquid state. If impurities, such as ions and particulates, exist in a supersaturated system, vapor may condense on the surfaces of these impurities. This phenomenon is called "heterogeneous nucleation".

At the CFFF, species K_2SO_4 and K_2CO_3 will reach a supersaturated state at the outlet of the secondary combustor. From the chemistry calculations (NASA 273 Equilibrium Code), one can find the supersaturation ratio for K_2SO_4 as $p/p_\infty = 4.2$, at 1500K. At this condition nucleation will occur. Since in the CFFF system there are many species, including K_2CO_3, flyash, and K_2SiO_3, the nucleation is more likely heterogeneous. In this dissertation, heterogeneous nucleation appears to be more important.

Homogeneous Nucleation

When a pure vapor or a component of a gas mixture exceeds the saturation condition in an unconfined space, spontaneous condensation, called homogenous nucleation, may be observed depending on the degree of supersaturation achieved, and the nature and

concentration of the nuclei present in the gaseous medium. When the saturation state is reached, the vapor and the liquid phases reach equilibrium states. The equilibrium between these two phases requires equality of temperatures

$$T_l = T_v \tag{F.1}$$

equality of pressures

$$p_l = p_v, \tag{F.2}$$

and equality of chemical potentials

$$\mu_l = \mu_v. \tag{F.3}$$

where the chemical potential is defined as

$$\mu_i = \left(\frac{\partial G}{\partial n_i}\right)_{T,p,n_j} \tag{F.4}$$

G is the Gibbs free energy, which is

$$G = U - TS + pV, \tag{F.5}$$

where T is the absolute temperature, V is the volume per mole, U is the internal energy per mole, S is the entropy per mole of material in the system, and p is pressure. The work required to form a spherical embryo of radius r in a system containing n_v molecules of vapor and n_l of liquid phase with free energy of the surface σ is

$$\Delta G = 4\pi r^2\sigma + \frac{4\pi}{3} r^3 n_l(\mu_l - \mu_v), \tag{F.6}$$

where μ_l is the chemical potential of the condensed phase, and μ_v is the chemical potential of the vapor molecules.

For an isothermal process at an arbitrary vapor pressure p,

$$d\mu_v = V_v dp \quad \text{and} \quad d\mu_l = V_l dp$$

or

$$d(\mu_l - \mu_v) = (V_l - V_v)dp, \tag{F.7}$$

where V_l is the volume of a species molecule in the liquid phase and V_v is the volume of a species molecule in the vapor phase. When two phases are in an equilibrium state, the chemical potential is the same in each phase. In the case of the species being a perfect gas, integration of Eq.(F.7) for a supersaturated state with $V_v >> V_l$, yields:

$$\mu_l - \mu_v = -kT \ln \frac{p}{p_0}, \tag{F.8}$$

where the ratio p/p_0 is the supersaturation ratio, S. Thus

$$\Delta G = 4\pi r^2 \sigma - \frac{4\pi}{3} r^3 n_l kT \ln S, \tag{F.9}$$

The most interesting case is vapor in a supersaturated state. For $p > p_0$ the free energy involved in the creation of an embryo has a maximum value ΔG^* at a radius r^*. Embryos with radii $r < r^*$ are unstable and tend to disappear. On the other hand, embryos which exceeded the critical radius r^* tend to grow to macroscopic droplets. Droplet embryos having the critical radius r^* are in unstable equilibrium with the supersaturated vapor.

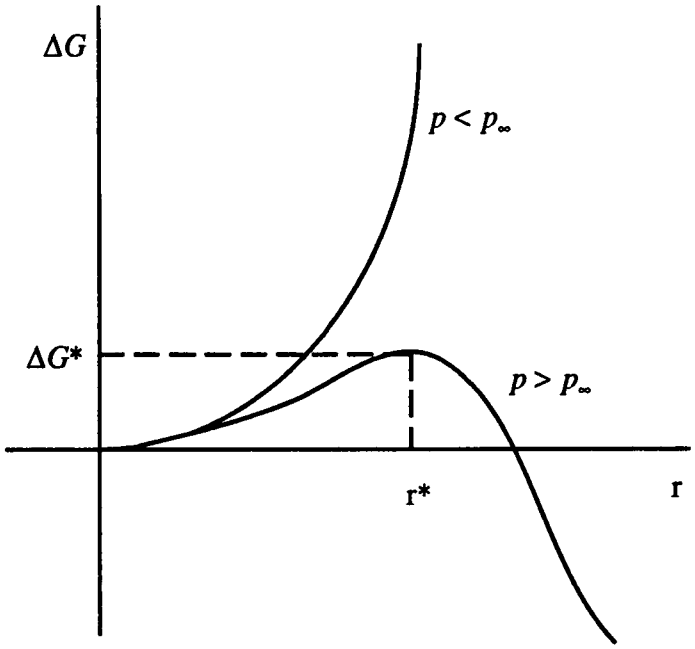


Figure F.1 ΔG Required to Form a Droplet of Radius r in a Vapor with Partial Pressure p

The critical radius is given by

$$\left.\frac{\partial \Delta G}{\partial r}\right|_{r=r^*} = 0. \tag{F.10}$$

For spherical embryos, this results in

$$r^* = \frac{2\sigma}{n_l kT \ln S} = \frac{2\sigma V_l}{kT \ln S}. \tag{F.11}$$

The critical free energy becomes:

$$\Delta G^* = \frac{4\pi}{3} r^{*2}\, \sigma. \tag{F.12}$$

or

$$\Delta G^* = \frac{16\pi\sigma^3}{3(n_l kT \ln S)^2}. \tag{F.13}$$

The nucleation rate is given by [78,79]

$$J = \frac{p}{\sqrt{2\pi m_v kT}} 4\pi r^{*2} n_v e^{-\frac{\Delta G^*}{kT}}. \tag{F.14}$$

When the liquid droplet solidifies, the nucleation theory can be modified.[80,81,82] The modification is applied to the free energy of the solid sphere and the nucleation rate. The critical radius remains unchanged. For a solid sphere, the free energy can be written as

$$\Delta G_s^* = \frac{16\pi\sigma_s^3 \xi V_s}{3(kT \ln S)^2}. \tag{F.15}$$

and the nucleation rate is

$$J = \frac{p}{\sqrt{2\pi m_v kT}} 4\pi r^{*2} \Lambda n_v e^{-\frac{\Delta G_s^*}{kT}}. \tag{F.16}$$

where

Λ = correction factor for the surface area of the solid. For a sphere $\Lambda = 1.0$.

σ_S = free energy per unit area of the solid-vapor interface.

V_S = molecular volume in the solid phase.

ξ = 1.0 for a solid sphere.

Therefore, a solid sphere is almost equivalent to the liquid droplet for nucleation. At the CFFF, the supersaturated ratio and the nucleation rate for homogeneous nucleation are plotted in Figure (F.2).

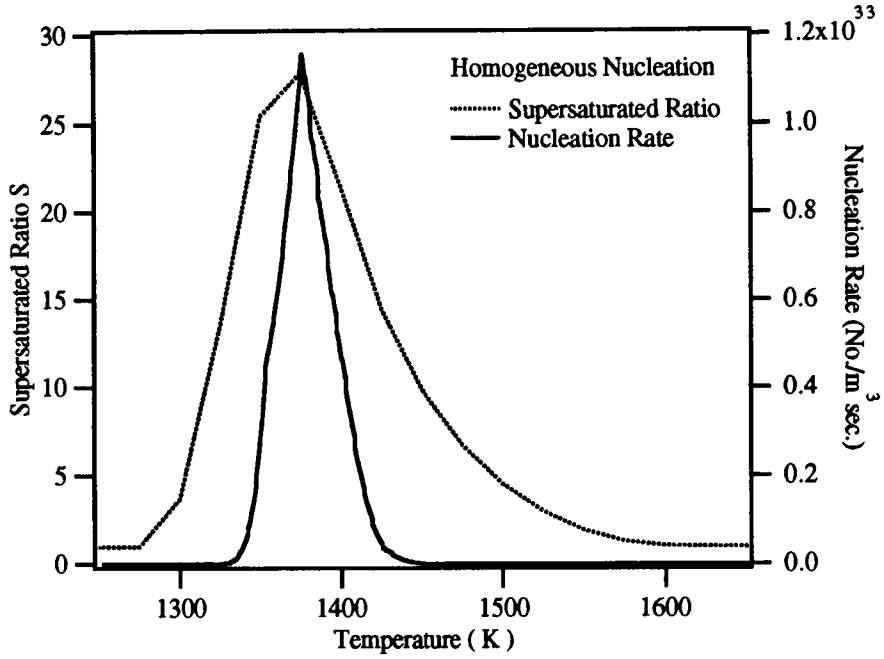


Figure F.2 Supersaturated Ratio and Nucleation Rate After the SC at CFFF

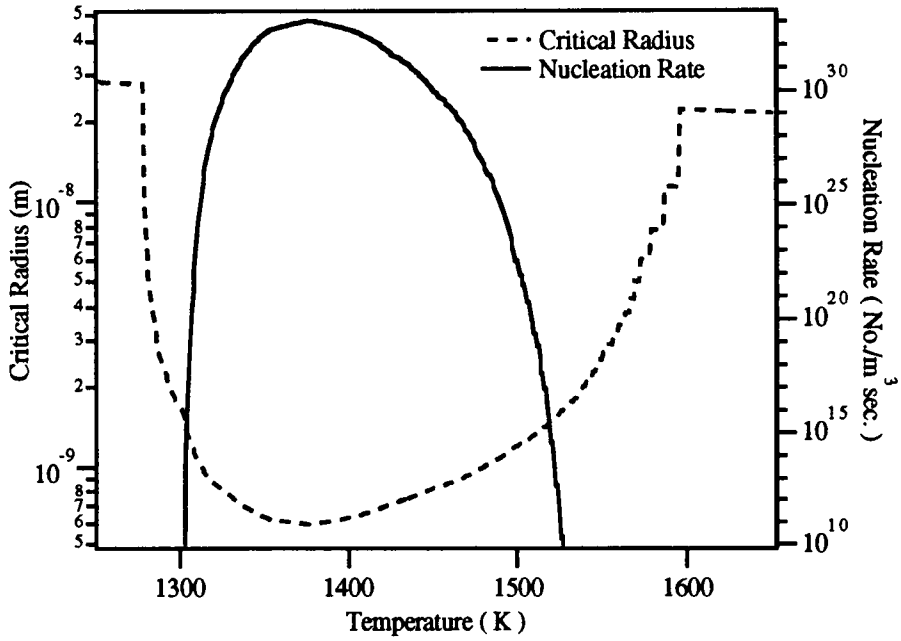


Figure F.3 Critical Radius and Nucleation Rate After the SC at CFFF

From Figure (F.2), it is clear that homogeneous nucleation occurs at gas temperature between 1340 K and 1425 K. These temperatures occur at the CFFF from the outlet of the secondary combustor into CS1.

Heterogeneous Nucleation

When a supersaturated vapor contains a number of small different particles, "foreign particles", these "foreign" particles can act as centers of spontaneous condensation. Depending on the cooling rate and the number of foreign nuclei, the resulting transition of phase of the metastable supersaturated vapor may take place at considerably lower supersaturation ratios than required for homogeneous nucleation.[83]

Because nucleation onto foreign matter involves at least one additional degree of freedom, the analysis of heterogeneous nucleation is more complicated than homogeneous nucleation. The nucleation rate will depend on the nature of the nucleus surface, including its geometry and chemical properties, its chemical compatibility with the vapor, and the condition of the surface in addition to the supersaturation ratio.[84]

A droplet nucleating on a foreign sphere will take the shape of a spherical cap provided that it does not wet the surface (Figure F.4). The two key geometrical parameters for the droplet are the radius of curvature r and the angle of contact between the liquid and the substrate ϕ. For equilibrium on the foreign surface, the line common to the three phases-substrate C, liquid L , and vapor V (G) - has to be restricted by

$$x = \cos\phi = \frac{\sigma_{CG} - \sigma_{CL}}{\sigma_{LG}}. \qquad \text{(F.17)}$$

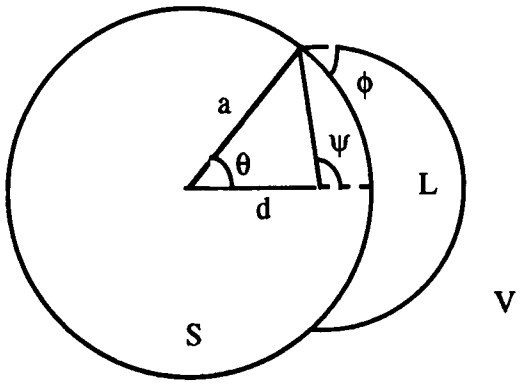


Figure F.4 An Embryo in the Form of a Spherical Cap

The free energy of formation for an embryo as a spherical cap then is given by

$$\Delta G = \frac{\pi r^3}{3} n_v (2+x)(1-x)^2 (\mu_l - \mu_v) + 2\pi r^2 (1-x)\sigma_{lv} + \pi r^2 (1-x^2)(\sigma_{cl} - \sigma_{cv}). \tag{F.18}$$

Applying the criterion that the free energy of formation of the critical sized cap should be a maximum, one can find that the critical radius of curvature will be the same as Eq.(F.11). Then the critical free energy is

$$\Delta G_c^* = \frac{16\pi\sigma_{LG}^3 V_L^2}{3(kT\ln S)^2} f(x), \tag{F.19}$$

where

$$f(x) = \frac{(2+x)(1-x)^2}{4}. \tag{F.20}$$

Thus the coefficient $f(x)$ represents a correction to the case of homogeneous nucleation. The range of $f(x)$ is $0 \le f(x) \le 1$ so that any foreign particles acting as nuclei will reduce the free energy necessary to form an embryo of critical size.

Under the normal condition, the surfaces of foreign nuclei will not be flat but will be irregular or curved. Fletcher[85] has summarized the geometrical corrections that have to made to account for variations in size of the nuclei. Instead of the correction *f(x)* being a function of *x* only, in this case, the curvature ratio *r/r** has to be included as

$$f(x,z)=1+\left(\frac{1-xz}{\tilde{g}}\right)^3+x^3\left[2-3\frac{z-x}{\tilde{g}}+\left(\frac{z-x}{\tilde{g}}\right)^3\right]+3xz^2\left(\frac{z-x}{\tilde{g}}-1\right), \tag{F.21}$$

with $z=r/r^*$, and $\tilde{g}=\sqrt{1+z^2-2xz}$. Fletcher also gave the nucleation rate per particle as

$$I^0=\frac{p}{\sqrt{2\pi m_c kT}}4\pi^2 r^2 r^{*2} n_{ads}\exp(-\frac{\Delta G_c^*}{kT}). \tag{F.22}$$

where n_{ads} is the number of (single) vapor molecules adsorbed per unit surface area of substrate. It can be roughly expressed as

$$n_{ads}\approx\left(\frac{p}{kT}\right)^{\frac{2}{3}}. \tag{F.23}$$

If the concentration of the nucleating particle of radius *r* is *n(r,t)*, the nucleation rate is

$$J=I^0 n(r,t)=\frac{p}{\sqrt{2\pi m_c kT}}4\pi^2 r^2 r^{*2} n_{ads} n(r,t)\exp(-\frac{\Delta G_c^*}{kT}). \tag{F.24}$$

The rate of heterogeneous nucleation is plotted in Figure (F.5) along with the rate of homogeneous nucleation. Because heterogeneous nucleation needs less free energy than homogeneous nucleation so that it occurs over a wider temperature range than homogeneous nucleation, but with a lower nucleation rate.

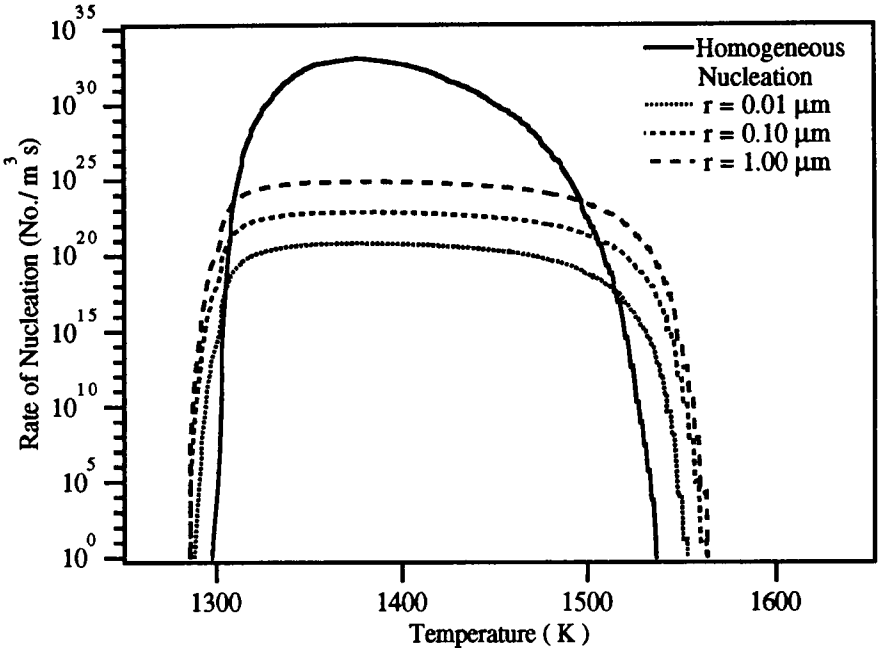


Figure F.5 Heterogeneous Nucleation Rate

APPENDIX G TURBULENT AND GRAVITATIONAL COAGULATION

Turbulence can affect coagulation by two different mechanisms. In the first case, since spatial non-homogeneities are brought about by the turbulent flow, different velocities of neighboring particles can appear, causing collisions by a mechanism analogous to the mechanism of laminar shearing flow. In addition, each particle will have a relative motion differing from that of the turbulent air because its inertia will not be the same as an equivalent mass of air. Since the inertia of the particles depends on their size, the first mechanism can give rise to collisions between equally and unequally sized particles, while the second mechanism results only in encounters between unequally sized particles.

Hidy and Brock[32] has given an expression for turbulent coagulation. The expression is for collisions per unit time per unit volume (collision rate density).

$$L_{ij}^{(tur)} = 2\sqrt{2\pi}(r_i + r_j)^2 n_i n_j \times \left\{\left(1-\frac{\rho_g}{\rho_i}\right)^2\left(\frac{1}{A_i}-\frac{1}{A_j}\right)^2\overline{\left(\frac{Dq}{Dt}\right)^2} + \frac{1}{9}(r_i + r_j)^2\frac{\varepsilon_t}{\nu_g} + \frac{1}{3}\left(1-\frac{\rho_g}{\rho_i}\right)^2\left(\frac{1}{A_i}-\frac{1}{A_j}\right)^2 g^2\right\}^{\frac{1}{2}} \tag{G.1}$$

The first term in brackets involves acceleration of the flow, giving collisions from particle motion relative to flow, which is different because of the different response of different sized particles to turbulent fluctuations; The second term is due to random motions introduced by the variations in shear; and the third term is due to the gravitational settling.

In the first term of Eq.(G.1), Batchelor[86] gives

$$\overline{\left(\frac{Dq}{Dt}\right)^2} \approx 1.3\frac{\varepsilon_t^{3/2}}{\nu_g^{1/2}}. \tag{G.2}$$

In Eq.(F.1), A_i is

$$A_i = \frac{1}{B_i m_i} = \frac{9}{2}\frac{\mu_g}{r_i^2 \rho_i C_u} \tag{G.3}$$

where

B_k = mobility

m_k = mass of particle

C_u = Cunningham factor

$$= 1 + Kn\left(a' + b' e^{-c'\frac{1}{Kn}}\right). \tag{G.4}$$

For a length L of pipe

$$\varepsilon_t = \frac{\overline{V}\frac{\pi D^2}{4}\Delta p}{\rho_g \frac{\pi D^2}{4} L} \tag{G.5}$$

The pressure drop can be written as,

$$\Delta p = \frac{\pi D \tau_w L}{\frac{\pi D^2}{4}} \tag{G.6}$$

and the shear stress as

$$\tau_w = \frac{f}{2}\rho_g \overline{V}^2. \tag{G.7}$$

Therefore, the energy dissipated per unit mass is

$$\varepsilon_t = 4 \cdot \frac{f}{2} \cdot \frac{\overline{V}^3}{D}. \qquad \text{(G.8)}$$

For the CFFF MHD system, total mass flow at the secondary combustor is 9.7 lb/sec, which is equivalent to $\dot{m} = 4.4 kg$ / sec. Other typical data are

D= 1.87 m

T=1442 ^{o}K

ρ_g = 0.14 kg/m^3

ρ_p = 2500 kg/m^3

μ_g = 5.0x10^{-5} kg/m-sec

$\overline{V}$ = 8 m/s

ν_g = 3.6x10^{-4} m^2/sec.

For a particle of 1.0 μm, R_e=0.0224. Since the Reynolds number is very small, the friction factor is relatively large. For the purpose of estimating ε_t, one can take f=0.1. From Eq.(G.8)

$$\varepsilon_t = 54.8 \text{ m}^2/\text{sec.}^3 \text{ and } \overline{\left(\frac{Dq}{Dt}\right)^2} = 2.78\text{x}10^4 \text{ m}^2/\text{sec.} \qquad \text{(G.9)}$$

$$\frac{\rho_g}{\rho_i} = 0. \qquad \text{(G.10)}$$

For r_i =0.1 μm, A_i^{-1} = 1.24 x10^{-7} sec. and for r_j =2.0 μm, A_j^{-1} = 7.29 x10^{-5} sec. From Eq.(G.1), one can obtain

first term in bracket = 1.48x10^{-4} m^2/sec.^{2}

second term in bracket = 2.04x10^{-8} m^2/sec.^{2}

third term in bracket = 5.11x10^{-7} m^2/sec.^{2}

From the calculation, it can be seen that the effect of the turbulence fluctuations causes the most turbulent coagulation while the gravitational coagulation and random motion coagulation are very small. Thus, only the first term is important. Hence

$$L_{ij}^{(tur)} = (1.48\times10^{-4})^{\frac{1}{2}} 2\sqrt{2\pi}(2.1\times10^{-6})^2 n_i n_j = \left(2.69\times10^{-13}\right) n_i n_j. \tag{G.11}$$

If number concentration of particle j (1.0μm) is $n_j = 10^{+11}$ particle/m^3 (Appendix A), Eq.(G.1) gives

$$-\frac{1}{n_i}\frac{dn_i}{dt} = 0.0269. \tag{G.12}$$

Integrating,

$$\frac{n_i}{n_{i0}} = e^{-0.0269t}. \tag{G.13}$$

and for a particle residence time of 1.0 sec.

$$\frac{n_i}{n_{i0}} = 0.973 = 97.3\%. \tag{G.14}$$

Thus, the fraction of particles collected due to turbulence equals 1-0.973=0.027 for a large particle radius of 2μm. Approximately 3 percent of the small (0.1μm) particles are collected by the turbulent effects after 1.0 second. For large particles of 4.0μm, $n_j=10^{+9}$ particle/m^3, careful calculation gives $n_i/n_{i0}=0.996$. Only 0.4 percent of small particles are collected by 4.0μm particles. Therefore, in this dissertation, turbulent coagulation is neglected. So is gravitational coagulation.

APPENDIX H MIGRATION OF PARTICLES TO THE WALL

Deposition of particles on a surface is caused by different mechanisms primarily depending on particle size, as discussed by Im and Chung.[13]

Particles, by virtue of fluid turbulence, will diffuse across the mean streamlines toward the wall. Particles of a diameter of several microns have sufficient momentum to be able to cross the laminar sublayer and deposit on the wall, but the momentum of fine particles dissipates in the laminar sublayer and turbulence alone does not suffice to cause the particles to diffuse to the wall. At this stage, thermophoresis is an effective phenomenon which drives fine particles to the wall.

The velocity profile in turbulent flow can be divided into three regions[13]: the fully turbulent region, the buffer layer and the laminar sublayer.

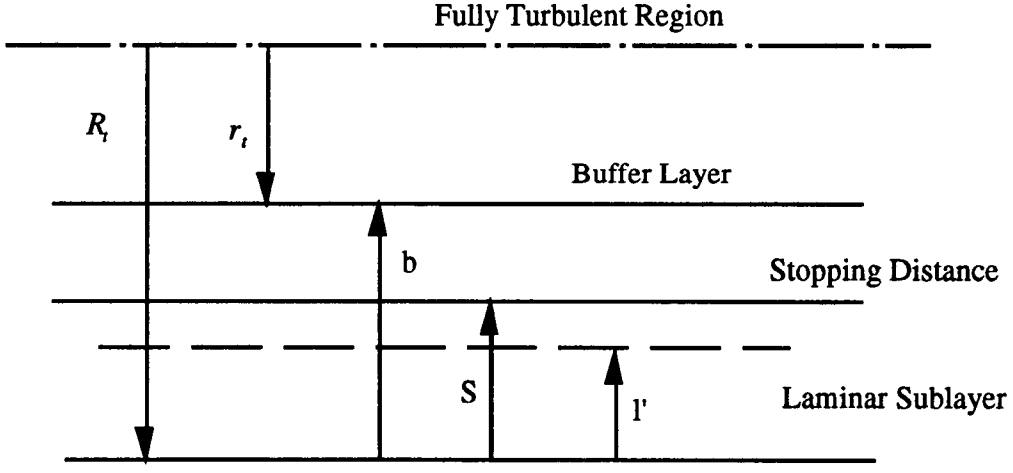


Figure H.1 Sketch of Flow Regions

Effective Deposition Velocity

According to Im and Chung, the effective deposition velocity of any particle originating in the fully turbulent region with a mass fraction C_A is given by

$$\frac{J_A}{C_A} = \frac{1}{\frac{1}{\hat{D}(b)} + \frac{1}{V}}. \tag{H.1}$$

where J_A is the particle flux toward the surface, $\hat{D}(b)$ is the effective diffusion velocity of the particle across the buffer layer, and V is related to the migration velocity through the sublayer adjacent to the wall; V is controlled by either turbulence-imparted momentum or thermophoresis. Calculations show that the turbulence-imparted momentum does not have any significant effect for particles whose radius is between 0.086 to 0.86 μm and hence, it can be totally neglected for these particles.

Effective Turbulent Diffusion Velocity

The term $\hat{D}(b)$ is defined as

$$\hat{D}(b) = \left[\int_s^b \frac{dy}{D_e}\right]^{-1} = \frac{0.4V^*}{Sc\left\{0.92\ln\left(\frac{b^+}{S^+ + k_s^+}\right) + \frac{13}{S^+ + k_s^+} + \frac{365}{\left(S^+ + k_s^+\right)^2}\right\}}, \tag{H.2}$$

where

$$\begin{aligned} b^+ &= b\frac{V^*}{\nu} \\ S^+ &= S\frac{V^*}{\nu}. \\ k_s^+ &= k_s\frac{V^*}{\nu} \end{aligned} \tag{H.3}$$

The particulate Schmidt number is

$$Sc = \frac{\varepsilon'}{D_e}, \tag{H.4}$$

where

ε' = eddy diffusivity of gas

D_e = particulate eddy diffusivity.

For fine particles, as shown

$$\frac{D_e}{\varepsilon'} \rightarrow 1.0$$

Hence,

$$Sc^{-1} \rightarrow 1.0$$

thus,

$$Sc=1.0. \tag{H.5}$$

Assuming a hydrodynamically smooth surface with surface roughness, k_S =0.0 so that $k_s^+ = 0.0$. The buffer layer region exists between b^+ and l^+. Reasonable values for these are[87]

$$b^+ = 30.0 \text{ and } l^+ = 6.0 = S^+. \tag{H.6}$$

If turbulent deposition is effective, $S \geq l^+$, but if it is not, and thermophoresis is, then replace S with l^+.

Friction velocity V^* is obtained from the following relations:

$$\frac{V^*}{\nu} = \frac{V^*}{\overline{V}} \cdot \frac{\overline{V}}{\nu}, \tag{H.7}$$

$$\frac{V^*}{\overline{V}} = \sqrt{\frac{f}{2}}, \tag{H.8}$$

$$\frac{\overline{V}}{\nu} = \frac{R_e}{D}. \tag{H.9}$$

The friction coefficient factor is[88]

$$\frac{f}{2} = 0.092 R_e^{-0.2}. \tag{H.10}$$

Eq.(H.8) reduces to

$$V^* = \overline{V}\sqrt{0.092 R_e^{-0.2}} \tag{H.11}$$

and Eq.(H.2) becomes to

$$\hat{D}(b) = \frac{0.4\overline{V}\sqrt{0.092 R_e^{-0.2}}}{0.92 \ln \frac{30.0}{6.0} + \frac{13.0}{6.0} + \frac{365.}{(6.0)^2}}. \tag{H.12}$$

The steady-state velocity, $\overline{V}$, as measured is approximately 8.0m/s.

Particle Diffusion Velocity

The conduction heat flux at the surface of the wall is equal to the convection heat flux

$$k\nabla T = h(T_g - T_w). \tag{H.13}$$

Applying the Reynolds analogy,

$$St = \frac{f}{2} = \frac{h}{\rho_g \overline{V} C_p}. \tag{H.14}$$

then

$$\nabla T = \frac{\overline{V}}{\alpha} \cdot \frac{f}{2} \cdot (T_g - T_w) \tag{H.15}$$

which is the temperature gradient at the surface, and this gradient will be constant through the laminar sublayer.

If Eq.(B.6) equation is rearranged to read

$$\frac{U_t T_0}{\nu \nabla T} = A(Kn), \tag{H.16}$$

where

$$A(Kn) = \frac{-2C_s(\frac{k_g}{k_p} + C_t\frac{\lambda}{r})(1 + \frac{\lambda}{r}(a' + b'e^{-c'\frac{r}{\lambda}}))}{(1 + 3C_m\frac{\lambda}{r})(1 + 2\frac{k_g}{k_p} + 2C_t\frac{\lambda}{r})}. \tag{H.17}$$

then

$$U_t = A(Kn) \cdot \frac{\overline{V}}{\alpha} \cdot \nu \cdot \frac{f}{2} \cdot \frac{T_g - T_w}{T_w}, \tag{H.18}$$

Finally,

$$U_t = A(Kn) \cdot \overline{V} \cdot \mathrm{Pr} \cdot (0.092 R_e^{-0.2}) \cdot \frac{T_g - T_w}{T_w}, \tag{H.19}$$

where, for this region, $T_0 \approx T_w$, thus, $U_t = V$ is the effective diffusion velocity of the particles across the laminar sublayer. The terms $\hat{D}(b)$ and V being known, J_A/C_A is calculated using Eq.(H.1).

Collection Efficiency of wall

The collection efficiency of the wall is defined as

$$\eta = 1 - \frac{C_A}{C_{A0}}, \tag{H.20}$$

where

$$\frac{C_A}{C_{A0}} = \exp\left(-\frac{J_A}{C_A} \cdot \frac{4}{\overline{V}} \cdot \frac{L}{D}\right), \tag{H.21}$$

Assuming J_A/C_A to be constant in a given section:

$$\text{inflow} = C_A \overline{V} A,$$

$$\text{outflow} = C_A \overline{V} A + \frac{d}{dx}(C_A \overline{V} A)dx,$$

$$\text{deposition} = \pi D J_A(x)dx,$$

Mass balance relation gives:

inflow = outflow + deposition.

which mathematically is written

$$-\frac{dC_A}{dx} = \frac{4}{D} \cdot \frac{J_A}{\overline{V}}, \tag{H.22}$$

Rearrange:

$$-\frac{dC_A}{C_A} = \frac{4}{D} \cdot \frac{J_A}{C_A} \frac{dx}{\overline{V}}, \tag{H.23}$$

and integrating it with J_A/C_A known. Finally

$$\eta = 1 - \exp\left(-\frac{J_A}{C_A} \cdot \frac{4}{\overline{V}} \cdot \frac{L}{D}\right), \tag{H.24}$$

At the CFFF, one can estimate the wall collection efficiency, η, with

$\overline{V}$ = 8.0 m/s

L= 0.5 m

D = 1.87 m

$\nu = 3.6 \times 10^{-4}$ m^2/s.

This collection efficiency is plotted in Figure H.2, which shows that the wall effects are very small at the CFFF(i.e.,1.0 % for very small particles). Since the dimensions of the CFFF flow train is very large and the laminar sublayer is very thin, only a small portion of the small particles are removed by wall effects. Therefore, the wall effects can be neglected.

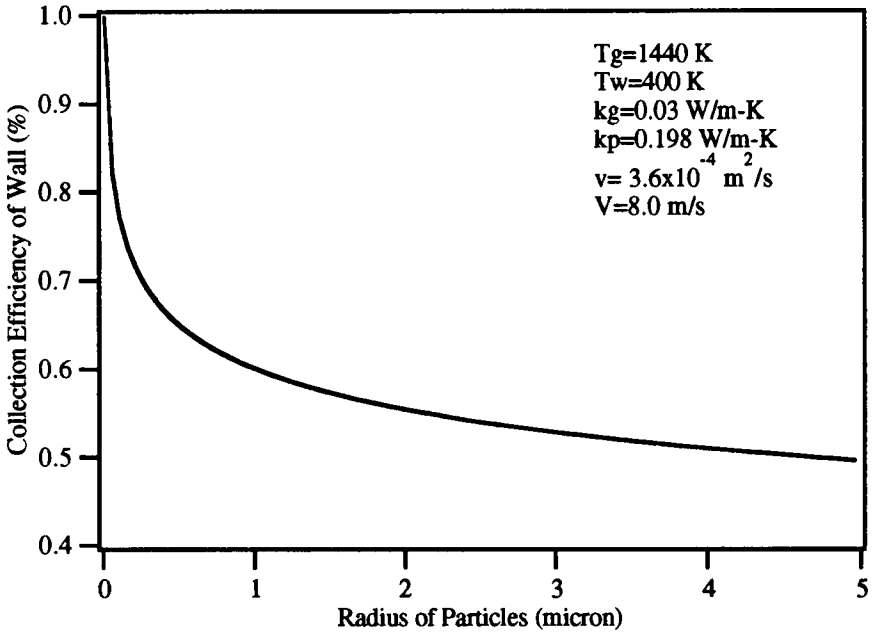


Figure H.2 Collection Efficiency of the Wall

APPENDIX I PARTICLE INJECTOR AND ITS MASS LOADING

The injector used for particle injection at the CFFF is sketched in Figure I.1.

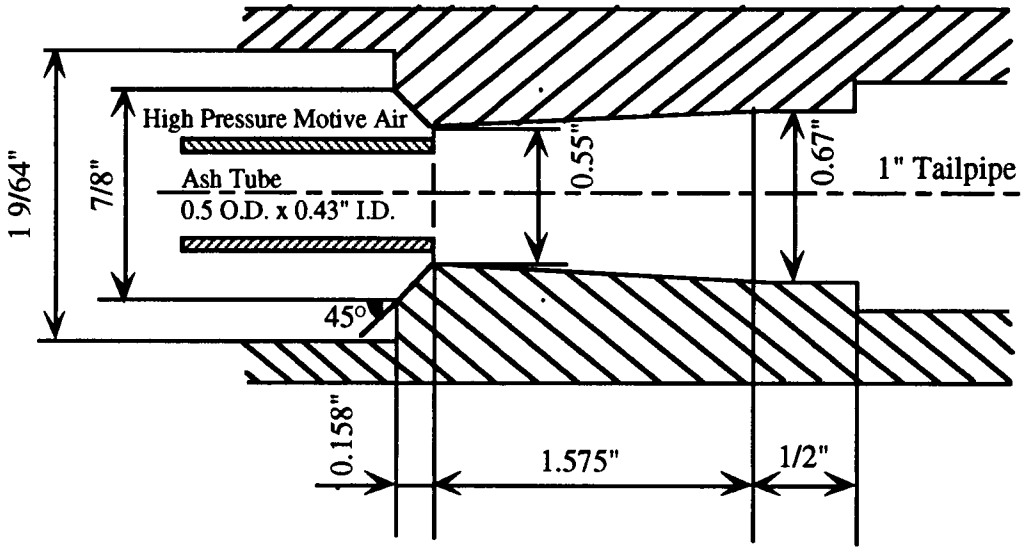


Figure I.1 Sketch of Particle Injector

A diagram of the injection experiment at the CFFF is shown in Figure I.2.

The measured mass loading of the injector is given by Figure I.3 for coal flow[89] and for ash flow.

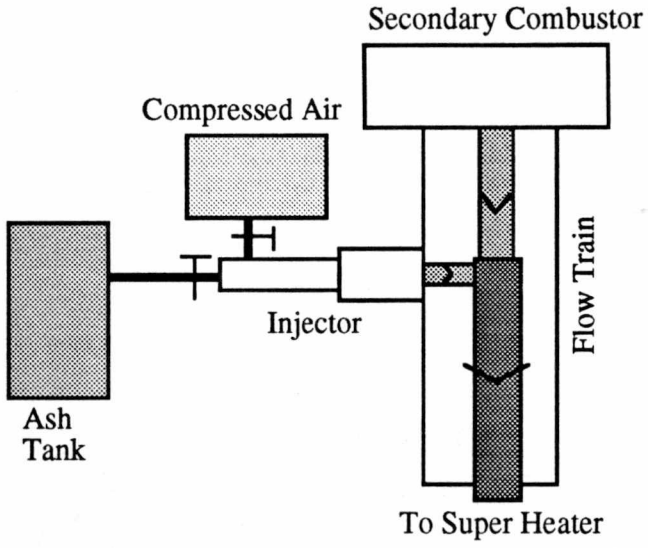


Figure I.2 Injection Experiment at CFFF

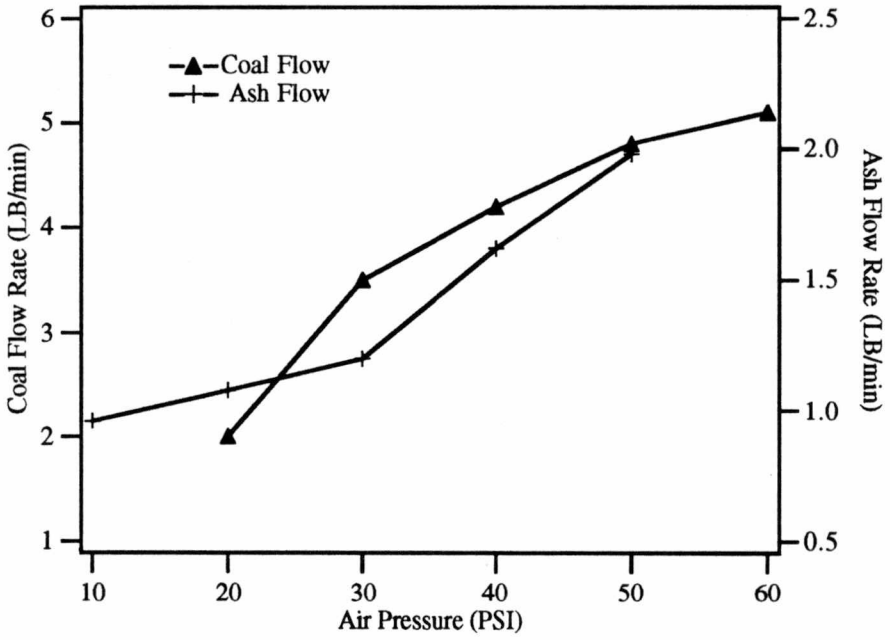


Figure I.3 Injector Flow Rate vs. Air Pressure

VITA

Dujiu Yang was born on December 29, 1963 in Beijing, the People's Republic of China. He entered elementary school in 1971 and high school in 1977. After graduation from the high school in 1981, he entered Tsinghua University in Beijing. He studied laser and nonlinear optics from the Department of Electrical Engineering and Information and received his B. S. in 1986. In the same year, he entered the University of South Mississippi, Hattiesburg, Mississippi, as a graduate student in the Department of Physics. He transferred to the University of Tennessee Space Institute in 1987 and received his Master degree in physics in 1990. He also worked for Energy Conversion Program division as a graduate research assistant. His master's thesis concerns the two-body Dirac equation. In 1990, he entered the Doctoral Program.

He has many hobbies, such as oil-painting, travel, photography and sports. Soccer is his favorite sport, which he has played for fifteen years now.

He married miss Kewei Wu in 1992.